Semiconductors, Vol. 38, No. 12, 2004, pp. 1365–1368. Translated from Fizika i Tekhnika Poluprovodnikov, Vol. 38, No. 12, 2004, pp. 1409–1413.

ELECTRONIC AND OPTICAL PROPERTIES OF SEMICONDUCTORS

Electrical Conductivity and Thermoelectric Power of Liquid Tellurium Doped with 3*d* Transition Metals

V. M. Sklyarchuk and Yu. O. Plevachuk^

Franko National University, Lviv, 79005 Ukraine

^e-mail: plevachuk@mail.lviv.ua

Submitted March 4, 2004; accepted for publication April 8, 2004

Abstract—The electrical conductivity and thermoelectric power of liquid tellurium with transition 3*d* metal impurities were measured in a wide temperature range (from 1700 K to the crystallization temperature) under argon pressure (up to 25 MPa). It is shown that Ti, V, Cr, and Mn impurities decrease the conductivity and slightly increase the thermoelectric power, whereas Fe, Co, Ni, and Cu impurities increase the conductivity and slightly decrease the thermoelectric power. In the region above 1200 K, the thermoelectric power remains virtually constant, whereas the conductivity decreases. The results obtained are interpreted in the context of the model of *s–d* hybridization. To describe electron scattering in such systems, the Friedel–Anderson procedure is used, based on the ideas about the existence of virtual bound states. © *2004 MAIK "Nauka/Interperiodica"*.

1. INTRODUCTION

Liquid tellurium occupies an intermediate position between semiconductors and metals and, therefore, understanding its properties is important for studying the properties of melts, as is shown by the numerous publications in this field over the last few decades [1–8]. Studies dealing with the effect of transition elements on the electronic properties of melts are much less numerous [9–13], and they are restricted to the temperature region below 1200 K. At the present stage of the research, the interpretation of the obtained results does not extend beyond the effect of the change in the density of states at the Fermi level if transition metals are added to liquid tellurium.

Several models of the electronic structure of liquid tellurium were considered [14, 15] and were later integrated into a single theory [16]. Using the structural data obtained by the EXAFS method, the authors of [16] performed Monte Carlo calculations and obtained the energy distribution of the density of states $N(E)$ of conduction electrons in liquid tellurium. The density of states has a shallow minimum (pseudogap), and the Fermi level is shifted towards the valence band.

Since the value of the conductivity lies in the region of the diffusive mechanism of charge transport, we may use the formulas for the conductivity (σ_0) and the thermoelectric power (S_0) suggested by N.F. Mott [17],

$$\sigma_0 = \frac{2\pi e^2 \hbar^3}{m^2} L_0 [N_0(E_f)]^2, \quad (1)$$

$$S_0 = -\frac{\pi^2 k_b^2 T}{3e}\left(\frac{d\ln\sigma_0}{dE_f}\right); \quad (2)$$

here, $N_0(E_f)$ is the density of states at the Fermi level E_f for conduction electrons, L_0 is the electron mean free path (on the order of interatomic spacing), T is temperature, k_b is the Boltzmann constant, e is the elementary charge, and m is the effective mass.

To describe *s* states of the impurity centers, we may use the procedure based on the idea of virtual bound states [18]. This procedure was developed for the description of magnetic properties of impurity atoms; however, it is also important for understanding the electron scattering processes. At the same time, it is known that 3*d* impurities in a melt can also have a magnetic moment. Then the virtual level is split, and we obtain a two-level system with different occupancies of the levels [19].

To simplify the discussion, we use the following relation obtained in [10] for the change in density of states at the Fermi level under the condition of fivefold degeneracy:

$$\Delta N(E_f) = \frac{5c}{\pi} N_0(E_f) \frac{dN_0(E)}{dE} \sin\frac{N_d \pi}{5} \equiv c\Delta\rho_s, \quad (3)$$

where c is the concentration of the 3*d* impurity and N_d is the density of states for the *d* element.

The effect of *s–d* interaction can be interpreted as a variation in the mean free path in expression (1) for the conductivity. The mean free path may be written as

$$\frac{1}{L} = \frac{1}{L_0} + \frac{c}{V_f \tau_{sd}}, \quad (4)$$

where L_0 is the mean free path in pure Te, V_f is the electron velocity at the Fermi level, and τ_{sd} is the relaxation time for resonant *s–d* scattering. It was shown previ-

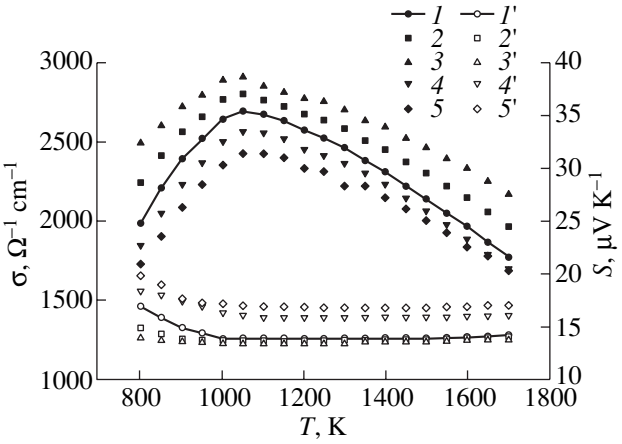

Fig. 1. (*1*–*5*) Electrical conductivity σ and (*1*'–*5*') thermoelectric power *S* for (*1*, *1*') pure Te; (*2*, *2*') Te + Fe (2 at %); (*3*, *3*') Te + Fe (4 at %); (*4*, *4*') Te + Ti (2 at %); and (*5*, *5*') Te + Ti (4 at %).

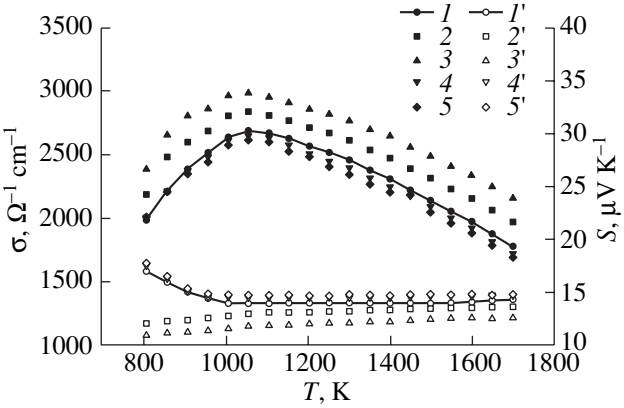

Fig. 2. (*1*–*5*) Electrical conductivity σ and (*1*'–*5*') thermoelectric power *S* for (*1*, *1*') pure Te; (*2*, *2*') Te + Co (2 at %); (*3*, *3*') Te + Co (4 at %); (*4*, *4*') Te + V (2 at %); and (*5*, *5*') Te + V (4 at %).

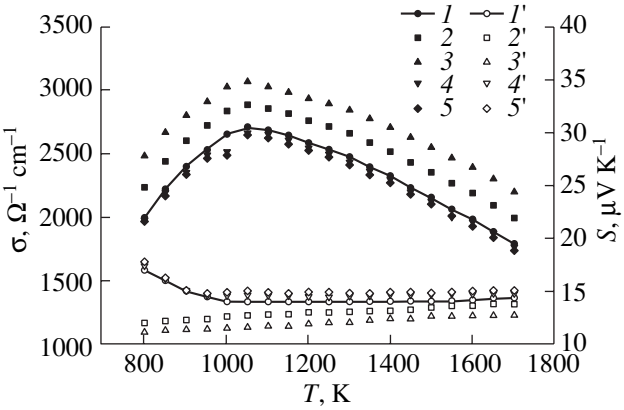

Fig. 3. (*1*–*5*) Electrical conductivity σ and (*1*'–*5*') thermoelectric power *S* for (*1*, *1*') pure Te; (*2*, *2*') Te + Ni (2 at %); (*3*, *3*') Te + Ni (4 at %); (*4*, *4*') Te + Cr (2 at %); and (*5*, *5*') Te + Cr (4 at %).

ously [10] that the relaxation time for resonant scattering can be written as

$$\frac{1}{\tau_{sd}} = \frac{20}{\pi\hbar N_0(E)}\sin^2\frac{\pi N_d}{10}. \quad (5)$$

Then, with allowance for (5), the effect of resonant scattering in expressions (1) and (2) is expected to decrease the conductivity and increase the thermoelectric power.

2. EXPERIMENTAL

We studied experimentally Te + Me (2 at %) and Te + Me (4 at %) (Me = Ti, V, Cr, Mn, Fe, Co, Ni, and Cu) melts. In order to keep the chemical composition constant and to prevent the evaporation of the volatile components, all measurements were performed under the condition of argon overpressure (up to 30 MPa). We used three-zone two-radii cells (with different but commensurate radii) made of boron nitride in the form of vertical containers with an internal cavity. Such cells must be used for the following reason. As a rule, measurement cells are dielectric containers made of a ceramic material, into which graphite probes are embedded. In almost all cases, the ceramic material is porous. Therefore, the melt is in contact with the wall of the container and diffuses into it. The concentration of the diffusing agent is highest at the "melt–wall" interface and exponentially decreases into the depth of the ceramics. Thus, in the bulk of the cell, a diffuse conducting layer is formed, which to some extent shunts the melt under study and produces uncontrollable errors in the conductivity measurements.

The formation of a conducting layer may be described as an increase in the radius of the sample by an effective value Δr. We may assume that Δr is the thickness of an additional layer of the sample that would produce the same shunting effect as that of the real conducting layer. Thus, this approach allows us to exclude analytically the error caused by the shunting effect. This method is described in detail in [20]. Note that the above shunting effect becomes significant for prolonged high-temperature studies, and under certain conditions it can produce an error of 40%. The thermoelectric power was measured by the standard method in the presence of a vertical gradient of 2–3 K/cm. The measurement error did not exceed 2% for the conductivity and 5% for the thermoelectric power.

3. RESULTS AND DISCUSSION

The results of the measurements of the conductivity and thermoelectric power of tellurium containing transition 3*d* metal impurities are shown in Figs. 1–4. To understand better the results obtained, they are compared with the results obtained previously for intrinsic Te [5]. The experimental temperature dependences of the conductivity agree well with the results of [9, 21],

which were obtained in the interval from the melting temperature (T_m) to 1200 K. We could not find any systematic studies of the conductivity at higher temperatures or any data on the thermoelectric power. It should be noted that the behavior of the conductivity for all the studied melts correlates with the behavior of the conductivity of pure tellurium. The introduction of Ti, V, Cr, and Mn impurities reduces the conductivity, and a higher impurity concentration results in a greater decrease in the conductivity. The thermoelectric power of these melts increases only slightly, by ~(1–2) μV/K. The thermoelectric power is about 14–16 μV/K in the entire investigated temperature range and shows a slight tendency to increase at high temperatures. After introducing the Fe, Co, Ni, and Cu impurities, the conductivity increases and the thermoelectric power decreases. The role of the impurity is illustrated in Fig. 5.

It follows from Figs. 1–4 that the electrical conductivity of all melts behaves in virtually the same way, apart from the absolute values. In the range from T_m to 1000 K, the conductivity increases; in the range from 1000 to 1200 K, it is weakly temperature-dependent and decreases with further heating. After melting, the thermoelectric power slightly decreases in a narrow temperature interval, remains positive in almost the entire investigated temperature range, and shows a weak tendency to increase. In [5], such a complicated behavior of kinetic coefficients for pure Te was interpreted in the context of the modified Ziman theory. To this end, the form factor of the temperature-dependent pseudopotential was introduced, as well as the effective radius of the Fermi sphere that increased with temperature. A similar interpretation was also suggested in [4]. However, for our melts, the application of the Ziman theory encounters certain difficulties caused by the change in the mechanism of charge-carrier scattering. We have already noted that the introduction of transition-metal impurities should lead to a decrease in the conductivity and, according to formulas (1) and (2), to an increase the thermoelectric power.

It can be seen from the experimental results obtained that this it not exactly so. For some melts, this position is true and for others it is not. In [10] the model of liquid tellurium with transition-metal impurities was considered; in this model, the positions of the energies of impurity states relative to the Fermi level were important. In Section 1, we discussed the relaxation time in this model. Omitting the intermediate calculations, we cite the final result for the additional resistance in the melts of this type,

$$\Delta R = cR_0\left(\frac{20ma}{\pi\hbar^2 k_f N_0(E)}\right)\sin^2\frac{\pi N_d}{10} + \left(\frac{15eS_0(T)}{\pi^3 k_b^2 T N_0(E)}\right)\sin\frac{\pi N_d}{5}. \quad (6)$$

Here, k_f is the wave vector, a is the interatomic spacing, N_0 is the density of states for pure tellurium, S_0 is the thermoelectric power of pure tellurium, and N_d is the

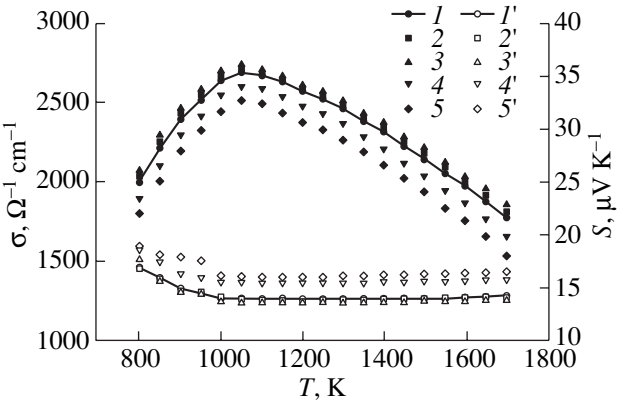

Fig. 4. (*1*–*5*) Electrical conductivity σ and (*1*'–*5*') thermoelectric power *S* for (*1*, *1*') pure Te; (*2*, *2*') Te + Cu (2 at %); (*3*, *3*') Te + Cu (4 at %); (*4*, *4*') Te + Mn (2 at %); and (*5*, *5*') Te + Mn (4 at %).

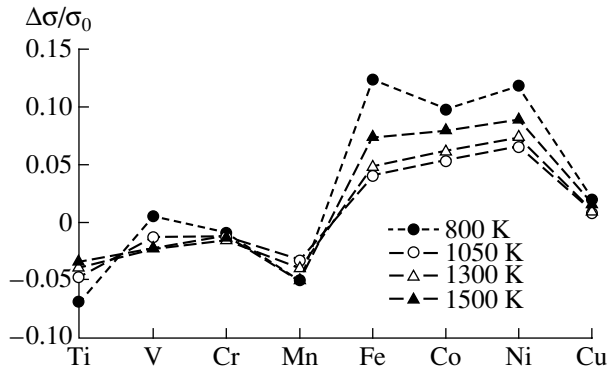

Fig. 5. Effect of 3*d* elements on the conductivity of tellurium.

density of impurity states. The analysis shows that in expression (6) the terms are not equally important. The first term gives a positive oscillating component, and the main contribution to the additional resistance comes from the second term. The second term is controlled by the rate of the variation in the density of states, i.e., by the position of the impurity state E_d with respect to the Fermi level. In our opinion, this model satisfactorily describes the behavior of the system; however, it requires many specific assumptions.

We suggest proceeding from the assumption that 3*d* impurities in the melt can have a magnetic moment. Therefore, the electrons at the Fermi level with different spin directions are differently scattered by these impurity centers. The scattering probability depends on the spin direction of the scattered electron with respect to the magnetic moment of the impurity atom. Then the general form of the Friedel sum rule may be written as

$$Z = \frac{1}{\pi}\sum\sum(2l+1)\eta_{l,\bar{\sigma}}, \quad (7)$$

where Z is the difference in the valences between the impurity atom and an atom of the matrix, l is the orbital

quantum number, $\eta_{l,\bar{\sigma}}$ is a phase shift, and $\bar{\sigma}$ is the spin index, which can have two values. Such a two-level model has three parameters [19]: the level width Γ, the level splitting $2U = \varepsilon_{d,\bar{\sigma}} - \varepsilon_{d,-\bar{\sigma}}$, and the level position with respect to the Fermi level $\varepsilon_d = (1/2)(\varepsilon_{d,\bar{\sigma}} + \varepsilon_{d,-\bar{\sigma}}) - E_f$. For resonant scattering, one phase shift is much greater than the others and is equal to $\eta_d = Z\pi/10$. Then we obtain the following equation:

$$\frac{Z\pi}{5} = \arctan\frac{\Gamma}{\varepsilon_d + U} + \arctan\frac{\Gamma}{\varepsilon_d - U}. \quad (8)$$

It follows from this equation that the system of virtual levels of the impurity center is formed under the conditions of strong interaction with conduction electrons. Then we find that the conductivity σ is given by

$$\frac{\sigma_0}{\sigma} = \text{const}[\sin^2\eta_{\bar{\sigma}}(E_f) + \sin^2\eta_{-\bar{\sigma}}(E_f)]. \quad (9)$$

The dependence obtained is represented by a curve with two peaks similar to that observed experimentally (Fig. 5). However, such a dependence does not explain deviations at $\sigma_0/\sigma > 1$ and $\sigma_0/\sigma < 1$. We must find the dependence of the virtual interaction parameters on quantum numbers. Note that the exchange or correlation repulsion of electrons with opposite spins occurs only if these electrons occupy the same atomic *d* level with energy ε_d. The Hartree–Fock approximation allows us to understand the significance of exchange terms. In our systems, the exchange integral *I* can assume both positive and negative values [22]. Without going into the details of the procedure, we write out the final result for the conductivity of the systems with impurities [23]:

$$\sigma \propto \sigma_0\left[1 - 2\frac{I}{N}N(E_f)\ln\left(\frac{D}{k_bT}\right)\right]. \quad (10)$$

Here, $N(E_f)$ is the density of states in the conduction band at the Fermi level, *N* is the number of atoms per unit volume, and *D* is a characteristic energy. We clearly see that the change in the conductivity $\Delta\sigma = \sigma - \sigma_0$ can be both positive and negative (Fig. 5). According to formula (2), the behavior of the thermoelectric power correlates completely with the results for the electrical conductivity.

The question of why the thermoelectric power remains virtually unchanged with decreasing conductivity at temperatures higher than 1200 K remains open. In (1) the only variables are the mean free path *L* and the density of states *N*(*E*). It follows from structural studies [24, 25] that *L* increases very slowly with temperature. At temperatures higher than 1200 K, the density of states decreases substantially. Therefore, the product $L[N(E)]^2$ and, accordingly, the conductivity decrease. Formula (2) may be rewritten as

$$S = -\frac{\pi^2}{3}\frac{k_b^2}{e}T\left[\frac{1}{L}\frac{dL}{dE} + \frac{2}{N(E)}\frac{dN(E)}{dE}\right]. \quad (11)$$

The first term in the brackets in (11) is always positive and the second term is negative. Since in the region of the pseudogap the density of states depends on energy approximately as E^2 and the corresponding dependence of *L* is generally weaker, the resulting sign of the thermoelectric power is positive, which agrees with the experimental observations. Since the Fermi level is shifted to the valence band [16], the expression in the brackets in (11) varies with temperature only slightly, and we therefore obtain virtually temperature-independent thermoelectric power.

REFERENCES

1. V. M. Glazov, S. N. Chizhevskaya, and N. N. Glagoleva, *Liquid Semiconductors* (Nauka, Moscow, 1967; Plenum, New York, 1969).
2. M. Cutler, *Liquid Semiconductors* (Academic, New York, 1977).
3. *Liquid Metals*, Ed. by R. Evans and D. A. Greenwood (AIP, New York, 1977; Metallurgiya, Moscow, 1980).
4. R. Barrue and J. C. Perron, Phys. Lett. A **89A**, 305 (1982).
5. V. Ya. Prokhorenko, B. I. Sokolovskii, and V. A. Alekseev, Phys. Status Solidi B **113**, 453 (1982).
6. J. C. Perron and R. Barrue, Z. Phys. Chem., Neue Folge **157**, 623 (1988).
7. H. Ikemoto, I. Yamamoto, T. Tsuzuki, and H. Endo, J. Non-Cryst. Solids **205–207**, 347 (1996).
8. T. Yamaguchi, H. Ohtani, and F. Yonezawa, J. Non-Cryst. Solids **250**, 437 (1999).
9. S. Takeda, S. Ohno, and S. Tamaki, J. Phys. Soc. Jpn. **40**, 113 (1976).
10. S. Ohno and S. Harada, J. Phys. Soc. Jpn. **49**, 188 (1980).
11. F. Kakinuta and S. Ohno, J. Phys. Soc. Jpn. **50**, 1951 (1981).
12. M. Tagashi, T. Okada, and S. Ohno, J. Phys. Soc. Jpn. **56**, 3609 (1987).
13. A. C. Barnes, D. Laundy, and J. E. Enderby, Philos. Mag. B **55**, 497 (1987).
14. N. F. Mott and R. S. Allgaer, Phys. Status Solidi **21**, 343 (1967).
15. B. Cabane and J. Friedel, J. Phys. (Paris) **32**, 813 (1971).
16. C. Bichara, J.-Y. Raty, and J.-P. Gaspard, J. Non-Cryst. Solids **205**, 361 (1996).
17. N. F. Mott, Philos. Mag. **24**, 1 (1971).
18. J. Friedel, Nuovo Cimento Suppl. **7**, 287 (1958).
19. P. W. Anderson, Phys. Rev. **124**, 41 (1961).
20. Yu. Plevachuk and V. Sklyarchuk, Meas. Sci. Technol. **12**, 23 (2001).
21. S. Ohno, J. Phys. Soc. Jpn. **55**, 295 (1986).
22. A. Animalu, *Intermediate Quantum Theory of Crystalline Solids* (Prentice Hall, Englewood Cliffs, N.J., 1977; Mir, Moscow, 1981).
23. J. M. Ziman, *Principles of the Theory of Solids*, 2nd ed. (Cambridge Univ. Press, London, 1972; Mir, Moscow, 1974).
24. Y. Katayama, O. Shimomura, and K. Tsuji, J. Non-Cryst. Solids **250**, 537 (1999).
25. Y. Kavakita, M. Yao, and H. Endo, J. Non-Cryst. Solids **250**, 447 (1999).

Translated by I. Zvyagin

Semiconductors, Vol. 38, No. 12, 2004, pp. 1369–1373. Translated from Fizika i Tekhnika Poluprovodnikov, Vol. 38, No. 12, 2004, pp. 1414–1418.

ELECTRONIC AND OPTICAL PROPERTIES OF SEMICONDUCTORS

$Hg_{1-x-y-z}Cd_xMn_yZn_zTe$: A New Alternative to $Hg_{1-x}Cd_xTe$

I. N. Gorbatyuk, A. V. Markov, S. É. Ostapov^, and I. M. Rarenko

Fed'kovich National University, Chernivtsy, 58012 Ukraine

^e-mail: ostap@chv.ukrpack.net

Submitted December 15, 2003; accepted for publication April 6, 2004

Abstract—The results of studying the most important energy-band parameters of a new quinary semiconductor HgCdMnZnTe solid solution are reported. It is shown that the parameters of HgCdMnZnTe can make this material highly competitive with HgCdTe, which is the main material for infrared photoelectronics in the spectral ranges 3–5 and 8–14 μm. © *2004 MAIK "Nauka/Interperiodica".*

1. INTRODUCTION

The compound HgCdTe remains today the main material for infrared optoelectronics, owing to its unique physical properties [1, 2]. By varying the composition of the solid solution, one can obtain HgCdTe with a band gap in the range 0–1.6 eV. One extremely important aspect of this compound is the very small difference between the lattice constants of CdTe and $Cd_{0.2}Hg_{0.8}Te$, which makes it possible to use these materials to form epitaxial structures. The high mobility of charge carriers in HgCdTe makes it possible to design devices with a very fast response [3].

The main drawback of HgCdTe is the weakness of the Hg–Te chemical bond, which gives rise to a large number of mercury vacancies and to difficulties in ensuring the stable behavior of the surfaces and interfaces in the structures. These problems can certainly be solved in part by using the existing technology; in this case, however, the cost of the material obtained increases severalfold.

Thus, the search for ways to improve the stability and homogeneity of HgCdTe crystals or the synthesis of HgCdTe analogues with a higher quality and more stable crystal lattice remains very important. This aim can be attained by introducing elements with an ionic radius smaller than that in HgCdTe into the solid solution, which would stabilize the Hg–Te crystal-lattice bond. Specifically, Mn and Zn can play the role of such isovalent elements; the ionic radii of Mn and Zn (1.39 and 1.3 Å) are much smaller than that of Cd (1.56 Å) [4–6].

Taking into account all the above, we believe that the quinary $Cd_xMn_yZn_zHg_{1-x-y-z}Te$ (CdMnZnHgTe) solid solution with a low content of both manganese and zinc (1–7%) should be more advantageous than HgCdTe in that it has (i) a higher temporal and thermal stability, (ii) a higher structural quality, and (iii) better properties of the surface and interfaces.

In this paper, we report features of the growth and preparation of CdMnZnHgTe crystals and the results of studying the energy-band parameters of this solid solution.

2. PREPARATION OF CRYSTALS AND DETAILS OF EXPERIMENTS

2.1. Preparation of Crystals

The CdMnZnHgTe crystals were grown by the modified floating-zone method from preliminarily synthesized homogeneous polycrystalline ingots 15–20 mm in diameter and 15–18 cm in length. In order to synthesize the solid solutions, we used the starting components Cd, Te, Zn, and Hg with a purity of at least 99.9999%; the Mn component had a purity of 99.998% and was additionally purified using double vacuum distillation.

The samples for studying the optical, electrical, and mechanical properties were cut from wafers that had thickness of 500–600 μm and were cut from the ingot perpendicularly to the growth direction. The damaged layer formed as a result of cutting and grinding was removed by polishing with ASM 2/1 and ASM 1/0 diamond pastes. Chemical–mechanical polishing was used for final treatment of the surface [7]. All the crystals grown had *p*-type conductivity.

2.2. Studies of Microhardness

An increase in the microhardness may be a qualitative indication that the Hg–Te bond becomes stronger and the crystal lattice of the material is stabilized in the presence of Mn and Zn. While no on questions the stabilizing effect of Zn on the crystal lattice of materials of the HgCdTe type, there is no general agreement among researchers as to the effect of manganese. Despite theoretical predictions of an increase in the Hg–Te bond energy in the presence of Mn [8], no direct experimental evidence of this effect has been obtained so far. Moreover, Grangler *et al.* [9], who studied the effect of

Table 1. Microhardness of $Hg_{1-x-y-z}Cd_xMn_yZn_zTe$ crystals with different compositions at $T = 300$ K

Composition of crystals ($E_g = 0.15$ eV)	H, kg/mm^2	Composition of crystals ($E_g = 0.3$ eV)	H, kg/mm^2
$Hg_{0.8}Cd_{0.2}Te$	37.6 ± 1.3	$Hg_{0.7}Cd_{0.3}Te$	47.3 ± 1.6
$Hg_{0.82}Cd_{0.16}Mn_{0.02}Te$	41.0 ± 1.4	$Hg_{0.73}Cd_{0.24}Mn_{0.03}Te$	50.1 ± 1.6
$Hg_{0.82}Cd_{0.15}Mn_{0.02}Zn_{0.01}Te$	43.6 ± 1.1	$Hg_{0.73}Cd_{0.23}Mn_{0.03}Zn_{0.01}Te$	53.7 ± 1.0
$Hg_{0.84}Cd_{0.11}Mn_{0.04}Zn_{0.01}Te$	46.5 ± 0.7	$Hg_{0.76}Cd_{0.17}Mn_{0.06}Zn_{0.01}Te$	57.5 ± 0.95

manganese on the mechanical properties (including microhardness) of wide-gap $Cd_xMn_{1-x}Te$ crystals, concluded that the crystal bonds were destabilized in II–VI crystals in the presence of Mn^{2+} ions with a 10% content.

At the same time, an increase in microhardness was observed in $Cd_xMn_{1-x}Te$ crystals with an Mn content as high as 40% [10, 11].

In this context, we studied the microhardness of CdMnZnHgTe crystals with different contents of manganese and zinc and compared the results with those obtained for HgCdTe and $Hg_{1-x-y}Cd_xMn_yTe$ crystals with approximately the same band gap. The studies were performed at room temperature using the Vickers method. The results averaged over 12–15 measurements are listed in Table 1.

As can be seen from Table 1, the microhardness of the crystals studied increases as the content of both zinc and manganese increases even if the mercury content increases (from 80 to 84% in the case of $E_g = 0.15$ eV and from 70 to 76% in the case of $E_g = 0.3$ eV). These results clearly indicate that the crystal-lattice bonds in mercury-containing materials of the HgCdTe type become stronger in the presence of small amounts (up to 5%) of both Zn and Mn.

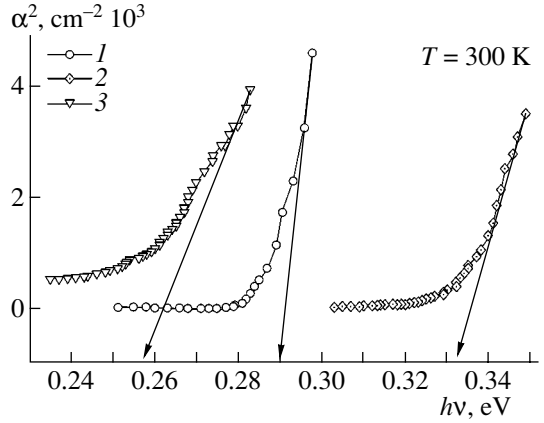

Fig. 1. Optical-absorption spectra of three $Hg_{1-x-y-z}Cd_xMn_yZn_zTe$ samples with (*1*) $x = 0.215$, $y = 0.031$, and $z = 0.02$; (*2*) $x = 0.212$, $y = 0.04$, and $z = 0.02$; and (*3*) $x = 0.178$, $y = 0.02$, and $z = 0.01$.

2.3. Determination of the Band Gap

The band gap of the crystals obtained was determined from the optical-absorption curves shown in Fig. 1 and from the temperature dependences of the Hall constant and electrical conductivity. The results obtained using the different methods are in good agreement with each other.

The band gaps determined using the above methods for three samples (see Fig. 1) were equal to $E_g = 0.291$ eV for sample 1, $E_g = 0.332$ eV for sample 2, and $E_g = 0.257$ eV for sample 3.

3. THEORETICAL CALCULATIONS

The main energy-band parameters of a quaternary $Hg_{1-x-y}Cd_xMn_yTe$ solid solution were calculated using the method suggested in [12]. According to this method, an arbitrary energy-band parameter of a multicomponent solid solution can be represented as a combination of two of its constituents. For the quaternary solid solution under consideration, any energy-band parameter A can be expressed as

$$A(Hg_{1-x-y}Cd_xMn_yTe) = 0.5A(Hg_{1-u}Cd_uTe) + 0.5A(Hg_{1-w}Mn_wTe), \quad (1)$$

where $u = 2x$ and $w = 2y$. According to this method, the band gap of $Hg_{1-x-y-z}Cd_xMn_yZn_zTe$ was calculated as

$$E_g(Hg_{1-x-y-z}Cd_xMn_yZn_zTe) = 0.5E_g(Hg_{1-x-2y}Cd_xMn_{2y}Te) + 0.5E_g(Hg_{1-x-2z}Cd_xZn_{2z}Te). \quad (2)$$

The values of the band gap calculated using formula (2) were compared with experimental data at room temperature. The results are listed in Table 2.

As can be seen, the suggested method for calculating the energy-band parameters also ensures good agreement with experiment for the quinary solid solution.

Calculating the energy from the bottom of the conduction band, we can use the Kane model [13] to obtain the following expression for the electron concentration in the conduction band:

$$n = \frac{2N_c}{\sqrt{\pi}}\int_0^\infty \frac{z^{1/2}(1+z/\Phi)^{1/2}(1+2z/\Phi)dz}{1+\exp(z-\eta)}. \quad (3)$$

Here, N_c is the effective density of states in the conduction band, $\Phi = E_g/k_BT$ is the reduced band gap, and $\eta = F/k_BT$ is the reduced Fermi energy. In this case, the effective electron mass at the bottom of the conduction band is given by

$$m_e^* = m_0\left[1 + E_P\frac{E_g + 2\Delta/3}{E_g(E_g + \Delta)}\right]^{-1}. \quad (4)$$

Here, $E_P = 2m_0P^2/\hbar^2$ and is typically equal to 18–19 eV in semiconductors of the HgCdTe type; Δ is the magnitude of the spin–orbit splitting of the bands. As a rule, the values of Δ are in the range 0.95–1.08 eV [4, 13].

The hole concentration in the valence band was calculated using the following conventional formula:

$$p = 4\pi\left(\frac{2k_BTm_{hh}^*}{h^2}\right)^{3/2}F_{1/2}(\eta + \Phi). \quad (5)$$

Here, m_{hh}^* is the effective mass of heavy holes and $F_{1/2}(\eta + \Phi)$ is the Fermi–Dirac integral. The values of E_P, spin–orbit splitting Δ, and the effective mass of heavy holes were assumed to be equal to $E_P = 18$ eV, $\Delta = 1$ eV, and $m_{hh}^* = 0.55m_0$ in the calculations.

The effective mass of electrons in CdMnZnHgTe in the case of complete degeneracy was calculated using the formula [13]

$$\left(\frac{m_e^*}{1 - m_e^*}\right)^2 = 32.5\times10^{-32}E_g^2/P^4 + 8.27\times10^{-30}n_i^{2/3}/P^2, \quad (6)$$

where P is the matrix element of the angular-momentum operator and n_i is the intrinsic concentration. Since we assumed that $E_P = 18$ eV, we have $P = 8.28\times10^{-8}$ eV cm. This value of P ensured the best agreement between the results of calculations and experimental data. Note that the values of P in the range from 8.2×10^{-8} to 8.5×10^{-8} eV cm are characteristic of HgCdTe-type semiconductors [4].

4. DISCUSSION

The results of calculating the concentration of intrinsic charge carriers n_i and the corresponding experimental data (triangles, circles, and squares) are shown in Fig. 2. It can be seen that theoretical curves are in good agreement with experimental values in the region of intrinsic conductivity. In our opinion, the $Hg_{1-x-y-z}Cd_xMn_yZn_zTe$ sample with $x = 0.14$, $y = 0.014$, and $z = 0.01$ is of particular interest. According to the concentration values and the shape of the curve, the range of intrinsic conductivity extends in this sample to 100 K, which, in turn, indicates that the defect concentration is low and, accordingly, that the HgMnZnCdTe crystals obtained are of high quality. The calculated $n_i(T)$ dependences for the other samples studied also show good agreement with experiment; however, the region of intrinsic conductivity can be distinguished in experimental curves only at $T > 180$ K for these samples.

Table 2. Band gap of the $Hg_{1-x-y-z}Cd_xMn_yZn_zTe$ crystals under study at $T = 300$ K

Sample no.	Composition	E_g, eV theory (2)	E_g, eV experiment
1	$x = 0.215$, $y = 0.031$, $z = 0.02$	0.301	0.291
2	$x = 0.212$, $y = 0.04$, $z = 0.02$	0.321	0.332
3	$x = 0.178$, $y = 0.02$, $z = 0.01$	0.260	0.257

For comparison, Fig. 2 also shows the temperature dependences of the intrinsic-carrier concentrations for $Hg_{0.8}Cd_{0.2}Te$ (curve *A*) and $Hg_{0.7}Cd_{0.3}Te$ (curve *B*); these concentrations were calculated using an empirical formula for the intrinsic-carrier concentration in HgCdTe [14]. It can be seen that the $Hg_{1-x-y-z}Cd_xMn_yZn_zTe$ sample with $x = 0.14$, $y = 0.014$, and $z = 0.01$ corresponds in the intrinsic-carrier concentration to $Hg_{0.8}Cd_{0.2}Te$; however, this sample corresponds to $Hg_{0.817}Cd_{0.183}Te$ with respect to the band gap. Similarly, $Hg_{1-x-y-z}Cd_xMn_yZn_zTe$ ($x = 0.21$, $y = 0.025$, and $z = 0.012$) exhibits almost the same carrier concentration as $Hg_{0.7}Cd_{0.3}Te$ and almost the same band gap as $Hg_{0.72}Cd_{0.28}Te$.

Thus, the intrinsic-carrier concentration in HgCdMnZnTe is somewhat lower than in HgCdTe with an identical band gap.

In Fig. 3, we illustrate the behavior of the Fermi level for the crystals studied. It can be seen that almost all these crystals are not degenerate. The $Hg_{1-x-y-z}Cd_xMn_yZn_zTe$ crystal with $x = 0.14$, $y = 0.014$, and $z = 0.01$ is an exception; in this case, the Fermi level is within the conduction band at $T > 170$ K. Such behavior should be

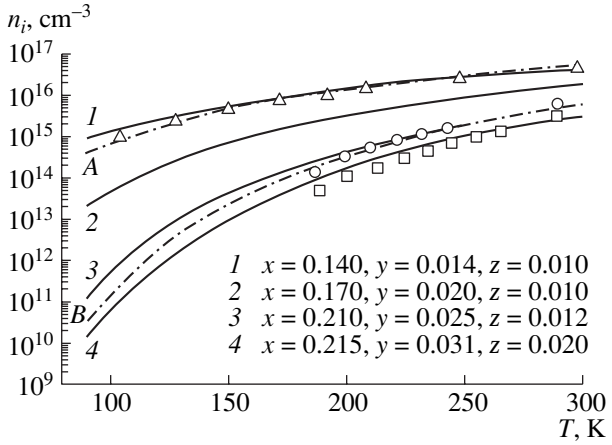

Fig. 2. Temperature dependences of the intrinsic-carrier concentration in the $Hg_{1-x-y-z}Cd_xMn_yZn_zTe$ samples with different compositions. The dash–dotted lines represent the results of calculations for (*A*) $Hg_{0.8}Cd_{0.2}Te$ and (*B*) $Hg_{0.7}Cd_{0.3}Te$ solid solutions.

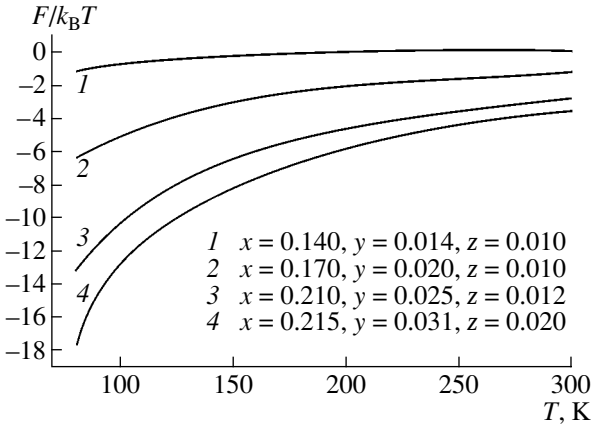

Fig. 3. Temperature dependences of the reduced Fermi level for the $Hg_{1-x-y-z}Cd_xMn_yZn_zTe$ crystals under study.

expected since this HgCdMnZnTe crystal corresponds (as was mentioned above) to $Hg_{1-x}Cd_xTe$ ($x = 0.183$) with respect to the band gap; as a result, the temperature dependence of the Fermi level should be similar for both of these compounds.

It is also of interest to compare the effective electron masses in HgCdMnZnTe with those in HgCdTe for the crystals with identical band gaps. In Table 3, we list the results of calculations and (for comparison) experimental data [15] at room temperature. It can be seen from Table 3 that the effective electron masses in HgCdMnZnTe are somewhat larger than in HgCdTe; as manganese and zinc content increases, the difference between effective masses increases. This finding is consistent with the conclusion made by Nesmelova [16] who compared the electron effective masses in the HgMnTe and HgCdTe solid solutions. In Table 4, we compare our results with those obtained in [16] at T = 300 K. It can be seen that the effective electron masses in HgCdMnZnTe are somewhat (about 15%) smaller than those in HgMnTe. The significant discrepancy between theory and experiment for the samples with $E_g = 0.054$ eV was also reported by Lowney *et al.* [14] (again, theoretical results exceeded experimental data). Apparently, the cause of this discrepancy is the fact that the theory used is hardly applicable to the situation where the value of E_g approaches zero.

Thus, the introduction of manganese and zinc into a HgCdTe solid solution leads not only to an increase in microhardness of four- and five-component compounds but also to a decrease in the intrinsic-carrier concentration and an increase in the effective electron mass.

5. CONCLUSIONS

Thus, the following results were obtained in this study.

(i) The modified floating-zone method was used to grow single crystals of a new $Hg_{1-x-y-z}Cd_xMn_yZn_zTe$ semiconductor solid solution with different Mn and Zn contents.

(ii) The microhardness of the crystals obtained was studied. It was shown that microhardness increases as

Table 3. Comparison of effective electron masses in the $Hg_{1-x-y-z}Cd_xMn_yZn_zTe$ and $Hg_{1-x}Cd_xTe$ crystals at T = 300 K

Composition of HgCdMnZnTe crystal	E_g, eV	Carrier concentration N, cm^{-3}	m_e/m_0, calculation (6)	m_e/m_0, theory [15]	m_e/m_0, experiment [15]	HgCdTe composition [15]
$x = 0.14$, $y = 0.014$, $z = 0.01$	0.131	2.4×10^{18}	0.049	0.045	0.049	0.18
$x = 0.166$, $y = 0.02$, $z = 0.01$	0.182	6.7×10^{17}	0.034	0.035	0.033	0.22
$x = 0.16$, $y = 0.03$, $z = 0.02$	0.223	2.8×10^{18}	0.052	0.049	0.048	0.25

Note: The values of x for $Cd_xHg_{1-x}Te$ solid solutions with almost the same values of E_g are given in the last column on the right.

Table 4. Comparison of effective electron masses in the $Hg_{1-x-y-z}Cd_xMn_yZn_zTe$ and $Hg_{1-x}Mn_xTe$ crystals at T = 300 K

Composition of HgCdMnZnTe crystal	E_g, eV	Carrier concentration N, cm^{-3}	m_e/m_0, calculation (6)	m_e/m_0, theory [16]	m_e/m_0, experiment [16]	HgMnTe composition [16]
$x = 0.092$, $y = 0.01$, $z = 0.01$	0.054	1.5×10^{17}	0.019	0.019	0.0162	0.06
$x = 0.14$, $y = 0.014$, $z = 0.01$	0.131	6.0×10^{16}	0.017	0.0194	–	0.09
$x = 0.16$, $y = 0.015$, $z = 0.01$	0.158	5.5×10^{17}	0.031	0.0345	0.036	0.1

Note: The values of x for the $Hg_{1-x}Mn_xTe$ solid solutions with almost the same values of E_g are given in the last column on the right.

the content of Mn and Zn in the crystals increases, which indicates that the crystal-lattice bonds in mercury-containing materials of the HgCdTe type become stronger if small amounts (up to 5–7%) of both Zn and Mn are introduced.

(iii) Temperature dependences of the intrinsic-carrier concentration in $Hg_{1-x-y-z}Cd_xMn_yZn_zTe$ were calculated. Good agreement between the results of calculations and experimental data is obtained in the region of intrinsic conductivity. The theory used in calculations is applicable to $Hg_{1-x-y-z}Cd_xMn_yZn_zTe$ compounds with $x \lesssim 0.3$, $y \lesssim 0.1$, and $z \lesssim 0.1$ in the temperature range $50\ \mathrm{K} \lesssim T \lesssim 300\ \mathrm{K}$.

(iv) The effective masses of electrons in nondegenerate and degenerate materials were calculated. It was shown that an increase in the content of manganese and zinc in the solid solution leads to an increase in the effective electron mass and to a decrease in the intrinsic-carrier concentration.

REFERENCES

1. J. Piotrowski and A. Rogalski, Sens. Actuators A **67**, 146 (1998).
2. M. A. Kinch, J. Electron. Mater. **29**, 809 (2000).
3. A. Rogalski, Infrared Phys. Technol. **43**, 187 (2002).
4. A. Rogalski, Infrared Phys. **31**, 117 (1991).
5. A. Rogalski, Prog. Quantum Electron. **13**, 299 (1989).
6. N. G. Gluzman, N. K. Lerinman, L. D. Sabirzyanova, *et al.*, Fiz. Tekh. Poluprovodn. (Leningrad) **23**, 1032 (1989) [Sov. Phys. Semicond. **23**, 644 (1989)].
7. N. D. Raranskiĭ, I. M. Rarenko, V. P. Shafranyuk, *et al.*, in *Abstracts of III Meeting on Schools of Higher Education Complex Program: X-rays* (Chernovtsy, USSR, 1989), p. 174.
8. A. Wall, C. Captile, and A. Franciosi, J. Vac. Sci. Technol. A **4**, 818 (1986).
9. R. Grangler, A. Lasbley, S. Rolland, *et al.*, J. Cryst. Growth **88**, 682 (1988).
10. I. Rarenko, E. Rybak, Y. Stetsko, and Z. Zakharuk, in *Abstracts of EMRS Spring Meeting* (Strasbourg, Germany, 1995), D-III, p. 409.
11. P. M. Bridenbaugh, Mater. Lett. **3** (7–8), 287 (1985).
12. O. A. Bondaruk, A. V. Markov, S. É. Ostapov, *et al.*, Fiz. Tekh. Poluprovodn. (St. Petersburg) **34**, 430 (2000) [Semiconductors **34**, 415 (2000)].
13. J. J. Schmit, J. Appl. Phys. **41**, 2876 (1970).
14. J. R. Lowney, D. G. Seiler, C. L. Littler, and I. T. Yoon, J. Appl. Phys. **71**, 1253 (1992).
15. I. M. Nesmelova, *Optical Properties of Narrow-Gap Semiconductors* (Nauka, Novosibirsk, 1992) [in Russian].
16. I. M. Nesmelova, Fiz. Tekh. Poluprovodn. (St. Petersburg) **37**, 1296 (2003) [Semiconductors **37**, 1257 (2003)].

Translated by A. Spitsyn

Semiconductors, Vol. 38, No. 12, 2004, pp. 1374–1377. Translated from Fizika i Tekhnika Poluprovodnikov, Vol. 38, No. 12, 2004, pp. 1419–1422.

ELECTRONIC AND OPTICAL PROPERTIES OF SEMICONDUCTORS

Stimulated and Spontaneous Emission of $Cd_xHg_{1-x}Te$ Structures in the Range 3.2–3.7 μm at 77 K

Yu. N. Nozdrin*, A. V. Okomel'kov*^, A. P. Kotkov^^, A. N. Moiseev**, and N. D. Grishnova****

**Institute for Physics of Microstructures, Russian Academy of Sciences, Nizhni Novgorod, 603950 Russia*

^e-mail: okom@ipm.sci-nnov.ru

***Institute of High-Purity Substances, Russian Academy of Sciences, Nizhni Novgorod, 603950 Russia*

^^e-mail: kotkov@ihps.nnov.ru

Submitted May 5, 2004; accepted for publication May 17, 2004

Abstract—Stimulated emission of radiation from $Cd_xHg_{1-x}Te$ samples pumped by a Nd:YAG laser at temperature $T \approx 77$ K is obtained. Both spontaneous and stimulated emission is observed for the wavelengths λ in the range 3300–3600 nm. Experimental emission spectra are presented. The special features of the spectra and the possible applications of the structures are discussed. © *2004 MAIK "Nauka/Interperiodica".*

1. INTRODUCTION

There is currently great interest worldwide in the fabrication of active emitting devices (lasers) and photodetectors that operate in the middle and far infrared (IR) ranges (λ ≈ 3–20 μm). Mastering this wavelength range is of interest, particularly for

(1) communication purposes, since this range includes the Earth's atmospheric transparency windows (3.5–4 μm, 4.5–5 μm, 8–14 μm, and 16–23 μm);

(2) spectroscopy and environment monitoring, since this range includes the frequencies of vibrational–rotational transitions of many molecules.

Among the few active devices that can really function within this region are semiconductor laser diodes and quantum cascade lasers. Given the principle on which they operate, both devices incorporate highly inhomogeneous structures. These are *p–n* junctions in laser diodes and quantum superlattices with a fairly large number (usually from one to several tens) of quantum-confinement layers in quantum cascade lasers. This circumstance complicates the production of the devices and increases their cost. As is well known, the characteristic frequencies of radiative band-to-band transitions in films of narrow-gap semiconductors, for example, $Cd_xHg_{1-x}Te$, can fall within the operation range of quantum cascade lasers. Moreover, it is now common practice to synthesize CdHgTe samples with a stoichiometry such that the characteristic frequencies of radiative band-to-band transitions (defined by the band gap E_g) come right in the middle IR region. CdHgTe may be considered as a promising material as the source of stimulated radiation since it is a direct-gap semiconductor (direct radiative band-to-band transitions are allowed). The carrier lifetime may be rather long there (if the band gap is quite wide).

From this point of view, if CdHgTe-based lasers were designed for a fairly broad range of stoichiometric compositions, they could compete with cascade lasers. A single CdHgTe film is much easier to handle than the quantum superlattice of a cascade laser. A CdHgTe film itself represents a waveguide in view of the high permittivity of the CdHgTe material (15–20), which can be conducive to the formation of cavity modes due to the total internal reflection from the film boundaries. Furthermore, in contrast to the structures of quantum cascade lasers, there is no need to grow quantum-confinement layers with the use of high-precision technology here, since the typical thickness of CdHgTe films usually ranges from several to several tens of micrometers. The technology of high-quality epitaxial CdHgTe films has now been developed in detail due to the production of IR photodetectors based on them. The main methods currently used for growing CdHgTe films are liquid-phase epitaxy, molecular-beam epitaxy, and metal–organic chemical vapor deposition (MOCVD). As experimental samples, we used structures grown at the Institute of High-Purity Substances, Russian Academy of Sciences, where an MOCVD method for growing epitaxial CdHgTe layers with various stoichiometric compositions is being developed [1, 2].

Until now, there are only a few studies dedicated to CdHgTe-based lasers, and most of the main questions remain to be clarified (for example, how far is it possible to move towards longer wavelengths and higher temperatures). For the first time, the spontaneous and coherent emission of radiation from a $Cd_xHg_{1-x}Te$ crystal optically pumped by a GaAs diode laser was observed in [3] (see also [4, 5]). Stimulated radiation was observed in the range λ = 3.8–4.1 μm at temperature $T \approx 12$ K, and spontaneous radiation was detected up to 15 μm.

Hartman [6] reported on optically pumped lasers operating in the range 1.25–2.97 μm at the liquid-nitrogen temperature. Continuous-wave lasing at 2.79 μm took place at 12 K. Stimulated emission was observed for CdHgTe films with $x = 0.5$ at 2.13 μm [7]. In this case, the lasing threshold was ~10 kW/cm^2 at the liquid-nitrogen temperature.

Mahavadi *et al*. [8] reported stimulated emission from CdHgTe films with $x = 0.46$ grown on a semi-insulating CdTe substrate and subjected to Nd:YAG-laser pumping: generation at 2.42 μm had a power of above 2.8 kW/cm^2 at 10 K.

As can be seen from the data presented above, the longest wavelength of stimulated radiation at the liquid-nitrogen temperature was 2.97 μm. This circumstance is conventionally associated with the fact that, at narrower band gaps (for comparatively small x, $x \approx 0.2$ and smaller), the relative role of nonradiative transitions attributed to Auger recombination increases (see [9]), although apparently the lasing frequency may be limited by nonradiative recombination via impurities. Evidently, with higher-quality and purer samples, one can hope to obtain a lasing effect for longer wavelengths as well. However, an important unsolved problem is the optimization of the thickness of the sample. Our experimental data suggest that, in the CdHgTe films under study, the emission of electromagnetic radiation at lower frequencies can be obtained at considerably higher temperatures than before.

2. RESULTS AND DISCUSSION

In this study, we measured the characteristics of electromagnetic radiation obtained from epitaxial $Cd_xHg_{1-x}Te$ layers pumped by a Nd:YAG laser (λ = 1.064 μm) at the liquid-nitrogen temperature. We used the $Cd_xHg_{1-x}Te$ samples with thicknesses from several micrometers to several tens of micrometers on semi-insulating GaAs substrates with a high-resistivity CdTe buffer layer. The samples placed at a copper heat sink were photoexcited on the side of the epitaxial layer. A metal spherical mirror focused the radiation from the edge of the epitaxial layer onto the entrance slit of a conventional monochromator. The output signal was detected by a photodetector kept at the liquid-nitrogen temperature. As a photodetector, we also used $Cd_xHg_{1-x}Te$ samples with an appropriate stoichiometric composition. When required, the scattered pump radiation was suppressed by Ge filters placed in front of the photodetector. The signal from the photodetector was applied to an oscilloscope synchronized with the Nd:YAG laser pulse.

Figure 1 shows one of the emission spectra (in the form of the photodetector signal versus the wavelength) obtained for the $Cd_xHg_{1-x}Te$ (MST 638/1) sample with $x \approx 0.376$ and thickness $h \approx 8.9$ μm at 77 K; the p-type sample was grown on a (111)-oriented GaAs substrate. The sample was shaped like an equilateral triangle with sides of ~5 mm. For the optical pump intensity $P <$ 4 kW/cm^2, the spectrum is shaped like a wide low pedestal, which is shown by the dashed line in Fig. 1. At $P \gtrsim 4$ kW/cm^2, a narrow line appears against the pedestal background. It is reasonable to associate the pedestal with spontaneous radiation and the narrow line, with stimulated radiation (superluminescence). Thus, we observed that the emission spectrum narrowed when the photoexcitation exceeded a certain threshold, which in our case was $P \approx 4$ kW/cm^2.

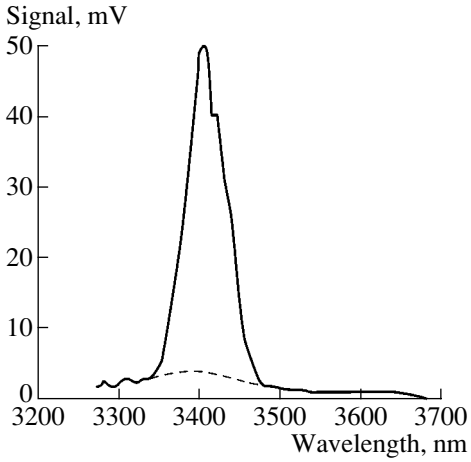

Fig. 1. Emission spectrum for the $Cd_xHg_{1-x}Te$ sample (MST 638/1, $x \approx 0.376$) at $T \approx 77$ K. The photodetector is the MST 641/1 sample, $x \approx 0.272$. Dashed and solid lines show the spectra at the photoexcitation below ($P < 4$ kW/cm^2) and above ($P \geq 4$ kW/cm^2) the threshold, respectively.

This value best agrees with the result reported in [8], where the stimulated radiation line corresponded to $\lambda \approx$ 2420 nm and had a width that nearly coincides with that of the line shown in Fig. 1. It is important to note that the measurements in [8] were carried out at $T = 12$ K, while our experiments were performed at $T \geq 77$ K. The fact that a six- or sevenfold difference in temperature has almost no effect on the line width ($\Delta\lambda \approx$ 50–60 nm) confirms the stimulated nature of this radiation.

In our experiments, various surface regions were illuminated, rather than the entire surface of the sample at once. Therefore, we actually measured the superluminescence spectra from different illuminated areas of the surface. The reliable observation of simulated radiation (even in the absence of a cavity) is an indication of the high gain in the system. This fact is consistent with the theoretical estimate [10] that indicates that the gain α can be as high as ~10^3 cm^{-1}.

Figure 2 shows the emission spectra of various samples each fabricated from a $Cd_xHg_{1-x}Te$ film with $x \approx$ 0.376, as well as the spectral lines obtained upon the illumination of different parts of the same sample. These spectral lines are seen to differ in their peak position λ_{max}, as well as in their width and shape. The values of λ_{max} related to different areas differ by ~3.6%, which suggests that the $Cd_xHg_{1-x}Te$ film under study is inhomogeneous: the corresponding fluctuations of its composition (nonstoichiometry) should vary from 3 to 4%.

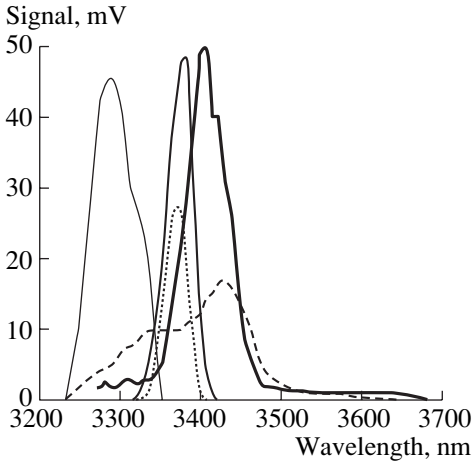

Fig. 2. Emission spectra of different samples (MST 638/1, $x \approx 0.376$) fabricated from the same $Cd_xHg_{1-x}Te$ film.

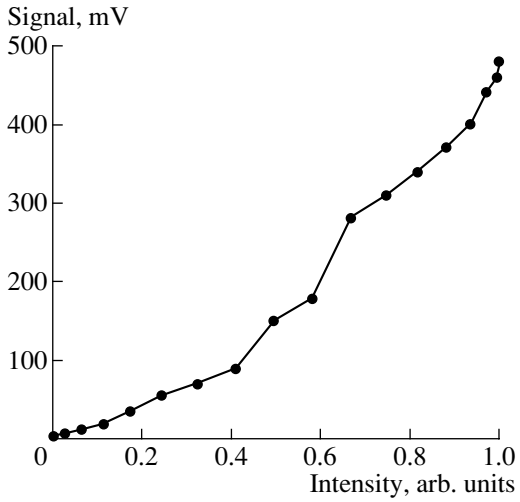

Fig. 3. Intensity of radiation at $T = 77$ K vs. the pump intensity for the $Cd_xHg_{1-x}Te$ sample (MST 638/1, $x \approx 0.376$).

Another indication of the spatial inhomogeneity of the film is the observed "improper" shape of the line (see, e.g., the dashed spectrum in Fig. 2). The spread in the conditions of photoexcitation (illumination of neighboring dissimilar areas) results in the inhomogeneous broadening of the superluminescence line.

Let us consider a simple estimation of the temperature dependence of the spontaneous spectrum line width for a spatially homogeneous sample in the case of an abrupt absorption edge. It is known (see, e.g., [11]), that the photoluminescence (spontaneous radiation) intensity can be expressed as

$$I_{\mathrm{PL}}(\hbar\omega) \propto \begin{cases} (\hbar\omega - E_g)^{1/2} \exp\left(-\dfrac{\hbar\omega - E_g}{k_B}\right) \\ \text{at } \hbar\omega > E_g, \\ 0 \text{ at } \hbar\omega < E_g. \end{cases}$$

We can use this expression to estimate the width of the spontaneous-emission line width as

$$\Delta(\hbar\omega) \approx (2\text{–}3)k_BT. \quad (1)$$

At the liquid-nitrogen temperature of our experiment, this formula yields a line width (in temperature terms) approximately equal to 160–240 K.

Evidently, formula (1) gives the minimal value of the spontaneous line width, since the possible heating of the sample is disregarded. In our experiment (and in [8]), the typical intensities were fairly high. Recall that the lasing threshold was observed at the pumping intensity $P \approx 4$ kW/cm^2. Another possible cause of the spontaneous line broadening is the spatial inhomogeneity of the $Cd_xHg_{1-x}Te$ solid solution (and, hence, the spatial inhomogeneity of the band gap).

In terms of temperature, the half-width (the width at the peak's half-height, $0.5I_{\max}$) of the spectral line and the pedestal in Fig. 1 is ~86 and ~400 K, respectively. These estimates indicate that the line is two to three times narrower than the value predicted for an "ideal" photoluminescence line and, therefore, cannot represent spontaneous radiation. Furthermore, the spectral width of the pedestal is larger than the "ideal" estimation, so that the pedestal can be attributed to spontaneous radiation. Note once again that, in all the studies available (see, e.g., [3, 6–8]), the spectrum appears just like a narrow line of stimulated radiation against the background of a broad pedestal governed by spontaneous radiation.

Figure 3 shows the emission intensity for the $Cd_xHg_{1-x}Te$ sample (MST 638/1, $x \approx 0.376$) as measured at $T = 77$ K by the detector with the band gap corresponding to the wavelength ~6 μm versus the optical pump intensity. It can be seen that the dependence is nonlinear but has a fairly smooth appearance. Thus, in order to find a clear manifestation of the lasing threshold, one should analyze the corresponding spectral dependences.

3. CONCLUSIONS

The width of the superluminescence spectrum shown in Fig. 1 almost coincides with the value reported in study [8]. However, in contrast to our results, the emission in [8] was obtained at a lower temperature ($T = 12$ K) and corresponded to a shorter wavelength ($\lambda_{\max} \approx 2420$ nm). Melngailis and Strauss [3] observed lines of stimulated emission in the region of $\lambda \approx 4100$ nm but also at $T = 12$ K. Thus, in this paper, we apparently report for the first time the observation of stimulated emission from the $Cd_xHg_{1-x}Te$ structures at 77 K in the wavelength range $\lambda \approx 3250$–3450 nm. The observation of stimulated emission at 77 K makes it possible to state that these structures are promising in the context of various applications. Note especially that the observed variations of the superluminescence frequency for different regions of the same sample can be

used to detect stoichiometric nonuniformities. This possibility is important for improving the technology of $Cd_xHg_{1-x}Te$ structures. In turn, the better quality of these structures will lead to a narrower spectrum of stimulated radiation.

ACKNOWLEDGMENTS

We thank A.A. Andronov for his interest in this study and helpful discussions.

REFERENCES

1. A. N. Moiseev, A. P. Kotkov, V. V. Dorofeev, and N. D. Grishnova, Neorg. Mater. **40** (1), 1 (2004).
2. K. O. Boltar', N. I. Yakovleva, V. P. Golovin, *et al.*, Prikl. Fiz., No. 5, 95 (2003).
3. I. Melngailis and A. J. Strauss, Appl. Phys. Lett. **8** (7), 179 (1966).
4. R. Dornhaus and G. Nimtz, Springer Tracts Mod. Phys. **78**, 1 (1978).
5. N. S. Baryshev, *Properties and Applications of Narrow-Gap Semiconductors* (UNIPRESS, Kazan, 2000) [in Russian].
6. T. C. Hartman, J. Electron. Mater. **8** (2), 191 (1979).
7. V. I. Ivanov-Omskiĭ, K. E. Mironov, R. B. Rustamov, and V. A. Smirnov, Pis'ma Zh. Tekh. Fiz. **10**, 1021 (1984) [Sov. Tech. Phys. Lett. **10**, 428 (1984)].
8. K. K. Mahavadi, J. Bleuse, X. Chu, and J. P. Faurie, Appl. Phys. Lett. **55**, 1285 (1989).
9. G. Nimtz, Phys. Rep. **63**, 265 (1980).
10. G. M. Genkin, A. V. Okomel'kov, and I. D. Tokman, Fiz. Tekh. Poluprovodn. (Leningrad) **22**, 2151 (1988) [Sov. Phys. Semicond. **22**, 1358 (1988)].
11. P. Yu and M. Cardona, *Fundamentals of Semiconductors* (Springer, Berlin, 1996; Fizmatlit, Moscow, 2002), p. 312.

Translated by A. Sidorova

Semiconductors, Vol. 38, No. 12, 2004, pp. 1378–1380. Translated from Fizika i Tekhnika Poluprovodnikov, Vol. 38, No. 12, 2004, pp. 1423–1425.

ELECTRONIC AND OPTICAL PROPERTIES OF SEMICONDUCTORS

Photoluminescence of Electron–Hole Plasma in Semi-Insulating Undoped GaAs

V. F. Kovalenko and S. V. Shutov

Institute of Semiconductor Physics, Kherson Branch, National Academy of Sciences of Ukraine, Kherson, 73008 Ukraine

Submitted August 14, 2003; accepted for publication May 20, 2004

Abstract—The dependence of the photoluminescence spectrum of electron–hole plasma in semi-insulating undoped GaAs on the concentration of the background carbon impurity N_C (3×10^{15} cm$^{-3} \le N_C \le 4 \times 10^{16}$ cm^{-3}) is studied at 77 K. It is established that the density of the electron–hole plasma, which is equal to $n_{e-h} \approx 1.1 \times 10^{16}$ cm^{-3} in crystals with the lowest impurity concentration at an excitation intensity of 6×10^{22} photons/(cm^2 s), decreases considerably as the value of N_C increases in the range mentioned above. A decrease in the density of the electron–hole plasma with increasing N_C is attributed to the effect of fluctuations in the carbon concentration N_C, which give rise to a nonuniform distribution of interacting charge carriers and to localization of holes in the tails of the density of states of the valence band. © *2004 MAIK "Nauka/Interperiodica".*

The photoluminescence (PL) of electron–hole plasma (EHP) and electron–hole drops in direct- and indirect-gap semiconductors, respectively, has been mainly studied in high-purity materials, so the conditions $N < n_{e-h}$ and $N < n_{ex}$ (N, n_{e-h}, and n_{ex} are the concentrations of the impurity, electron–hole pairs, and excitons, respectively) at high excitation levels were satisfied; as a result, collective interactions between nonequilibrium charge carriers appeared [1–6].

It is evident that an increase in N should enhance the screening effect of impurity atoms on the charge carriers and weaken the interaction between the charge carriers. It seems likely that the magnitude of this effect may depend on the electrical properties of the material, the degree of compensation, and the distribution of the impurity potential. However, the possible effect of these factors on the EHP in direct-gap semiconductors has been inadequately studied.

In this paper, we consider the dependence of the EHP PL intensity in semi-insulating undoped GaAs that includes impurity-potential fluctuations on the concentration of the background carbon impurity N_C. The electrical characteristics of the samples under study and the method for measuring the PL spectra were reported previously [7]. The excitation level J was changed from 3×10^{21} to 6×10^{22} photons/(cm^2 s) by varying the operation current of an Ar laser.

It was shown previously [7] that the edge-emission band in the PL spectra of semi-insulating undoped GaAs crystals that contain background carbon with the concentration N_C and are subjected to a low-intensity excitation ($J \le 3 \times 10^{21}$ photons/(cm^2 s)) is formed by the band-to-band transitions of interacting charge carriers at $N_C \le 1.4 \times 10^{16}$ cm^{-3}. At higher values of N_C, this band is related to recombination of free electrons with holes localized at the tails of the density of states of the valence band; these tails are caused by fluctuations in the doping-impurity concentration.

As the excitation-intensity increased ($J > 3 \times 10^{21}$ photons/(cm^2 s)), the spectrum of the edge-emission PL was modified. This modification is characteristic of radiative recombination in the EHP: the band peak (the energy corresponding to the peak $h\nu = h\nu_m$) shifted to longer wavelengths, and the band broadened and changed shape. In addition, the short-wavelength falloff of the PL intensity became less steep (Fig. 1), which was indicative of recombination of hot charge carriers whose temperature at the highest excitation intensity was estimated from the slope of the short-wavelength falloff and increased from 87 to 96 K as N_C increased in the range 3×10^{15} cm$^{-3} \le N_C \le 4 \times 10^{16}$ cm^{-3} under study.

The emission spectrum of some of the crystals at the highest excitation levels exhibited peaks (Fig. 1) that were evidently caused by the initiation of stimulated emission. The most substantial modification of the spectrum occurred in the crystals with the smallest values of N_C. As the carbon concentration increases, the spectrum modification is no longer observed at $N_C \approx 2.8 \times 10^{16}$ cm^{-3}, as follows from the extrapolation of the N_C dependences of the peak energy $h\nu_m(N_C)$ and the band width $W(N_C)$ at various excitation levels (Fig. 2).

In Fig. 3, we show the dependence of the EHP density n_{e-h} at $J = 6 \times 10^{22}$ photons/(cm^2 s) on the carbon concentration estimated from the effective-potential approximation using the formula [4]

$$E_g' = E_g - \frac{3e^2}{\pi\varepsilon}(3\pi^2 n_{e-h})^{1/3},$$

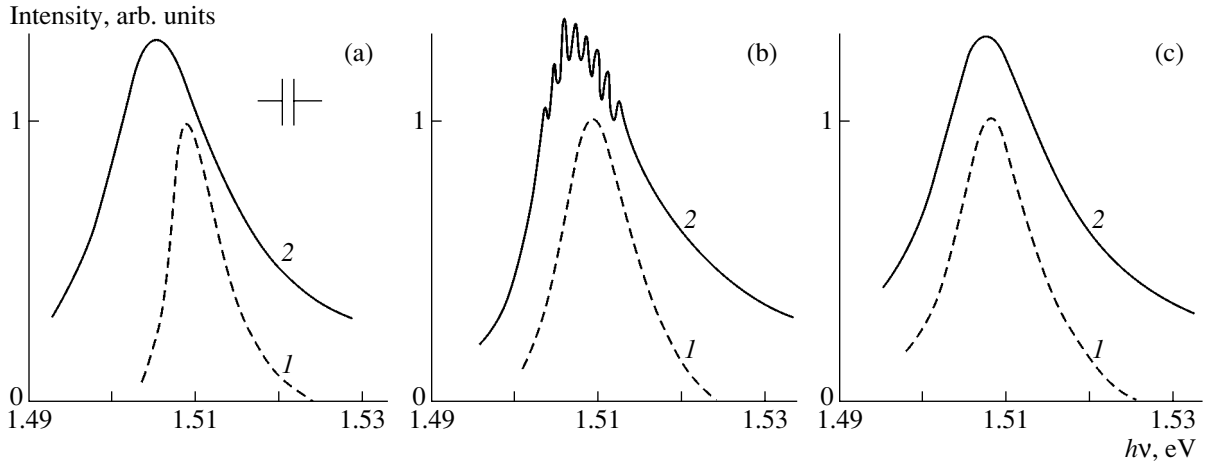

Fig. 1. Excitation-level dependences of the edge-PL spectra for GaAs crystals with different carbon concentrations N_C at $T = 77$ K. The excitation intensity was $J = (1)\ 3 \times 10^{21}$ and $(2)\ 6 \times 10^{22}$ photons/(cm^2 s). N_C = (a) 3.5×10^{15}, (b) 9×10^{15}, and (c) 2.1×10^{16} cm^{-3}. The spectra were normalized to unity and were shifted arbitrarily along the vertical axis.

where E_g' is the band gap narrowed as a result of collective electron–hole interaction, E_g is the unperturbed band gap, $\varepsilon = 12$ is the relative dielectric constant of GaAs, and e is the elementary charge. When estimating, we assumed that $E_g' = h\nu_m$ and we decreased the value of E_g at $N_C \geq 1.4 \times 10^{16}$ cm^{-3} by the depth of the percolation level for electrons and holes $\gamma' = (2/3)\gamma$ is the depth of potential wells formed by fluctuations in the carbon concentration).

As expected, the $n_{e-h}(N_C)$ dependence shown in Fig. 3 indicates that the EHP density decreases as N_C increases; this decrease is larger than that of electron–hole drops in Ge [8]. In our opinion, the main factor causing the substantial decrease in the EHP density as N_C increases is the presence of fluctuations in the doping-impurity concentration that give rise to a nonuniform distribution of interacting charge carriers. Localization of holes within the tails of the density of states of the valence band at $N_C \geq 1.4 \times 10^{16}$ cm^{-3} occurs in times that are shorter than the lifetimes of nonequilibrium charge carriers τ (according to our estimations, $\tau \leq 1.3 \times 10^{-11}$ s at the highest excitation intensity, which is

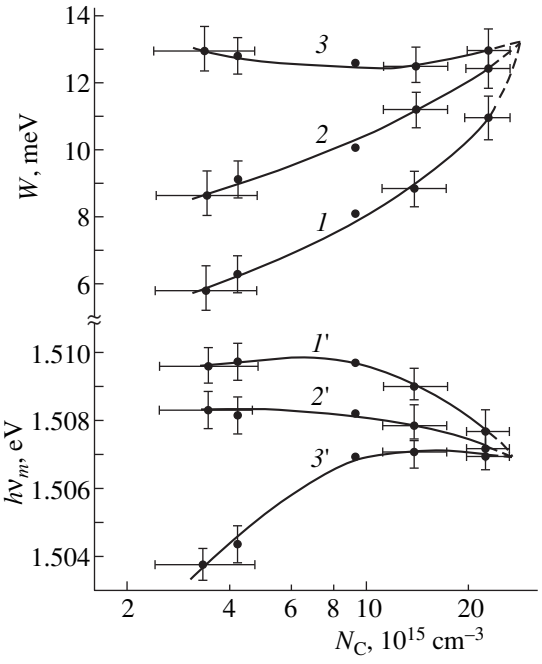

Fig. 2. Dependences of the (*1*–*3*) width W and (*1*'–*3*') the peak energy $h\nu_m$ of the edge-PL spectrum on the carbon concentration N_C at different excitation intensities J at $T = 77$ K. $J = (1, 1')\ 3 \times 10^{21}$, $(2, 2')\ 2 \times 10^{22}$, and $(3, 3')\ 6 \times 10^{22}$ photons/(cm^2 s).

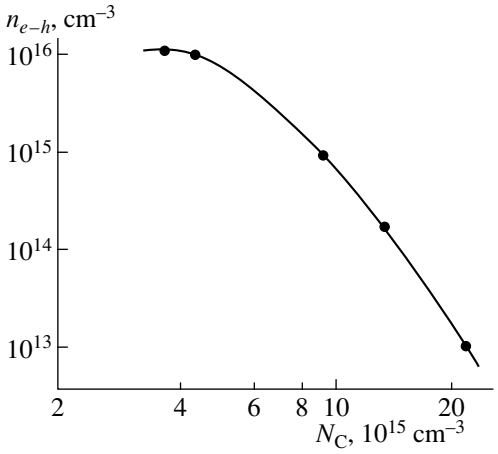

Fig. 3. Density of the electron–hole plasma as a function of the carbon concentration at the excitation intensity $J = 6 \times 10^{22}$ photons/(cm^2 s) and $T = 77$ K.

consistent with the values of τ in semi-insulating undoped GaAs, as reported previously [9]). This localization reduces the fraction of the charge carriers that are involved in the formation of the electron–hole plasma. The latter circumstance reduces the density of the electron–hole plasma even further.

REFERENCES

1. V. B. Stopachinskiĭ, Zh. Éksp. Teor. Fiz. **72**, 592 (1977) [Sov. Phys. JETP **45**, 310 (1977)].
2. V. S. Bagaev, L. I. Paduchikh, and G. S. Sakhonenko, in *Excitons in Semiconductors* (Nauka, Moscow, 1971), p. 54 [in Russian].
3. V. G. Lysenko, V. I. Revenko, T. G. Tratas, and V. B. Timofeev, Zh. Éksp. Teor. Fiz. **68**, 335 (1975) [Sov. Phys. JETP **41**, 163 (1975)].
4. T. Moriya and T. Kushida, J. Phys. Soc. Jpn. **43**, 1646 (1977).
5. M. N. Vinoslavskiĭ and A. V. Kravchenko, Fiz. Tekh. Poluprovodn. (St. Petersburg) **35**, 390 (2001) [Semiconductors **35**, 377 (2001)].
6. I. A. Vashchenko, B. S. Kerner, V. V. Osipov, and V. F. Sinkevich, Fiz. Tekh. Poluprovodn. (Leningrad) **23**, 1378 (1989) [Sov. Phys. Semicond. **23**, 857 (1989)].
7. V. F. Kovalenko, M. B. Litvinova, and S. V. Shutov, Fiz. Tekh. Poluprovodn. (St. Petersburg) **36**, 174 (2002) [Semiconductors **36**, 167 (2002)].
8. D. L. Smith, Solid State Commun. **18**, 637 (1976).
9. N. M. Litovchenko and L. G. Shepel', Optoélektron. Poluprovodn. Tekh., No. 29, 108 (1995).

Translated by A. Spitsyn

Semiconductors, Vol. 38, No. 12, 2004, pp. 1381–1383. Translated from Fizika i Tekhnika Poluprovodnikov, Vol. 38, No. 12, 2004, pp. 1426–1428.

SEMICONDUCTOR STRUCTURES, INTERFACES, AND SURFACES

Effect of Hydrogen Sulfide on Photoelectric Characteristics of Al–*n*-Si–SnO_2:Cu–Ag Isotype Heterostructures

S. V. Slobodchikov†, E. V. Russu, É. V. Ivanov, Yu. G. Malinin, and Kh. M. Salikhov

Ioffe Physicotechnical Institute, Russian Academy of Sciences, Politekhnicheskaya ul. 26, St. Petersburg, 194021 Russia

Submitted May 12, 2004; accepted for publication May 17, 2004

Abstract—Electrical and photoelectric properties of Al–*n*-Si–SnO_2:Cu–Ag heterostructures are studied. It is established that the charge transport in this structure is caused by double injection of charge carriers in the diffusion approximation. A 35% increase in the photocurrent is observed after exposing the heterostructure to a mixture of 1% of H_2S with N_2. The initial values of the photocurrent are recovered if the heterostructure is subsequently exposed to air. The rise and decay times of the photosignal are relatively short: 1 and 3 min, respectively. *© 2004 MAIK "Nauka/Interperiodica".*

1. INTRODUCTION

Tin dioxide (SnO_2) is widely used in the production of detectors of hydrogen sulfide H_2S, methane CH_4, and a number of other gases; the electrical conductivity of SnO_2 changes in the atmosphere of the above gaseous compounds [1, 2]. One serious disadvantage of these sensors is that it is necessary to heat the sensitive SnO_2 layer to a temperature of 300–400°C. In addition, the selectivity of SnO_2-based detectors does not always meet present-day requirements.

In this context, we recently suggested a fundamentally new method of H_2S detection [3] that is based on the variation in the photosensitivity of SnO_2-based structures exposed to H_2S. The potential of this method was illustrated for the first time with the example of anisotype Al–*p*-Si–SnO_2:Cu–Ag heterostructures [3]. In this paper, we report the results of studying the electrical and photoelectric characteristics of Al–*n*-Si–SnO_2:Cu–Ag isotype structures as applied to the problem of H_2S detection.

The technology for fabricating structures with both *p*-Si and *n*-Si is quite similar and was described in detail in our previous publication [3]. Silicon with *n*-type conductivity and a (100) crystallographic orientation was used as the substrate for the Al–*n*-Si–SnO_2:Cu–Ag structures.

2. RESULTS AND DISCUSSION

We measured the current–voltage (*I–V*) characteristics, spectral dependences of photovoltage, and the dependences of photocurrent on the time the structure was exposed to a gaseous mixture of nitrogen and hydrogen sulfide for the samples of Al–*n*-Si–SnO_2:Cu–Ag heterostructures. The volume concentration of H_2S amounted to 1%. All measurements were performed at room temperature (20–25°C).

The energy-band diagram of the structure under study is shown in Fig. 1.

2.1. Electrical Characteristics of Heterostructures

In Fig. 2 we show the dependence of the current *J* on the forward bias *U* with the negative voltage applied to *n*-Si; this dependence is characteristic of the samples that were not exposed to hydrogen sulfide.

In the range of currents from 10^{-7} to 10^{-4} A, the $J(U)$ curve can be approximated by the expression

$$J = J_0 \exp[qU/(\nu kT)] \quad \text{with} \quad \nu \approx 10, \qquad (1)$$

where all designations are conventional. It follows from (1) that the charge transport in the heterostructure is not controlled either by the diffusion current in the neutral base region (since in that case $\nu \approx 1$) or by the generation–recombination current in the space-charge region (in that case, we should have $\nu \approx 2$). Therefore, the charge transport should be controlled by one of the types of double injection of charge carriers into the space-charge region [4].

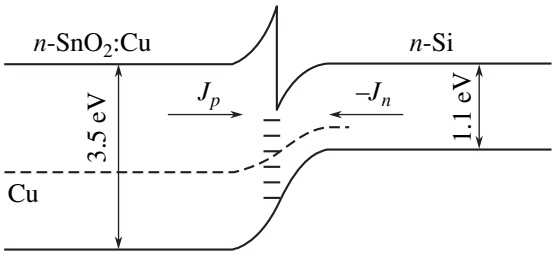

Fig. 1. Energy-band diagram of an Al–*n*-Si–SnO_2:Cu–Ag isotype heterostructure.

†Deceased.

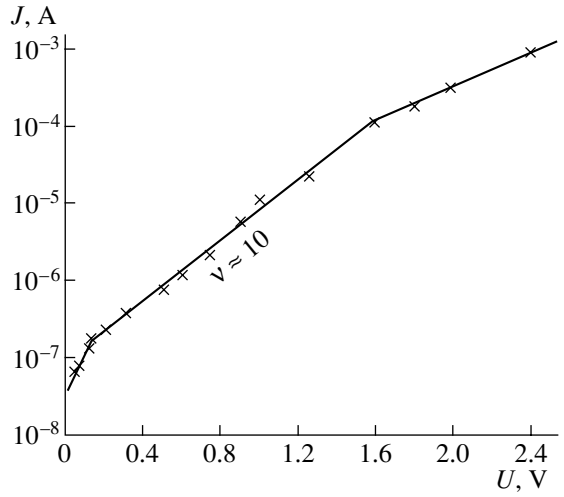

Fig. 2. Current–voltage characteristic of the heterostructure under forward bias before exposure to hydrogen sulfide.

Since the double injection corresponds to a power-law dependence of the current on voltage in the drift approximation, analytical expression (1) describes the double injection in the diffusion approximation. Note that $\nu = \cosh(w/L_A)$, where w and L_A are the width of the space-charge region and the ambipolar-diffusion length, respectively.

The presence of a compensating Cu level can give rise to the attachment of holes. It follows from an analysis of formula (1) that, at $J_p/J < 1$ and $J_n/J \approx 1$ (here, J_p and J_n are the hole and electron currents, respectively), the effect of the hole attachment on the shape of the *I–V* characteristic is insignificant since the electron current flows predominantly through the isotype heterostructure under consideration.

When considering the plasma injected into the semiconductor when the diffusion current is predominant, we can write the following equation that expresses the law of conservation for the number of particles [5]:

$$(2kT/q)d^2n/dx^2 \approx (b + 1)b/(\mu_n\tau). \qquad (2)$$

Here, $b = \mu_n/\mu_p$ and all other designations are conventional. The solution of Eq. (2) indicates that the function $n(x)$ falls off exponentially. It is important that the charge carriers injected into the semiconductor are expected to be concentrated in the region with a depth on the order of $L_A = [(2kT/q)\mu_n\tau/(b + 1)]^{1/2}$.

Our previous studies of the Al–*p*-Si–SnO_2:Cu–Ag anisotype heterostructures [3] showed that the changes in the *I–V* characteristics observed after exposing the samples to a gaseous mixture consisting of H_2S (1%) and N_2 were small compared to the changes in photosensitivity. Similar results were obtained previously for various structures that incorporated a palladium contact and were exposed to hydrogen (see, for example, [6]). Taking this circumstance into consideration, we did not perform experiments to clarify the effect of H_2S on the electrical characteristics of Al–*n*-Si–SnO_2:Cu–Ag isotype heterostructures.

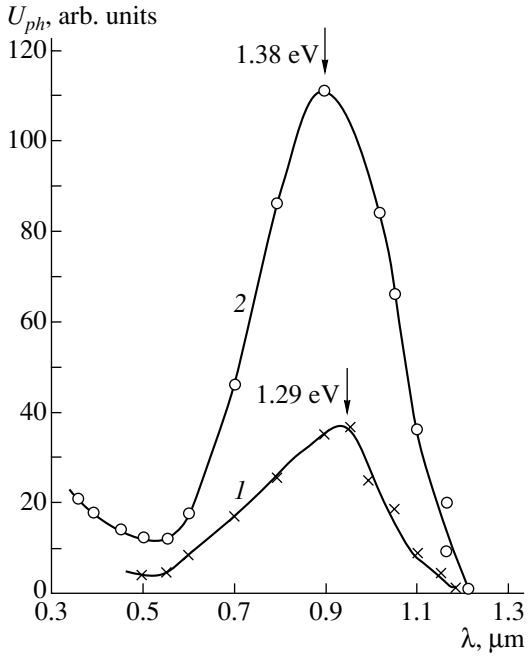

Fig. 3. Spectral photosensitivity of the heterostructure (*1*) before and (*2*) after exposure to a gaseous mixture consisting of 1% of H_2S and N_2.

2.2. Photoelectric Characteristics of the Heterostructures

In Fig. 3 we show two spectral dependences of photosensitivity measured before (curve *1*) and after (curve *2*) exposing the structure to the 1%-H_2S/N_2 mixture with subsequent exposure to air. These dependences were measured under conditions of open-circuit photovoltage.

The exposure to hydrogen sulfide gives rise to a shift of the spectral photosensitivity curve to shorter wavelengths by 0.09 eV and leads to an appreciable increase in the photovoltage. These results can be interpreted in the following way.

Akimov *et al.* [7] studied the effect of hydrogen sulfide on the electrical conductivity of SnO_2 films doped with copper. It was established that chemical reactions that involve copper and sulfur proceeded both at the surface and in the bulk of the SnO_2:Cu layer exposed to hydrogen sulfide. As a result, multicomponent chemical compounds were formed, whose composition was not identified. We may assume that similar processes occur in the case under consideration.

The space-charge region in *n*-Si contains a copper impurity whose concentration decreases as the distance from the heteroboundary increases (as the substrate is approached). Therefore, compounds composed of sulfur and copper can appear in this region as a result of

exposure to hydrogen sulfide; these compounds are expected to exhibit a larger gradient in their distribution than that of the initial copper impurity. If these compounds are neutral or exhibit a low activity with respect to the capture of nonequilibrium charge carriers, the recombination rate at the interface where the concentration of the sulfur–copper compounds is highest decreases. In turn, this circumstance gives rise to a shift of the spectral photovoltage curve to shorter wavelengths.

Apparently, the increase in the absolute value of photovoltage observed experimentally should be related to the corresponding variation in the barrier height at the *n*-Si–SnO_2:Cu interface.

It is worth noting that similar spectral dependences of photovoltage were observed previously for the Al–*p*-Si–SnO_2:Cu–Ag anisotype heterostructures [3]. An important difference between those curves and the curves obtained in this study is the following. Absolute values of the photovoltage for anisotype heterostructures were an order of magnitude smaller than those for isotype heterostructures. This result indicates that the contribution of the surface states to the recombination process is small in the case of an Al–*n*-Si–SnO_2:Cu–Ag heterostructure.

A diagram illustrating the variation in the photocurrent J_{ph} in relation to the time t is shown in Fig. 4. This time dependence was observed for an Al–*n*-Si–SnO_2:Cu–Ag heterostructure in a hydrogen sulfide atmosphere (region I) and in air (region II) and was measured in the short-circuit mode. The Al–*n*-Si–SnO_2:Cu–Ag heterostructure was installed in a special gas-filled cell. Optical radiation was introduced into the cell through a sapphire window. An incandescent lamp with a power of 60 W, which was mounted at a distance of 30 cm from the sample, served as the radiation source.

The photocurrent started to increase as the (1%-H_2S)/N_2 gaseous mixture was introduced into the cell. In about 1 min, the photosignal attained a steady-state value and then remained unchanged. The increase in the photocurrent amounted to ~35% with respect to its initial value. After the hydrogen sulfide was pumped out of the cell and atmospheric air was introduced, the photocurrent recovered the value it had before the sample was exposed to the (1%-H_2S)/N_2 mixture. The signal-relaxation time was 3–4 min. The above processes were completely reproducible in the admission–removal series for the H_2S-containing mixture.

The above results differ not only quantitatively but also qualitatively from the corresponding data obtained previously for Al–*p*-Si–SnO_2:Cu–Ag anisotype heterostructures [3]. For these heterostructures, a decrease in the photocurrent as a result of exposure to hydrogen sulfide was observed; the initial value of the photocurrent was recovered after subsequent exposure of the heterostructure to air. The characteristic time constants were equal to 10–20 min [3].

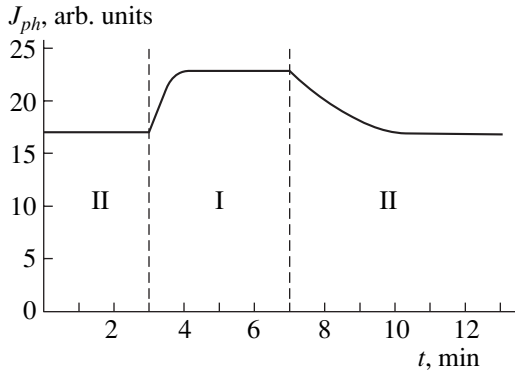

Fig. 4. Kinetics of variations in the photocurrent for the heterostructure illuminated using an incandescent lamp (region I, in an atmosphere of (1% H_2S)/N_2; region II, in air).

3. CONCLUSION

Thus, our experiments made it possible to study the electrical and photoelectric characteristics of Al–*n*-Si–SnO_2:Cu–Ag isotype heterostructures. We observed and studied a variation in the photosensitivity of the heterostructures under consideration as a result of exposure to hydrogen sulfide. In this context, the following special features are important: a significant increase in the photosignal amplitude, small time constants, the reversibility of physical processes, and the possibility of operating at room temperature. The results obtained show that the heterostructures under study might be promising as components for the fabrication of H_2S sensors.

REFERENCES

1. W. Gopel, Prog. Surf. Sci. **20**, 9 (1985).
2. *Solid State Gas Sensors*, Ed. by P. T. Moseley and B. C. Tofield (Hilger, Bristol, 1987), p. 51.
3. S. V. Slobodchikov, E. V. Russu, É. V. Ivanov, *et al.*, Fiz. Tekh. Poluprovodn. (St. Petersburg) **38**, 1234 (2004) [Semiconductors **38**, 1198 (2004)].
4. É. I. Adirovich, P. M. Karageorgiĭ-Alkalaev, and A. Yu. Leĭderman, in *Double-Injection Currents in Semiconductors* (Sovetskoe Radio, Moscow, 1973), Chap. 2, p. 55 [in Russian].
5. M. A. Lampert and P. Mark, *Current Injection in Solids* (Academic, New York, 1970; Mir, Moscow, 1973), Chap. 13, p. 289.
6. G. G. Kovalevskaya, L. Kratena, M. M. Meredov, *et al.*, Pis'ma Zh. Tekh. Fiz. **15** (12), 55 (1989) [Sov. Tech. Phys. Lett. **15**, 478 (1989)].
7. B. A. Akimov, A. V. Albul, A. M. Gas'kov, *et al.*, Fiz. Tekh. Poluprovodn. (St. Petersburg) **31**, 400 (1997) [Semiconductors **31**, 335 (1997)].

Translated by A. Spitsyn

Semiconductors, Vol. 38, No. 12, 2004, pp. 1384–1389. Translated from Fizika i Tekhnika Poluprovodnikov, Vol. 38, No. 12, 2004, pp. 1429–1434.

SEMICONDUCTOR STRUCTURES, INTERFACES, AND SURFACES

Photoreflection Studies of Band Offsets at the Heterojunction in Strained Short-Period GaAs/GaAsP Superlattices

L. P. Avakyants*^, P. Yu. Bokov*, T. P. Kolmakova, and A. V. Chervyakov***

**Department of Physics, Moscow State University, Moscow, 119992 Russia*

^e-mail: avakants@genphys.phys.msu.ru

***OAO Optron, Moscow, 105318 Russia*

Submitted April 22, 2004; accepted for publication April 28, 2004

Abstract—Energies of band-to-band transitions with the involvement of the quantum-confinement subbands are determined from the photoreflection spectra of the strained short-period GaAs/$GaAs_{0.6}P_{0.4}$ superlattice. Strains caused by the mismatch of the crystal lattice in the GaAs and $GaAs_{0.6}P_{0.4}$ layers are calculated on the basis of the observed shift of the fundamental-transition energy in $GaAs_{0.6}P_{0.4}$. Positions of minibands in the superlattice are simulated in relation to the potential jump at the heteroboundary; the Kronig–Penney model is used in the calculations. Comparison of the results of simulation with experimental data shows that the studied superlattice is of type I with weakly localized electrons and light holes. The potential jump at the heteroboundary in the conduction band amounts to $\Delta E_c/\Delta E_g = 0.15$. © *2004 MAIK "Nauka/Interperiodica".*

1. INTRODUCTION

An improvement in the technology of the production of semiconductor heterostructures (HSs) has made it possible to grow films with a thickness of several nanometers without generating misfit dislocations. This circumstance allows one to grow defect-free HSs based on semiconductors with differing crystal-lattice parameters under the condition that the thickness of the layers does not exceed a certain critical value specified by the lattice mismatch [1]. Semiconductor layers in such HSs experience compressive and tensile strains, which leads to an additional modification of the energy-band structure of the layers [2, 3]. Optical properties of superlattices (SLs) with strained layers differ from those of so-called matched SLs. The positions of the energy levels in strained SLs are affected not only by the width of the quantum wells and the thickness of barriers but also by the strains that appear in the layers as a result of the difference between the crystal-lattice constants of contacting materials. A variation in the composition of the well or barrier layers leads, on the one hand, to a variation in the band gap and, on the other hand, to a variation in the lattice constant and, consequently, to changes in the valence and conduction bands. The character of these variations depends on the sign of the strain.

Structures based on the GaAs/$GaAs_{1-x}P_x$ heterocontact are an example of strained HSs. In the case of strained HSs based on GaAs/$GaAs_{1-x}P_x$, the GaAs layers experience compressive strains, whereas $GaAs_{1-x}P_x$ layers experience tensile strains [4]. Recent studies [4, 5] showed that lasers that emit in the infrared and red spectral regions and are based on GaAs/$GaAs_{1-x}P_x$ strained HSs have better characteristics than similar devices fabricated on the basis of unstrained GaAs/$Al_xGa_{1-x}As$ HSs; specifically, lasers based on strained HSs have lower threshold currents and a higher quantum yield.

Note that for strained HSs the question of the value of the potential jump at the heteroboundary remains open. According to theoretical concepts [6], the conduction band in III–V compounds is formed by the ions of Group III elements; as a result, in GaAs/$GaAs_{1-x}P_x$ SLs where the composition of the Group-V ions varies, the major potential jump is located in the valence band (the so-called common-anion rule). However, it is believed in the majority of publications (see, for example, [7]) that up to 60% of the difference in the energies of fundamental transitions in GaAs and $GaAs_{1-x}P_x$ (as in the case of the GaAs/$Al_xGa_{1-x}As$ HS) is related to the conduction band.

In addition, the approximation according to which all stresses are concentrated only in a single layer (for example, in the layer that forms the barrier in a strained HS) is often used [4, 5, 8]. In the latter studies, experimental data were used to derive the dependence of the magnitude of the valence-band splitting in the barrier of the GaAs/$GaAs_{1-x}P_x$ HS on the phosphorus concentration. However, this approximation can be used only if the thicknesses of the layers that form the HS barrier are much smaller than the quantum-well width.

Gorya *et al.* [9] calculated the energy-band diagram of the GaAs/$GaAs_{1-x}P_x$ SL on the assumption that the potential jump in the conduction band is much smaller than the potential jump in the valence band. The authors of [9] consider that the bottom of the conduction band in the layers of the GaAs well and $GaAs_{1-x}P_x$ barrier in the heterostructure are separated from the vacuum level by electron affinity, which is generally valid only for

intrinsic semiconductors at $T = 0$ K; this leads to the conclusion that the SL under consideration is of type II.

In this paper, we report the results of using photoreflection spectroscopy to study the energies of band-to-band transitions in an SL based on GaAs/$GaAs_{1-x}P_x$. We calculate the interband-transition energies in the SL in the context of the Kronig–Penney periodic-potential model taking into account (i) the difference between the effective masses in the well and the barrier and (ii) the strains. In contrast to [4, 5, 8], we take into account that the energy-band structure of both the GaAs well and the $GaAs_{1-x}P_x$ barrier is modified as a result of strains. Based on the obtained data of photoreflection spectroscopy, we calculate the potential jump at the GaAs/$GaAs_{1-x}P_x$ heteroboundary taking into account both the strains in the SL layers and the common-anion rule.

2. EXPERIMENTAL

The sample under study was grown by liquid-phase epitaxy on a GaAs substrate with the (100) orientation and consisted of 20 alternating layers of GaAs and $GaAs_{1-x}P_x$ with identical thickness (7 nm). The phosphorus concentration in the barriers amounted to ~40%.

The photoreflection spectra were measured using the setup shown in Fig. 1. The emission of spectroscopic lamp *1* with a power of 30 W was resolved into a spectrum using the first monochromator of an MDR-6 system *2* and was then directed to sample *3*. The emission of a He–Ne laser *4* with a power of 1 mW was simultaneously directed onto the sample; this emission was modulated using a chopper *5*. The modulation frequency was 370 Hz. Reflected radiation was directed onto the second monochromator in the MDR-6 system *2* equipped with an additional entrance slit. The light from the exit slit of the second monochromator was directed onto an FDK-263 silicon photodiode *6*; the signal from the latter was amplified using a preliminary low-noise photoamplifier. The signal was then fed to the synchronous detector *7* of a Unipan-232B selective nanovoltmeter. The signal from photodiode *8* was applied to the reference-voltage input of the synchronous detector; the modulated radiation of laser *4* was directed onto this photodiode. Thus, the voltage at the output of the synchronous detector was proportional to the variation in the reflection coefficient R of sample *3* at the modulation frequency. A variation in the position of gratings in monochromator *2* and measurements of the photoreflection signal were performed using a microprocessor-based interface that was software-controlled by personal computer *9*.

The spectral width of the spread function of the monochromator amounted to 1 meV. The photoreflection spectra were measured at room temperature.

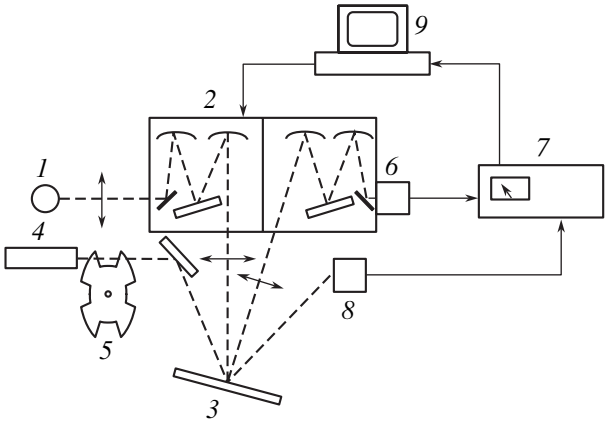

Fig. 1. Block diagram of experimental setup for measuring the photoreflection spectra. (*1*) Spectroscopic lamp, (*2*) MDR-6 double monochromator, (*3*) sample, (*4*) He–Ne laser, (*5*) chopper, (*6*) photodetector with a low-noise amplifier, (*7*) Unipan-232B selective nanovoltmeter, (*8*) photodetector of the reference signal, (*9*) computer with an interface module.

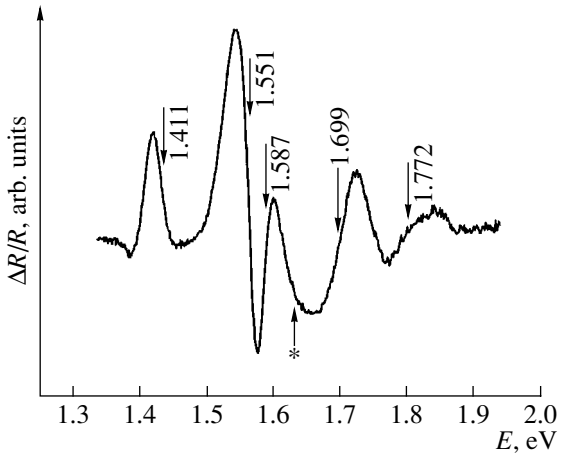

Fig. 2. Photoreflection spectrum of the GaAs/$GaAs_{0.6}P_{0.4}$ superlattice. Arrows indicate the observed transition energies in the superlattice.

3. RESULTS AND DISCUSSION

3.1. Positions of the Spectral Lines

The photoreflection spectrum of a GaAs/$GaAs_{1-x}P_x$ SL is shown in Fig. 2. The following lines are observed in the spectrum: a line peaked at 1.41 eV and caused by the presence of the GaAs substrate, a line peaked at 1.78 eV and related to the absorption edge of $GaAs_{1-x}P_x$, and a series of lines in the energy range from 1.53 to 1.78 eV that are caused by transitions between the SL minibands of the conduction and valence bands.

We determined the spectral-line positions by approximating the experimental data by the sum of the Aspnes expressions [10, 11] for the so-called low-field case,

$$\frac{\Delta R}{R}(E) = \mathrm{Re}[Ae^{i\varphi}(E - E_i + \Gamma)^{-m}], \qquad (1)$$

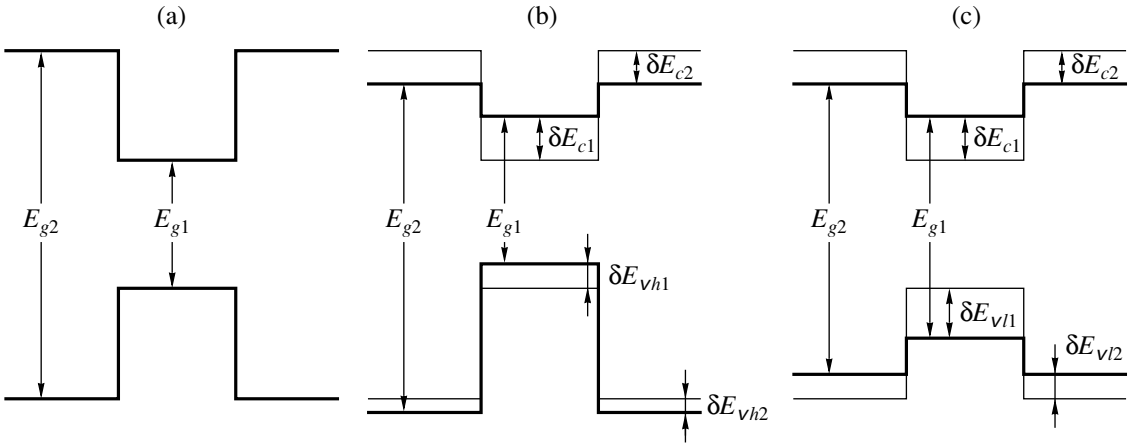

Fig. 3. Energy-band diagram of the quantum well for (a) matched and (b, c) mismatched heterocombinations with allowance for splitting of the valence band into the subbands of (b) heavy and (c) light holes. In a mismatched heterocombination, the crystal-lattice constant of the well exceeds that of the barrier.

where A and φ are the amplitude and phase factors, respectively; E is the probing-radiation energy; E_i is the position of a spectral feature; Γ is a phenomenological broadening parameter; and m is the parameter controlled by the type of critical point and by the order of the derivative of the permittivity $\varepsilon(E)$ with respect to energy. We used $m = 2$ [12].

As a result of the approximation of the spectrum by the sum of the Aspnes expressions, we determined the positions of the spectral lines as 1.411, 1.551, 1.587, 1.699, and 1.772 eV. The first and last lines are related to fundamental transitions in the GaAs substrate and the $GaAs_{1-x}P_x$ barrier.

Let us compare the obtained value of the band gap in the barrier with published data. The fundamental-transition energy in the unstrained $GaAs_{1-x}P_x$ layer is determined using the following expression suggested in [13]:

$$E_g(GaAs_{1-x}P_x) = 1.42 + 1.12x + 0.21x^2. \quad (2)$$

As a result, we find that the band gap $E_g = 1.902$ eV for $x = 0.4$, whereas the fundamental-transition energy determined by us (1.772 eV) is considerably lower. This discrepancy may be related to the presence of strains caused by the mismatch between the crystal-lattice constants of the GaAs well and the $GaAs_{1-x}P_x$ barrier.

3.2. Strain-Induced Variations in the Energy-Band Structure

As is well known [14], the presence of strains leads to a variation in the SL energy-band structure. For GaAs/$GaAs_{1-x}P_x$ SLs grown along the [100] direction, the layers of the GaAs well experience both uniform and uniaxial compression. Uniform compression leads to an increase in the band gap owing mainly to a shift of the conduction band. Uniaxial compression removes the valence-band degeneracy at the Γ point; as a result, an energy gap appears between the subbands of the heavy and light holes.

The strain-induced shifts of the conduction band δE_c and also of the subbands of the heavy holes δE_{vh} and light holes δE_{vl} in the valence band at the center of the Brillouin zone are determined from the expressions [7]

$$\delta E_c = 2a_c\varepsilon(C_{11} - C_{12})/C_{11}, \quad (3)$$

$$\delta E_{vh} = E_H + E_S, \quad (4)$$

$$\delta E_{vl} = E_H + \frac{1}{2}\Delta_0 - \frac{1}{2}E_S - \frac{1}{2}(\Delta_0^2 + 2\Delta E_S + 9E_S^2), \quad (5)$$

where

$$\varepsilon = (a_2 - a_1)/a_1, \quad (6)$$

$$E_H = 2a_v\varepsilon(C_{11} - C_{12})/C_{11}, \quad (7)$$

$$E_S = b\varepsilon(C_{11} + 2C_{12})/C_{11}. \quad (8)$$

Here, ε is the strain in the layer; a_c and a_v are the hydrostatic deformation potentials for the conduction and valence bands, respectively; b is the potential of uniaxial strains; C_{11} and C_{12} are the elastic constants; a_1 and a_2 are the crystal-lattice constants of the well and barrier layers, respectively; and Δ_0 is the spin–orbit splitting of a subband in the valence band. As a result of strains in the GaAs/$GaAs_{1-x}P_x$ SL, the bottom of the GaAs conduction band is shifted by δE_{c1} and increases the band gap in the well, whereas the bottom of the conduction band in $GaAs_{1-x}P_x$ is shifted by δE_{c2} in the opposite direction. The resulting variations in the conduction-band positions of GaAs and $GaAs_{1-x}P_x$ cause the depth of the quantum-well for electrons to decrease.

In Fig. 3 we show the energy-band diagrams of the quantum wells formed by (a) a matched heterocombination and (b, c) mismatched heterocombinations for which the quantum-well region experiences compressive strains and the barrier region experiences tensile

strains. The designations used in Fig. 3 (δE_{c1}, δE_{vh1}, δE_{vl1} and δE_{c2}, δE_{vh2}, ΔE_{vl2}) are the shifts of the well and barrier bands as a result of strains; these shifts were calculated using formulas (3)–(5) with the indices 1 and 2 denoting the layers of the GaAs well and the $GaAs_{1-x}P_x$ barrier, respectively.

Uniaxial stresses lead to the removal of degeneracy and to the appearance of an energy gap between the subbands of the heavy and light holes at the center of the Brillouin zone of the valence band. For example, the top of the heavy-hole subband of the valence band in the layer of the GaAs well is insignificantly shifted so that the band gap decreases, whereas the corresponding band in $GaAs_{1-x}P_x$ shifts in the opposite direction (Fig. 3). The opposite situation is observed for the subband of light holes. Thus, the resulting variations in the subbands of the GaAs and $GaAs_{1-x}P_x$ valence bands lead to an increase in the depth of the quantum well for heavy holes and to a decrease in that for light holes. As a result of the strain-induced variations in the band structure, the energies of transitions between the bottom of the conduction band and the top of the heavy-hole subband in the valence band and between the bottom of the conduction band and the top of the light-hole subband in the valence band increase in the well region and decrease in the barrier region in comparison with unstrained structures. Thus, in the vicinity of the fundamental absorption edge in strained semiconductor layers, one observes two energy gaps related to transitions from the conduction band to the subbands of the heavy holes $E_g^{str}(c\text{–}vh)$ and light holes $E_g^{str}(c\text{–}vl)$ in the valence band. The energies of these transitions can be determined from the following expressions:

$$E_g^{str}(c\text{–}vh) = E_g^{unstr} + \delta E_c + \delta E_{vh}, \quad (9)$$

$$E_g^{str}(c\text{–}vl) = E_g^{unstr} + \delta E_c + \delta E_{vl}. \quad (10)$$

Here, E_g^{unstr} is the band gap for the unstrained material.

Thus, a decrease in the $GaAs_{1-x}P_x$ band gap is caused by strains in the SL layers. The constants required for calculation of the energy-band structure using expressions (3)–(5) were reported previously [7, 15]. For the phosphorus content claimed by the manufacturer (40%), the strain-induced band gaps are 1.524 and 1.785 eV for the edge transitions between the conduction band and the heavy-hole subband in the valence band of GaAs and $GaAs_{0.6}P_{0.4}$, respectively; these energies are equal to 1.603 and 1.683 eV for similar transitions involving the light-hole subband in the valence band. We determined the phosphorus content x using the position of the spectral line (Fig. 2) related to the fundamental transition in the barrier. This content amounted to (39 ± 3)%, which is in good agreement with the data of the manufacturer.

3.3. The Effects of Spatial Quantization

A series of lines in the photoreflection spectrum in the range from 1.53 to 1.78 eV (Fig. 2) is related to transitions between the spatial-quantization subbands of the conduction and valence bands in the $GaAs/GaAs_{1-x}P_x$ SL. Since the observed spectral features are fairly narrow (when the spectrum is approximated using the least-squares method, the phenomenological broadening parameter in expression (1) is no larger than 20 meV), we believe that these features are caused by transitions between the conduction-band minibands and the heavy-hole subband in the valence band [6].

We now calculate the energies of the band-to-band transitions in the SL. The behavior of a particle is described in terms of the Kronig–Penney model for an infinite periodic rectangular SL potential [6, 16]. The position and width of the minibands are determined from the following transcendental equation based on the method of the envelope wave function:

$$\frac{k_2^2 - k_1^2}{k_2^2 k_1^2}\sinh(k_2 d_2)\sin(k_1 d_1) + \cosh(k_2 d_2)\cos(k_1 d_1) = \cos(k_z d_z). \quad (11)$$

Here,

$$k_1 = \frac{1}{\hbar}\sqrt{2m_1^* E}, \quad (12)$$

$$k_2 = \frac{1}{\hbar}\sqrt{2m_2^*(U - E)}, \quad (13)$$

where m_1^* and m_2^* are the effective masses of charge carriers in the SL well and barrier, respectively; U is the potential-well depth governed by the potential jump at the heteroboundary; d_1 and d_2 are the well and barrier width, respectively; and E is the particle energy. The wave vector k_z is defined within the first Brillouin minizone as

$$-\pi/d_z \le k_z \le \pi/d_z. \quad (14)$$

Thus, the range of the energies allowed in the SL can be determined from the relation

$$1 \le \frac{k_2^2 - k_1^2}{k_2^2 k_1^2}\sinh(k_2 d_2)\sin(k_1 d_1) + \cosh(k_2 d_2)\cos(k_1 d_1) \le 1. \quad (15)$$

The effective mass of charge carriers in the $GaAs_{1-x}P_x$ barrier depends on the ternary-compound composition as [7]

$$\begin{aligned} m_e/m_0 &= 0.067 + 0.103x, \\ m_{hh}/m_0 &= 0.62 + 0.17x, \\ m_{lh}/m_0 &= 0074 + 0.066x. \end{aligned} \quad (16)$$

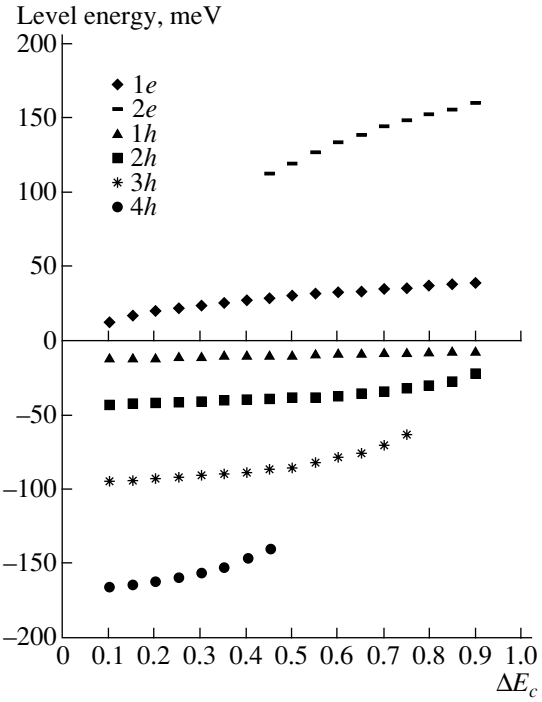

Fig. 4. Dependences of positions of the minibands in a GaAs/GaAsP superlattice on the potential jump in the conduction band. The minibands of the conduction band are plotted in the positive half-plane, while the heavy-hole subbands are plotted in the negative half-plane. 1*e*, 2*e*, 1*h*, 2*h*, 3*h*, and 4*h* denote the energies of minibands for electrons (*e*) and holes (*h*).

Here, m is the free-electron mass; m_e, m_{hh}, and m_{lh} are the effective masses of electrons in the conduction band and of the heavy and light holes in the valence band, respectively; and x is the phosphorus fraction in the ternary compound.

The nonparabolicity of the dispersion relation in the GaAs conduction band was taken into account in calculations by introducing the following energy dependence of the electron effective mass (as suggested in [17]):

$$\frac{m_e(E)}{m_0} = 0.0665 + 0.0436E + 0.0236E^2 - 0.147E^3. \quad (17)$$

Here, $m_e(E)$ is the effective mass of charge carriers in the conduction band and E is the energy expressed in electronvolts. We introduced relation (17) into expressions (12), (13), and (16) when calculating the energy levels in the quantum well of the conduction band.

In order to determine the miniband edges using relation (15), we compiled a program in the MathCad software package for mathematical simulation. It was found that the width of minibands is no larger than 5 meV for the studied sample, with well and barrier widths of 7 nm; this miniband width gives rise to well-defined features in the photoreflection spectrum (Fig. 2).

The energies of the interband transitions $E_{i,j}^{c-vh}$ and $E_{i,j}^{c-vl}$ in the strained SL are defined by the following expressions:

$$E_{i,j}^{c-vh} = E_g^{\mathrm{str}}(c-vh) + E_i^c + E_j^{vh}, \quad (18)$$

$$E_{i,j}^{c-vl} = E_g^{\mathrm{str}}(c-vl) + E_i^c + E_j^{vl}. \quad (19)$$

Here, E_i^c is the position of the ith miniband in the conduction band, E_j^{vh} is the position of the jth miniband of heavy holes in the valence band, and E_j^{vl} is the position the jth miniband of light holes in the valence band.

The positions of minibands in the SL are controlled not only by their geometric parameters but also by the depth of the quantum well for electrons and holes U. Until now, there is no generally accepted method for determining the value of the potential jump at the heteroboundary. On the one hand, the conduction bands in the SL should be spaced from the vacuum level by an energy equal to the electron affinity; this circumstance rigidly fixes the depth of quantum wells for the valence and conduction bands. However, this inference holds only for intrinsic semiconductors at $T = 0$ K. On the other hand, there is the mnemonic common-anion rule. It is well known that the conduction band of III–V compounds is formed by Group-III ions (in the case under consideration, by Ga ions). Therefore, the largest variations in the potential are concerned with the valence band in GaAs/GaAs$_{1-x}$Z$_x$ heterostructures where As ions in the ternary compound are replaced by the ions of an element Z that form the valence band. At the same time, the bands in the heterostructures are arranged with respect to the Fermi level so that the Fermi level is common to all layers. The presence of charge carriers has a significant effect on the position of the Fermi level [18].

In order to determine the potential jump at the heteroboundary in GaAs/GaAs$_{0.6}$P$_{0.4}$, we simulated the energy-band structure of an SL with a different distribution of the potential jump between the subband of heavy holes in the valence band and the conduction band. In the course of simulation with a step of 5%, from 10 to 90% of the energy difference of fundamental transitions in GaAs and GaAs$_{0.6}$P$_{0.4}$ fell within the potential jump in the conduction band; the opposite was true for the valence band.

As a result, we constructed a diagram (Fig. 4) in which the fraction of the band offsets that falls within the conduction band is plotted along the horizontal axis and the energy of minibands in the valence band is plotted on the vertical axis in the negative region, while that in the conduction is plotted on the vertical axis in its positive region. Thus, in order to determine the energy of the band-to-band transition, we should find the energy gap between the minibands in the valence band and those in the conduction band for a specific band offset at the heteroboundary and then add the strain-

induced band gap of GaAs (9) to the value obtained. The best agreement between experimental and theoretical data is attained if 15% of the difference between the energies of fundamental transitions in the well and barrier falls within the conduction band. In the case under consideration, the depth of the well for the conduction band is 39 meV; this depth is 222 and 41 meV for the subbands of the heavy and light holes in the valence band, respectively. It follows from the above that the SL studied is a type-I SL [6] with weakly localized electrons and light holes.

Taking into account the determined potential jump, we suggest the following identification of the lines observed in the photoreflection spectrum: the line at 1.551 eV is attributed to the 1*e*–1*h* transition; the line at 1.587 eV, to the 1*e*–2*h* transition; and the line at 1.699 eV, to the 1*e*–4*h* transition. It is important that the difference between the theoretical and experimental data does not exceed the error in the determination of the positions of spectral lines. The top of the single miniband in the subband of heavy holes is 16 meV away from the top of the valence band, and the energy of the single possible band-to-band transition 1*e*–1*l* is 1.636 eV (which is indicated by an asterisk in Fig. 2).

4. CONCLUSION

Photoreflection spectroscopy is used to study the energies of band-to-band transitions in a superlattice (SL) based on the GaAs/$GaAs_{0.6}P_{0.4}$ heterostructure at room temperature.

In order to determine the magnitude of the potential jump at the heteroboundary, we simulated the structure of the SL minibands using the Kronig–Penney model for periodic potential and taking into account the strain-induced changes in the energy-band structure of the GaAs well and $GaAs_{0.6}P_{0.4}$ barrier. We find that the best agreement between experimental and theoretical data is attained if 15% of the difference in the energies of fundamental transitions in $GaAs_{0.6}P_{0.4}$ and GaAs is concerned with the conduction band ($\Delta E_c/\Delta E_g = 0.15$); this conclusion is consistent with the common-anion rule. We identified the lines observed in the photoreflection spectrum taking into account the determined potential jump at the heteroboundary in the conduction band. It is shown that the lines correspond to band-to-band transitions involving minibands in the superlattice.

REFERENCES

1. G. C. Osbourn, IEEE J. Quantum Electron. **22**, 1677 (1986).
2. E. P. O'Reilly, Semicond. Sci. Technol. **4**, 137 (1989).
3. C. Mailhiot and D. L. Smith, Phys. Rev. B **35**, 1242 (1987).
4. F. Agahi, A. Baliga, K. M. Lau, and N. G. Anderson, Appl. Phys. Lett. **68**, 3778 (1996).
5. F. Agahi, K. M. Lau, E. S. Koteles, *et al.*, IEEE J. Quantum Electron. **30**, 459 (1994).
6. C. Weisbuch and B. Winter, *Quantum Semiconductor Structures: Fundamental and Applications* (Academic, San Diego, 1991).
7. X. Zhang, K. Onabe, Y. Nitta, *et al.*, Jpn. J. Appl. Phys. **30**, L1631 (1991).
8. N. G. Anderson, F. Agahi, A. Baliga, and K. M. Lau, J. Electron. Mater. **24**, 713 (1995).
9. O. S. Gorya, A. S. Keyanu, I. V. Kravetskiĭ, *et al.*, Zh. Prikl. Spektrosk. **62**, 160 (1995).
10. D. E. Aspnes, Surf. Sci. **37**, 418 (1973).
11. P. J. Hughes, B. L. Weiss, and T. J. S. Hosea, Semicond. Sci. Technol. **10**, 1339 (1995).
12. Yu. Kavalyauskas, G. Krivaĭte, L. V. Sharonova, *et al.*, Fiz. Tekh. Poluprovodn. (St. Petersburg) **27**, 1086 (1993) [Semiconductors **27**, 598 (1993)].
13. L. Malikova, F. H. Pollak, O. Gorea, and A. Korotkov, J. Electron. Mater. **29**, 1346 (2000).
14. E. L. Ivchenko and G. Pikus, *Superlattices and Other Heterostructures. Symmetry and Optical Phenomena* (Springer, Berlin, 1995), Series Solid State Science, Vol. 110.
15. S.-G. Shen and X.-Q. Fan, J. Phys.: Condens. Matter **8**, 4369 (1996).
16. A. P. Silin, Usp. Fiz. Nauk **147**, 485 (1985) [Sov. Phys. Usp. **28**, 972 (1985)].
17. H. Kawai, J. Kaneko, and N. J. Watanabe, J. Appl. Phys. **58**, 1263 (1985).
18. V. L. Bonch-Bruevich and S. G. Kalashnikov, *Physics of Semiconductors* (Nauka, Moscow, 1990) [in Russian].

Translated by A. Spitsyn

Semiconductors, Vol. 38, No. 12, 2004, pp. 1390–1393. Translated from Fizika i Tekhnika Poluprovodnikov, Vol. 38, No. 12, 2004, pp. 1435–1438.

SEMICONDUCTOR STRUCTURES, INTERFACES, AND SURFACES

Influence of Ultrashort Pulses of Electromagnetic Radiation on Parameters of Metal–Insulator–Semiconductor Structures

V. A. Terekhov^, A. N. Man'ko, E. N. Bormontov, V. N. Levchenko, S. Yu. Trebunskikh, E. A. Tutov, and É. P. Domashevskaya

Voronezh State University, Universitetskaya pl. 1, Voronezh, 394693 Russia

^e-mail: root@flt.vsu.ru

Submitted April 6, 2004; accepted for publication May 11, 2004

Abstract—The effect of pulsed electromagnetic radiation with a leading-edge duration of 1.4×10^{-9} s and a total pulse duration of $\sim 11.5 \times 10^{-9}$ s, a repetition rate of 10 kHz, and various pulse energies ($\lesssim 2.4 \times 10^{-4}$ J) on $Al/SiO_2/Si$ structures is studied. Capacitance–voltage characteristics of such structures were measured before, during, and after exposure to ultrashort pulses. Changes dependent on the pulse energy caused by insulator polarization and a transformation of the nonequilibrium defect structure of the interface with the semiconductor as a result of the irradiation were found, as well as irreversible changes associated with a breakdown observed after the radiation was switched off. © *2004 MAIK "Nauka/Interperiodica".*

1. INTRODUCTION

Current progress in devices for generating electromagnetic radiation (EMR) makes it possible to produce video pulses with a high peak power with nanosecond and picosecond duration [1–3], comparable to the characteristic response times of insulator, semiconductor, and metal materials that compose the material basis of modern radio-electronic devices.

The fundamental processes of nonsteady nonlinear energy conversion of high-power ultrashort pulses (USPs) of electromagnetic radiation to the response energy of semiconducting and insulating materials radically and conceptually differ from their well-studied interaction with harmonic or pulsed EMR of long duration, in which case transient processes are insignificant.

Difficulties in constructing mathematical tools to adequately describe the interaction between USPs and various materials and structures result in the fact that experimental studies are the main priority at the current stage of development of research in this field.

In the vast majority of modern devices of semiconductor microelectronics, an active functioning region is a very thin semiconductor layer, surface region, or interface of two media. Metal–insulator–semiconductor (MIS) structures are convenient test objects for the control of technological processes and can also be used to identify mechanisms of electronic processes in semiconductor and insulator surface layers subject to various external effects [4].

Many studies of the effect of ultrahigh-frequency (microwave) radiation (both continuous and pulsed of various durations) on materials and device structures have been carried out [5–11]. It was shown that changes in the parameters of the objects under study subjected to an impact exposure to EMR can be both transient, i.e., observed during exposure or immediately after its termination, and steady, observed for a long time after termination of exposure. The following results of the studies of the effect of microwaves on MIS structures were obtained [5–11].

(i) The strongest effects are characteristic of impact fields with the largest gradients.

(ii) Degradation, polarization, and ionization effects in impact fields manifest themselves at significantly lower energies than in steady fields.

(iii) Inhomogeneous semiconductor structures with internal electric fields and interfaces incorporating insulator and metal regions are the least stable to irradiation.

The prime objective of this study was to detect the changes in capacitance–voltage (C–V) characteristics of test $Al/SiO_2/Si$ MIS structures caused by exposure to USPs of EMR.

2. EXPERIMENTAL

Structures grown on KÉF-4.5 crystalline ⟨100⟩ silicon (n-Si:P, $\rho = 4.5\ \Omega$ cm) with a thermal oxide 125 nm thick and control aluminum electrodes (gates) 0.8 mm in diameter deposited by vacuum condensation were used as test structures. High-frequency C–V characteristics were measured at a frequency of 1 MHz and a test signal amplitude of 25 mV using an E7-12 meter. A bias applied to the structure was controlled in the range from –15 to +15 V using a GPC-3030DQ power supply. Since USPs of EMR can significantly affect the operation of the measuring device, the test structures were placed into a matched broadband coaxial load, which decreased the signal at peripheral devices to 60 dB. The internal volume of the coaxial load was filled with a

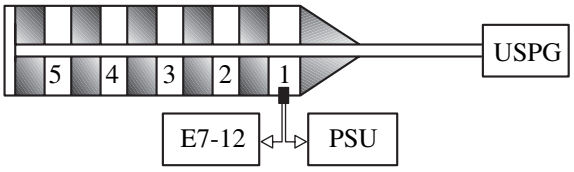

Fig. 1. Schematic diagram of the setup for measuring the *C–V* characteristics of MIS structures in the field of the USP generator (USPG); PSU is the power supply unit.

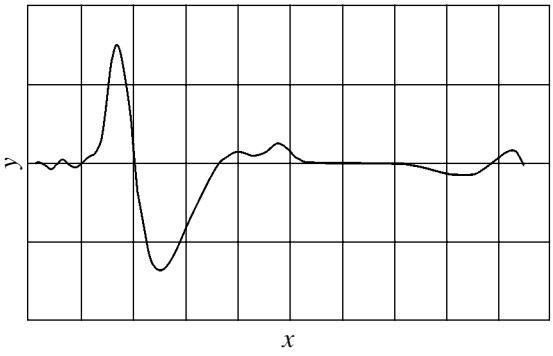

Fig. 2. Oscilloscope trace of the USPG bipolar pulse with an energy of 2.4×10^{-4} J. The *x* and *y* axis scales are 5 ns and 1 V per division, respectively; the attenuation factor is 800.

special adsorber, which allowed us, in combination with positional windows arranged along the load, to place an object into fields with various energies. Figure 1 shows the schematic diagram for measuring the *C–V* characteristics of MIS structures in the field of USPs with various amplitudes and energies, depending on window index 1–5. In these experiments, we used a USP generator (see Fig. 2) that produced bipolar pulses with leading and trailing edge durations of 1.4×10^{-9} and 3.2×10^{-9} s, respectively; a polarity switching time of 2.8×10^{-9} s; and a repetition rate of 10 kHz. The pulse energy at the generator output was 2.4×10^{-4} J. In the first window of the matched coaxial load, the pulse energy was 2.5×10^{-5} J.

3. RESULTS AND DISCUSSION

Measurements of the *C–V* characteristics of MIS structures makes it possible to assess the quality of the insulating layer and its interface with the semiconductor, including the value and sign of the effective charge, the surface-state density, and the existence of leakage currents [12], i.e., the parameters controlling the operation of field-effect transistors and integrated circuits based on them.

Figure 3 shows the typical *C–V* characteristics of MIS structures, measured before and during exposure to EMR USPs with energy $E = 1.3 \times 10^{-5}$ J. Figure 4 shows the *C–V* characteristics of the identical test MIS structure, measured at various energies of EMR USPs. As can be seen in Figs. 3 and 4, the structure capacitance increases during exposure to USPs over the entire measurement range; however, this increase depends on the sign and magnitude of the applied bias. An almost parallel increase in the capacitance is observed in the region enriched with majority carriers (positive bias), in which case the MIS structure capacitance is equal to the insulator capacitance. An increase in the capacitance with the *C–V* characteristic slope is observed in the regions of small and negative biases. In this case, the largest relative change in the capacitance is observed at a bias of 1.5–2 V. An increase in the USP energy results in a nonparallel increase in the capacitance of the structure over the entire bias range (Fig. 4). After exposure to USPs of such energies, the *C–V* characteristic of the MIS structure under study almost coincides with the initial characteristic (Fig. 4).

To analyze the effect of EMR USPs on MIS structures, some electrical parameters were calculated using conventional processing of *C–V* characteristics [12, 13].

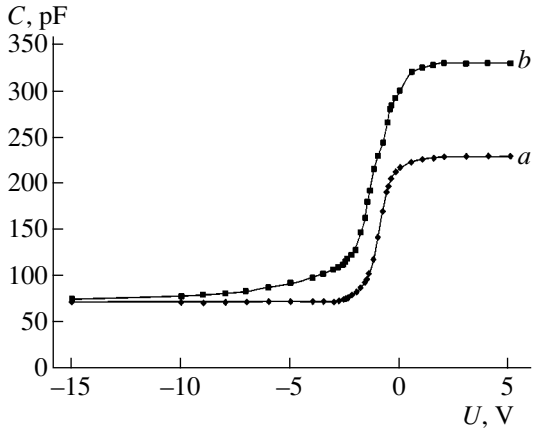

Fig. 3. Capacitance–voltage characteristics of the MIS structure (*a*) before and (*b*) during exposure to USP with energy $E = 1.3 \times 10^{-5}$ J.

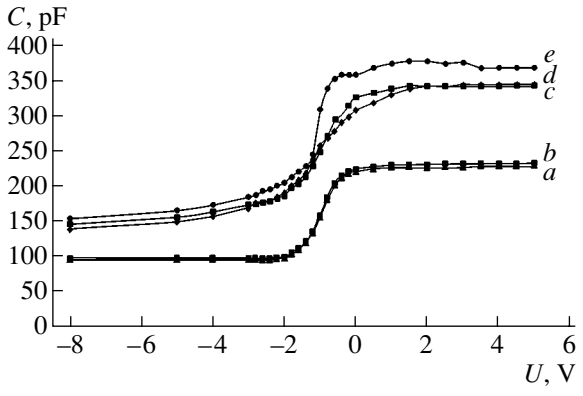

Fig. 4. Capacitance–voltage characteristics of the MIS structures (*a*) before, (*b*) after, and (*c–e*) during exposure to USP with energies of (*c*) 1.2×10^{-5}, (*d*) 1.3×10^{-5}, and (*e*) 2.5×10^{-5} J.

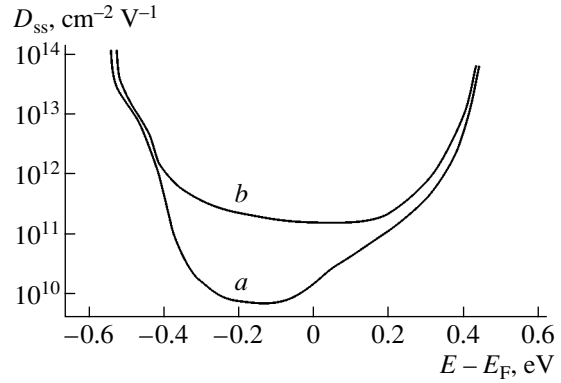

Fig. 5. Spectral surface-state density D_{ss} of the MIS structure at the Si–SiO_2 interface (*a*) under irradiation and (*b*) without irradiation; E_F is the Fermi level.

For the initial structure before its exposure to USPs, the following parameters were determined:

(i) donor impurity concentration $N_D = 10^{15}$ cm^{-3};

(ii) gate insulator thickness $d_{ox} = 125$ nm;

(iii) flat-band voltage $V_{FB} = -0.7$ V;

(iv) effective surface charge $Q_{ss}^* = 1.5 \times 10^{-8}$ C/cm^2; and

(v) effective surface-state density $N_{ss}^* \approx 10^{11}$ cm^{-3}.

During exposure to USPs with $E = 1.3 \times 10^{-5}$ J (Fig. 3), the same structure has the parameters:

$V_{FB} = 1$ V;

$Q_{ss}^* = 3.5 \times 10^{-8}$ C/cm^2; and

$N_{ss}^* \approx 2.2 \times 10^{11}$ cm^{-3}.

In this case, the charge of surface states is positive, since the *C–V* characteristic shifts to negative voltages.

Figure 5 shows the change in the spectral density (D_{ss}) of surface states at the Si–SiO_2 interface. It follows from Fig. 5 that the energy density of surface states increases approximately tenfold under irradiation.

We stress that this interpretation of the change in the *C–V* characteristics under exposure to EMR USPs follows from the conventional method for processing *C–V* characteristics and is only one possible interpretation. The changes observed can also be explained within the model of random fluctuations of the surface electrostatic potential ψ_s of the semiconductor [14, 15]. An increase in the amplitude of fluctuations and their variance under exposure to USPs seems quite reasonable and conforms well to the experimentally observed extension of the *C*(*V*) curve along the voltage axis.

The most unclear phenomenon is the significant increase (~40%) in the highest capacitance of the structure, observed under exposure to USPs with energy $E = 1.3 \times 10^{-5}$ J under conditions of enrichment with majority carriers, since, in this case, the total structure capacitance is specified only by the geometric capacitance of the insulating layer,

$$C_{ox} = \frac{\varepsilon_0 \varepsilon_{ox}}{d_{ox}}.$$

The observed change in C_{ox} corresponds to an increase in the SiO_2 relative permittivity from 3.9 to ~5.6. This increase is presumably caused by the rather strong polarization of silicon and oxygen atoms under exposure to USPs of a fairly large amplitude, which increases ε_{ox}. As the USP energy and amplitude decrease, the C_{ox} increase becomes noticeably smaller (Fig. 4). At a pulse energy of 1.3×10^{-6} J, the additive component to C_{ox} amounts to 5–7%. The rather heavy dependence of the change in the insulator capacitance of the MIS structure on the UPS amplitude may suggest that the polarization factor significantly contributes to this change.

As the UPS amplitude and energy increase to $E = 2.5 \times 10^{-5}$ J, the effects of through insulator breakdown become observable, which manifests itself in the C_{ox} falloff with increasing bias to the MIS structure. As the USP energy increases approximately tenfold to $\sim 2.4 \times 10^{-4}$ J, irreversible changes in the *C–V* characteristics of the MIS structures can be observed. We carried out these experiments in a stripe load without adsorber [16]. Figure 6a shows the *C–V* characteristics of the MIS structures, in which leakage currents of both majority and minority carriers manifest themselves after exposure to high-energy EMR USPs for 10 min. Figure 6b illustrates the rare case of degradation of the MIS structure under exposure to USPs with the same energy of $\sim 2.4 \times 10^{-4}$ J. Here, irradiation for 2 min in addition to the initiation of leakage currents of minority carriers results in the rather distinct peak in the experimental *C–V* characteristic of the MIS structure. This peak indicates that a local level of fast surface states (which have time to respond at the frequency of capacitance measurements, 1 MHz) is formed at the Si–SiO_2 interface under exposure to USPs. After calculating a theoretical *C–V* characteristic of a corresponding ideal MIS structure and calibrating it over the surface potential ψ_s, we estimated the position of this level [12, 13] as ~0.3 eV above the top of the valence band. The concentration of local centers at this level immediately after exposure to EMR USPs was 3×10^{11} cm^{-3}. After the termination of irradiation, the observed capacitance peak decreases for about an hour, after which the *C–V* characteristic in this voltage range becomes identical to that shown in Fig. 6a.

Thus, the insulator capacitance in MIS structures increases under exposure to EMR USPs. This increase depends on the USP energy, and when the energy is sufficiently high ($>2.5 \times 10^{-5}$ J), a through insulator breakdown is possible. Moreover, a significant increase in the surface-state density is observed, and the conductivity conversion point shifts in the boundary region.

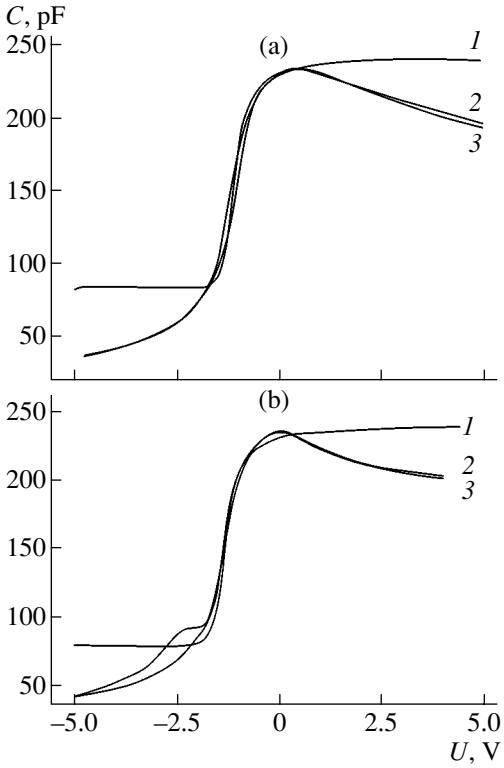

Fig. 6. Capacitance–voltage characteristics of MIS structures before and after exposure to EMR USPs with an energy of 2.4×10^{-4} J. (a): (*1*) before irradiation, (*2*) immediately after 10-min irradiation, and (*3*) one day after irradiation. (b): (*1*, *3*) the same as in (a) and (*2*) immediately after 2-min irradiation (manifestation of the local level of fast surface states at the Si–SiO_2 interface immediately after exposure to USPs).

4. CONCLUSIONS

The study of changes in the *C–V* characteristics of MIS structures exposed to ultrashort pulses (USPs) of electromagnetic radiation shows that

(i) the increase in the insulator capacitance in MIS structures depends on the USP energy;

(ii) under exposure to USPs with an energy of $\sim 10^{-5}$ J, the energy surface-state density at the semiconductor–insulator interface increases tenfold; and

(iii) as the USP energy increases to 10^{-4} J, a through insulator breakdown in MIS structures is possible.

REFERENCES

1. S. N. Rukin, Prib. Tekh. Éksp., No. 4, 5 (1999) [Instrum. Exp. Tech. **42**, 439 (1999)].
2. A. S. Karaush and R. V. Potemkin, Élektron. Prom-st., No. 1, 93 (1998).
3. V. G. Shpak, M. I. Yalandin, N. S. Ginzburg, *et al.*, Dokl. Akad. Nauk **365**, 50 (1999) [Dokl. Phys. **44**, 143 (1999)].
4. *Properties of Metal–Insulator–Semiconductor Structures*, Ed. by A. V. Rzhanov (Nauka, Moscow, 1976) [in Russian].
5. B. A. Stryukov and S. I. Lenchuk, Radiotekh. Élektron. (Moscow) **45**, 887 (2000) [J. Commun. Technol. Electron. **45**, 808 (2000)].
6. D. A. Usanov, A. V. Skripal', and N. V. Ugryumova, Pis'ma Zh. Tekh. Fiz. **25** (1), 42 (1999) [Tech. Phys. Lett. **25**, 17 (1999)].
7. D. A. Usanov, S. B. Venig, and V. E. Orlov, Pis'ma Zh. Tekh. Fiz. **25** (2), 39 (1999) [Tech. Phys. Lett. **25**, 58 (1999)].
8. D. A. Usanov, A. V. Skripal', N. V. Ugryumova, *et al.*, Fiz. Tekh. Poluprovodn. (St. Petersburg) **34**, 567 (2000) [Semiconductors **34**, 550 (2000)].
9. D. A. Usanov, A. V. Skripal', and N. V. Ugryumova, Fiz. Tekh. Poluprovodn. (St. Petersburg) **32**, 1399 (1998) [Semiconductors **32**, 1248 (1998)].
10. A. A. Belyaev, A. E. Belyaev, A. A. Ermolovich, *et al.*, Zh. Tekh. Fiz. **68** (12), 49 (1998) [Tech. Phys. **43**, 1445 (1998)].
11. V. V. Antipin, V. A. Godovitsyn, D. V. Gromov, *et al.*, Zarubezh. Élektron. Tekh., No. 1, 37 (1995).
12. S. Sze, *Physics of Semiconductor Devices*, 2nd ed. (Wiley, New York, 1981; Mir, Moscow, 1984), Vol. 1.
13. E. N. Bormontov, *Physics and Metrology of MIS Structures* (Voronezh. Gos. Univ., Voronezh, 1997) [in Russian].
14. E. H. Nicollian and A. Goetzberger, Bell Syst. Tech. J. **46**, 1055 (1967).
15. E. N. Bormontov and S. V. Lukin, in *Proceedings of 5th Conf. on Simulation of Devices Technologies* (Obninsk, Russia, 1996), p. 35.
16. V. A. Terekhov, E. A. Tutov, A. N. Man'ko, and É. P. Domashevskaya, Kondens. Sredy Mezhfaz. Granitsy **3** (1), 86 (2001).

Translated by A. Kazantsev

Semiconductors, Vol. 38, No. 12, 2004, pp. 1394–1399. Translated from Fizika i Tekhnika Poluprovodnikov, Vol. 38, No. 12, 2004, pp. 1439–1444.

SEMICONDUCTOR STRUCTURES, INTERFACES, AND SURFACES

Traps with Near-Midgap Energies at the Bonded Si/SiO_2 Interface in Silicon-on-Insulator Structures

I. V. Antonova*^, V. P. Popov*, V. I. Polyakov, and A. I. Rukovishnikov****

**Institute of Semiconductor Physics, Siberian Division, Russian Academy of Sciences, pr. Akademika Lavrent'eva 13, Novosibirsk, 630090 Russia*

^e-mail: antonova@isp.nsc.ru

***Institute of Radio Engineering and Electronics, Russian Academy of Sciences, Mokhovaya ul. 11, Moscow, 103907 Russia*

Submitted April 26, 2004; accepted for publication May 11, 2004

Abstract—Capture centers (traps) are studied in silicon-on-insulator (SOI) structures obtained by bonding and hydrogen-induced stratification. These centers are located at the Si/SiO_2 interface and in the bulk of the split-off Si layer. The parameters of the centers were determined using charge deep-level transient spectroscopy (Q-DLTS) with scanning over the rate window at fixed temperatures. Such a method allows one to study the traps near the Si midgap at temperatures near 295 K. It is shown that the density of traps with a continuous energy spectrum, which are located at the bonded Si/SiO_2 interface, decreases by more than four orders of magnitude at the midgap compared with the peak density observed at the activation energy $E_a \approx 0.2$–0.3 eV. The capture centers are also found in the split-off Si layer of the fabricated SOI structures. Their activation energy at room temperature is $E_a = 0.53$ eV, the capture cross section is 10^{-19} cm^2, and the concentration is $(0.7–1.7) \times 10^{13}$ cm^{-3}. It is assumed that these capture centers are related to deep bulk levels induced by electrically active impurities (defects) in the split-off Si layer close to the Si/SiO_2 interface. © *2004 MAIK "Nauka/Interperiodica".*

1. INTRODUCTION

In addition to epitaxy, the main procedure that is currently used for fabrication of various multilayer structures is material bonding technology [1]. Bonding is currently the simplest and cheapest method for fabricating various heterostructures based on different materials including submicrometer Si layers in silicon-on-insulator (SOI) structures. This method is especially attractive from the standpoint of applications. If the SOI structures are fabricated using bonding technology, the bonded Si/SiO_2 interface is sometimes located in the immediate proximity of the operational layer of the SOI structures, specifically, between the split-off Si layer and the insulator [2, 3]. The energy spectrum of states was studied for the upper half of the band gap for a bonded Si/SiO_2 interface [4, 5]. It was shown that the trap energies are mainly concentrated in the range $E_a = 0.17$–0.37 eV calculated from the bottom of the conduction band. Moreover, this range narrows as the doping level of the split-off Si level increases [5]. For the classical Si/SiO_2 interface fabricated by thermal oxidation, the density of states (DoS) for the trap energy spectra sometimes has a maximum $D_{it}^{\max}$ in this energy range, especially for Si (111) [6]. Usually, the ratio $D_{it}^{\max}/D_{it}^{mg} \lesssim 3$, where D_{it}^{mg} is the DoS at the Si midgap. In the case of a bonded Si/SiO_2 interface, the carrier capture cross sections of the traps are relatively small ($\sigma = 10^{-18}$–10^{-19} cm^2). Therefore, when using the conventional DLTS procedure with temperature scanning at fixed values of the rate window, it was possible to study capture centers only up to the maximum energy $E_a \approx 0.4$ eV, and no information was obtained for the spectrum of states closer to the Si midgap. In this study, we used the Q-DLTS method with scanning over the rate window [7, 8] and an ASEC-03 measuring system [9]. This allowed us to significantly expand the measured spectral range and to study the traps with activation energies close to the Si midgap in the SOI structures.

2. EXPERIMENTAL

The SOI structures studied had a 0.48-μm-thick split-off *n*-Si layer and a buried 0.4-μm-thick SiO_2 insulator layer. The charge carrier (electron) concentrations in the split-off Si layer and in the *n*-Si substrate were 3×10^{15} and 4×10^{14} cm^{-3}, respectively. To fabricate the measurement mesas with Al contacts on the Si layer and on the substrate, we formed islands of the split-off Si layer lying on the oxide. The Q-DLTS studies were carried out using a multifunctional ASEC-03 measuring system with automated measurement of the rate window in the range from 2×10^{-6} to 10 s. The Q-DLTS spectra $\Delta Q(\tau_m)$, where $\tau_m = (t_2 - t_1)/\ln(t_2/t_1)$ is the rate window and t_1 and t_2 are the times measured from the beginning of the relaxation, were determined in two modes. In mode 1, a bias voltage, which produced the maximum depletion of the split-off Si layer, was applied to the structure. Then the filling voltage

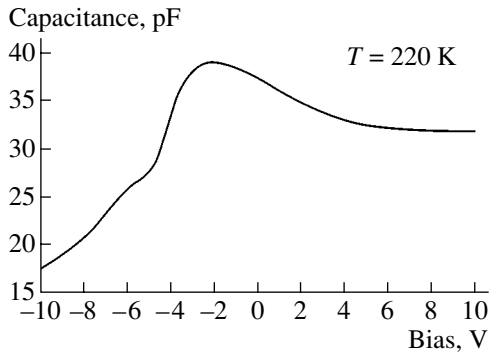

Fig. 1. Capacitance–voltage characteristic of the silicon-on-insulator structure measured at T = 220 K and frequency of the probe signal f = 500 Hz.

pulse was applied, whose amplitude completely removed the space charge. This produced recharging of the largest possible number of traps located in the split-off layer and at the Si/SiO$_2$ interface. In this case, the Q-DLTS spectrum was measured after the end of the pulse during carrier escape from the levels. This is the standard mode of DLTS measurements. In mode 2, the forward bias voltage applied to the structure removed the band bending and the space charge region in the split-off Si layer. Under such a bias, the traps were filled. Then a voltage pulse was applied that depleted the split-off Si layer. The quantity $\Delta Q(\tau_m)$ was measured at the end of the pulse, when the carriers were captured by the traps, rather than during the release of carriers as in mode 1. In describing the results of the measurements, we refer to the voltage pulse used for recharging the traps as the filling pulse, irrespective of its polarity and measurement mode.

3. RESULTS

Figure 1 shows a typical capacitance–voltage (C–V) characteristic at 220 K and at a frequency of the probe signal of 500 kHz. The capacitance for negative bias voltages applied to the split-off Si layer side corresponds to the enrichment of the band-bending region at the SiO$_2$/n-Si interface in the split-off Si layer and to the depletion in the n-Si substrate (a space-charge region is formed in the substrate). For a positive bias at the structure, the substrate is in the accumulation state, whereas the space charge region is formed in the split-off Si layer. This allowed us to use positive voltages from the range of the observed capacitance variation for the study of capture centers in the split-off Si layer and traps at the Si/SiO$_2$ interface.

Figure 2 shows the Q-DLTS spectra measured at 200, 220, and 240 K for measurement modes 1 and 2 for a large filling-pulse amplitude (>5 V). The decrease in the measurement temperature corresponds to the shift of the probed energy region in the Si band gap toward the conduction band. It should be noted that the spectra recorded in modes 1 and 2 significantly differ, although the bias voltages U applied to the structure and filling-pulse amplitudes ΔU are similar,

$$U_1 = U_2 + \Delta U_2, \quad \Delta U_1 = -\Delta U_2, \quad U_2 = U_1 + \Delta U_1;$$

here, indices 1 and 2 denote the measurement mode. Such a choice of voltages allowed us to test the same regions and levels using both measurement modes. The Q-DLTS spectra show the existence of a continuous energy spectrum of electrically active traps. Such a spectrum is characteristic of surface or interface states. Similarly to [4, 5], we attribute this spectrum to recharging of traps at the Si/SiO$_2$ interface. In mode 2 measurement of the Q-DLTS spectra, the A peak is clearly recorded (Fig. 2b). The location of the A peak is

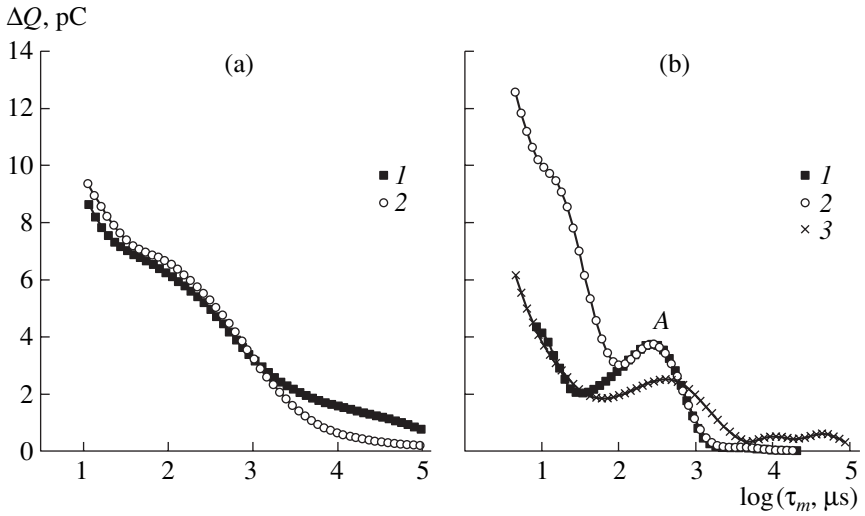

Fig. 2. Q-DLTS spectra measured at temperatures T = (*1*) 240, (*2*) 220, and (*3*) 200 K and the filling-pulse duration $\tau = 10^3$ μs. Measurement modes: (a) 1 and (b) 2. (a): (*1*) U = 10 V, ΔU = –9 V; (*2*) U = 8 V, ΔU = –10 V; (b): (*1*) U = 1 V, ΔU = 9 V; (*2*) U = –2 V, ΔU = 10 V; (*3*) U = 3 V, ΔU = –7 V. U is the constant bias voltage, and ΔU is the filling-pulse amplitude.

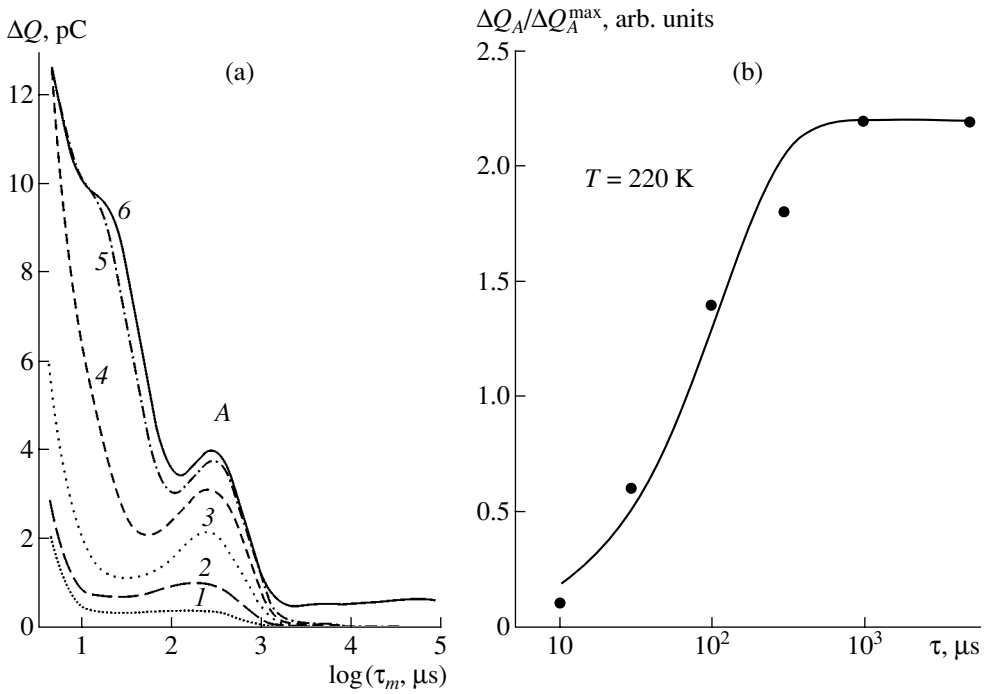

Fig. 3. (a) Q-DLTS spectra for measurement mode 2 at T = 220 K and the filling-pulse duration τ = (*1*) 10, (*2*) 30, (*3*) 10^2, (*4*) 3×10^2, (*5*) 10^3, and (*6*) 5×10^3 μs. (b) The experimental dependence (dots) of the normalized amplitude of the peak A ($\Delta Q_A/\Delta Q_A^{\max}$) as a function of the filling-pulse duration τ and the result of the calculation (solid line) by formula (1) in arbitrary units.

almost independent of the charging-pulse amplitude and continuous illumination of the split-off layer with a photon energy higher than the Si band gap. This observation indicates that this peak is caused by recharging the capture centers localized in the bulk of the split-off Si layer. These centers have a discrete activation energy. For relatively low bias voltages and filling-pulse amplitudes, the Q-DLTS spectra measured in mode 1 became identical to the spectra recorded in mode 2; i.e., the A peak appeared in the spectra. The observed variation in the spectra can be associated with the strong effect of the trap charge at the Si/SiO_2 interface on the filling of the capture centers A (this charge is accumulated at high bias voltages).

The Q-DLTS spectra measured in mode 2 at 220 K for different filling-pulse durations τ are shown in Fig. 3a. The filling-pulse amplitude U was 10 V, and the bias voltage ΔU was –2 V. The bias voltage was not changed during the measurement of the spectra. Figure 3a shows that, at $\tau \geq 5$ ms, the amplitude of the A peak and the spectrum in the regions formed by the recharging of the traps at the Si/SiO_2 interface are saturated. Figure 3b shows the experimental τ dependence of the normalized amplitude of the A peak ($\Delta Q_A/\Delta Q_A^{\max}$) and the result of the calculation (solid line) by formula

$$\frac{\Delta Q_A}{\Delta Q_A^{\max}} = 1 - e^{-e_n \tau}, \qquad (1)$$

where e_n is the emission rate from the level and $\Delta Q_A^{\max}$ is the maximum amplitude of the A peak, which is attained as the filling-pulse duration τ increases. The experimental data agree well with the calculation. The dependences of the amplitude of the A peak on the filling-pulse duration were also measured at 200 and 240 K and used to calculate e_n at these temperatures.

Similar measurements of the Q-DLTS spectra for different filling-pulse durations τ were carried out in mode 1 using relatively low reverse-bias voltages and filling-pulse amplitudes. For this measurement mode, the τ dependence of the normalized amplitude of the A peak is described adequately by the expression

$$\frac{\Delta Q_A}{\Delta Q_A^{\max}} = 1 - e^{-c_n \tau}, \qquad (2)$$

where $c_n = v_T n \sigma_A$ is the capture rate for the level, σ_A is the capture cross section, and v_T and n are the thermal velocity and carrier concentration, respectively. The performed estimations showed that $c_n \approx e_n$. The table gives the determined rates of carrier capture and escape from the level, the capture cross sections, and the activation energies of the centers forming the peak A in the Q-DLTS spectra. The concentration of the capture centers A is $(0.7–1.7) \times 10^{13}$ cm^{-3}.

Similar analysis of the dependence of the recharging of the traps on the filling-pulse duration τ was also carried out for capture centers with a continuous energy

spectrum. These centers are located at the Si/SiO$_2$ interface. Figure 4 shows the experimental τ dependences of $\Delta Q_C/\Delta Q_C^{\max}$, where ΔQ_C is the magnitude of the charge that recharges the traps with a continuous energy spectrum at a fixed value of the rate window τ_m = 20 μs; $\Delta Q_C^{\max}$ is the maximum value of the charge, which is attained as τ increases; and the solid line represents the result of the calculation (similar to the above estimations for the capture centers *A*) by the formula

$$\frac{\Delta Q_C}{\Delta Q_C^{\max}} = 1 - e^{-e_n\tau}. \quad (3)$$

According to this calculation, the rate of emission from the traps is $e_n = 2 \times 10^3$ s^{-1} at 220 K. Figure 4 shows that, for the Q-DLTS spectra measured in mode 1, the τ dependence of $\Delta Q_C/\Delta Q_C^{\max}$ is different from the similar dependence for the centers *A*.

To calculate the energy spectrum of the DoS of the traps D_{it} at the Si/SiO$_2$ interface of the SOI structure, we used the method suggested in [10]. The activation energy of the capture centers that make the main contribution to the DLTS signal at a given temperature *T* and a rate window τ_m was described by the expression $E_a = |E_C - E| = kT\ln(\sigma v_T N_c \tau_m)$, where N_c is the DoS in the conduction band, E_C is the energy of the bottom of the conduction band, and *E* is the energy location of the trap.

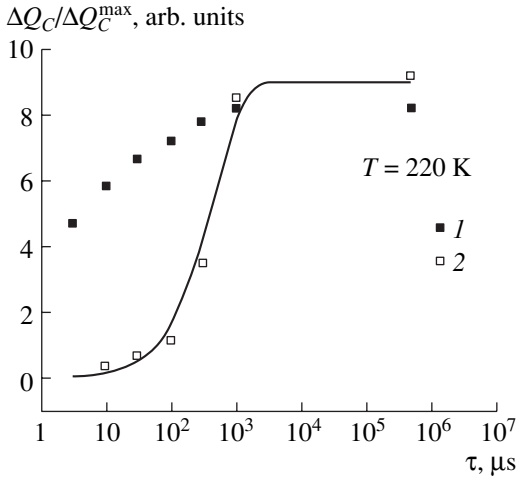

Fig. 4. Experimental dependences of $\Delta Q_C/\Delta Q_C^{\max}$ on the filling-pulse duration τ for measurement modes 1 (points *1* at U = 8 V, ΔU = –10 V) and 2 (points *2* at U = –2 V, ΔU = 10 V); T = 220 K. ΔQ_C is the magnitude of the charge contributing to the recharging of traps with a continuous energy spectrum at a fixed rate window τ_m = 20 μs, and $\Delta Q_C^{\max}$ is the maximum value of the charge attained as τ increases. The solid line represents the result of the calculation by formula (3) (in arbitrary units).

Parameters of capture centers *A*

T, K	e_n, s^{-1}	c_n, s^{-1}	E_A, eV		σ_A, cm^2
			mode 1	mode 2	
240	8×10^3	7×10^3	0.52	0.53	1.1×10^{-19}
220	8×10^3	8×10^3	0.49	0.45	1.1×10^{-19}
200	2.5×10^3	4×10^3	0.43	0.38	3.3×10^{-20}

Note: c_n and e_n are the rates of carrier capture and emission for the centers, E_A is the activation energy, and σ_A is the capture cross section for centers *A*.

Figure 5 shows the trap energy distributions, which were determined from the Q-DLTS spectra recorded in the two measurement modes. For calculations, we used a value of the capture cross section of 10^{-18} cm^2, which was determined in [5]. Processing the Q-DLTS spectra measured in mode 2, we subtracted the peak *A* from the total spectrum when we calculated the trap spectrum at the Si/SiO$_2$ interface.

Figure 6 shows the results of the calculation of the energy spectrum (the trap DoS) for the structure studied; these results were obtained for activation energies up to ~0.4 eV from the temperature-scan DLTS spectra [5] and for higher activation energies from our DLTS spectra recorded by scanning over the rate window. Our method for calculating the spectrum of states was identical to that used in [5]. We can see that the spectra supplement each other well.

We also measured the kinetics of photovoltage $V_{\text{ph}}(t)$ of an SOI structure under high-intensity pulsed illumination using white light (the split-off Si layer was illuminated). The measurements were carried out under

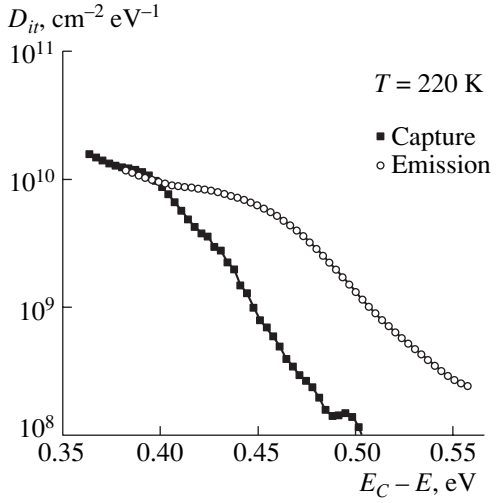

Fig. 5. Energy spectrum of the density of states of the D_{it} traps at the Si/SiO$_2$ interface of the SOI structure. The spectrum is derived from the Q-DLTS spectra measured for carrier emission from the traps (mode 1) and for their charging (mode 2) at T = 220 K. $E_C - E = E_a$ is the activation energy.

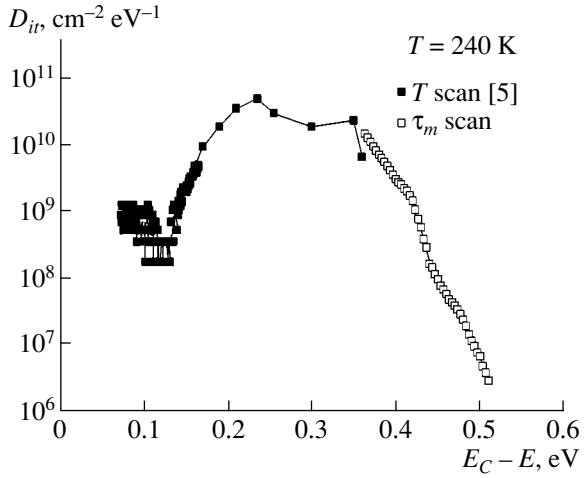

Fig. 6. Combined energy spectrum (trap density of states) at the Si/SiO_2 interface and in the split-off Si layer for the SOI structure from [5] and from our results for the measurement temperature 240 K.

open-circuit conditions and showed the presence of two fast components of different signs. We attributed these components to the separation of nonequilibrium carriers in the band-bending region (in the potential barriers) at the boundary with SiO_2 in the substrate and in the split-off Si layer. The magnitude of these barrier photovoltages increased with temperature at constant illumination intensity. In addition, two slow components with different signs were clearly seen in the measured photoresponse. These components are most probably due to the contribution of surface trapping of excess carriers at the Si/SiO_2 interface to the measured photovoltage signal. For samples without a split-off Si layer, the photoresponse included only two components, specifically, a fast and a slow component with the same sign. By the sign of the slow component, we can conclude that this component is related to the capture of nonequilibrium holes by traps at the Si/SiO_2 interface.

4. DISCUSSION

The analysis of the experimental data showed that the rates of carrier capture and escape for the traps forming the *A* peak (these rates were determined from the dependences of the Q-DLTS spectra on the filling pulse duration) are almost the same. However, in the case of measurement of the Q-DLTS spectra in mode 1 at large values of the constant bias voltages and filling-pulse amplitudes, the filling of the *A* centers with carriers significantly decreased. At the same time, the largest number of traps with continuous energy spectrum, which are located at the Si/SiO_2 interface, were recharged under these conditions. This allows us to assume that the capture centers *A* are located at the interface, and the charge at the traps of the Si/SiO_2 interface affects the number of carriers captured at the *A* centers.

The second specific feature of the *A* centers is the dependence of the energy level on temperature and measurement mode (see table). Note also that in each case the *A* peak in the DLTS spectra virtually corresponds to the centers with fixed values of the activation energy and the capture cross section. The most probable explanation of the variation in the activation energy as a function of temperature and measurement mode relies on the assumption that the measured energy is determined by the effective height of the potential barriers for carrier capture and emission. If an accumulation voltage pulse is applied, the majority carriers (electrons) captured by the centers overcome the barrier when these carriers are in the conduction band. In contrast, the emission proceeds from the level in the band gap, and the effective height of the potential barrier for carriers is larger for their emission. This reasoning can explain the high activation energy determined during the measurement of the Q-DLTS spectra in mode 1. However, the effective height of the potential barrier is specified by the temperature-dependent parameters of traps at the Si/SiO_2 interface, by their occupancy (the position of the Fermi level at the Si/SiO_2 interface), and by the characteristics of the localized charge in the oxide. As a result, the effective height of the potential barrier for carriers increases with temperature both for their capture and emission (see table).

It follows from Figs. 4 and 5 that the use of large amplitudes of the reverse bias, which induces the space charge region in the split-off Si layer, leads to a considerable increase in the charge at the traps of the Si/SiO_2 interface. A possible reason for this effect is the charging of slow states at the interface during the reverse bias. This charging gives rise to depletion for majority carriers (electrons) in the boundary region and the accumulation mode for holes. In this case, the positive charge must be trapped, which naturally changes the kinetics of trap filling with electrons. This conclusion is also confirmed by the results of the study of the photovoltage kinetics under intense pulsed illumination. The photoresponse caused by the generation of nonequilibrium carriers in the split-off Si layer can be clearly separated into two components. These are the barrier photovoltage and photovoltage of surface trapping that is associated with the capture of excess holes by the traps at the Si/SiO_2 interface.

Figure 6 shows that the DoS for traps with energies close to the midgap significantly decreases compared with the DoS at the peak of the distribution at energies of 0.25–0.35 eV. The ratio of DoS at the peak and at the Si midgap for the fabricated SOI structures was found to be $D_{it}^{\max}/D_{it}^{mg} \approx 3 \times 10^4$, which indicates a substantial qualitative and quantitative difference between the energy distribution of the traps at the bonded Si/SiO_2 interface and that at the interface formed by thermal oxidation of silicon.

5. CONCLUSIONS

We studied the capture centers at the boundary and in the bulk of the split-off Si layer in silicon-on-insulator (SOI) structures. The measurements performed showed that the trap density at the Si midgap of the fabricated SOI structures is more than four orders of magnitude lower compared with the trap density at the peak of the distribution ($E_a \approx 0.25$–0.35 eV). This finding indicates that the energy structure of the traps at the bonded Si/SiO_2 interface differs radically from that for the interface produced by thermal oxidation of silicon. In the split-off Si layer, we also found and studied capture centers with an activation energy of 0.53 eV at room temperature, a capture cross section of 10^{-19} cm^2, and a concentration of $(0.7–1.7) \times 10^{13}$ cm^{-3}. These deep centers are electrically active point defects or impurities localized at the bonding interface of SOI structures.

ACKNOWLEDGMENTS

This study was supported in part by the International Scientific Research Center, project no. 2503.

We thank M.S. Kagan and L.L. Golik for helpful discussions.

REFERENCES

1. *Abstracts of VII International Symposium on Semiconductor Wafer Bonding Science, Technology and Applications, 2003*, Ed. by S. Bengtsson and C. E. Hant (Electrochemical Society, Pennington, N.J., 2004).
2. V. P. Popov, I. V. Antonova, V. F. Stas', and L. V. Mironova, RF Patent No. 2 164 719 (1999).
3. Y. Cho and N. W. Cheung, Appl. Phys. Lett. **83**, 3827 (2003).
4. I. V. Antonova, O. V. Naumova, J. Stano, *et al.*, Appl. Phys. Lett. **79**, 4539 (2001).
5. I. V. Antonova, J. Stano, D. V. Nikolaev, *et al.*, Fiz. Tekh. Poluprovodn. (St. Petersburg) **35**, 948 (2001) [Semiconductors **35**, 912 (2001)].
6. N. M. Johnson, D. K. Biegeslsen, M. D. Moyer, and S. T. Chang, Appl. Phys. Lett. **43**, 563 (1983).
7. V. I. Polyakov, P. I. Petrov, O. N. Ermakova, *et al.*, Fiz. Tekh. Poluprovodn. (Leningrad) **23**, 125 (1989) [Sov. Phys. Semicond. **23**, 76 (1989)].
8. V. I. Polyakov, N. M. Rossukanyi, A. I. Rukovishnikov, *et al.*, J. Appl. Phys. **84**, 2882 (1998); V. I. Polyakov, A. I. Rukovishnikov, N. M. Rossukanyi, and B. Druz, in *MRS Book Electrically Based Microstructural Characterization* (2000), Vol. 699, p. 219.
9. K. Hofmann and M. Schulz, J. Electrochem. Soc. **132**, 2201 (1985).
10. D. Vuillaume and J. C. Bourgoin, Surf. Sci. **162**, 680 (1985).

Translated by N. Korovin

Semiconductors, Vol. 38, No. 12, 2004, pp. 1400–1401. Translated from Fizika i Tekhnika Poluprovodnikov, Vol. 38, No. 12, 2004, pp. 1445–1446.

SEMICONDUCTOR STRUCTURES, INTERFACES, AND SURFACES

Kinetics of the Growth of an Amorphous Layer at the Surface of Silicon Bombarded with Fast Heavy Ions at Low Temperatures

A. Yu. Azarov

St. Petersburg State Polytechnical University, Politekhnicheskaya ul. 29, St. Petersburg, 195251 Russia

e-mail: alazar@hotbox.ru

Submitted May 17, 2004; accepted for publication May 24, 2004

Abstract—The accumulation of defects in the surface region of Si bombarded with 0.5-MeV Bi ions at a temperature of –196°C is considered. It is shown that the buildup of disorder in the surface region as the ion dose increases manifests itself in the planar growth of an amorphous layer starting from the Si–SiO_2 interface, and this growth sets in after a threshold implantation dose is attained. The results obtained can be described adequately in the context of a model based on the migration of mobile point defects generated by fast ions to the surface, subsequent processes of segregation of these defects at the interphase boundary, and the presence of saturable sinks in the initial samples. © *2004 MAIK "Nauka/Interperiodica".*

Bombardment with high-energy (~1 MeV) ions makes it possible to modify the properties of a solid to a considerable depth [1, 2]. Ion bombardment inevitably generates radiation defects; therefore, it is necessary to understand the processes of accumulation of these defects in order to optimize the technology. Previously [3], Rutherford backscattering in combination with channeling was used to study defect production during irradiation of Si with 0.5-MeV Bi ions. It was shown that a surface peak of defects is observed at the liquid-nitrogen temperature, in addition to the bulk peak whose origin and growth kinetics were considered in detail previously. Typically, such a surface peak of defects is observed after irradiation of Si with light ions at room temperature [4, 5] and corresponds to a thin and completely amorphized layer [6]. It is worth noting that, due to the small thickness of this layer and the low resolution of Rutherford backscattering/channeling, the surface peak is not rectangular and its height is below the level that corresponds to a completely disordered sample. This circumstance is clearly illustrated in Fig. 1, in which the squares show an example of the depth distribution of the relative defect concentration for the ion dose $\Phi = 1.8 \times 10^{13}$ cm^{-2}; this distribution was calculated on the basis of the experimental spectrum using one of the widely used algorithms [7]. In order to estimate the thickness of the surface amorphous layer, we replaced the depth distribution profile of defects with a model function that was rectangular and had a height corresponding to complete disordering and a width h; the latter was assumed to be equal to the thickness of the surface amorphous layer and was determined by comparing the actual spectrum with the result of convolution of the model function with the instrument-related functions. The instrument (spread) function was taken as a Gaussian function with the rms deviation determined from the slope of the surface edge of the spectrum for the completely amorphized sample. The result of this simulation is shown in Fig. 1 for the case of irradiation with $\Phi = 1.8 \times 10^{13}$ cm^{-2} of ions; the solid line represents the model function, and the dashed line represents the result of convolution of the latter with the spread function. Finally, the thickness related to the presence of the natural SiO_2 surface oxide was subtracted from the value of h obtained as a result of simulation. The $h(\Phi)$ dependence obtained in this way is represented by squares in Fig. 2. It can be seen that the value of h increases with Φ; a rapid increase in h sets in after a certain threshold dose of ions is

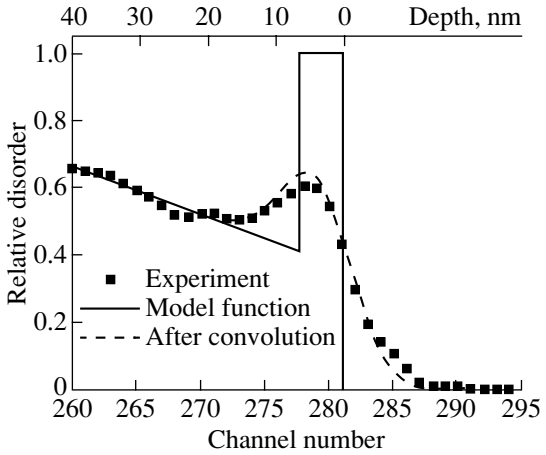

Fig. 1. Dependence of the relative defect concentration in the surface region on depth (channel number) for the case of irradiation of Si (100) at –196°C with Bi ions with an energy of 0.5 MeV and a dose of 1.8×10^{13} cm^{-2}. Squares correspond to experimental data, the solid line represents the model function, and the dashed line represents the result of convolution of the model function with the instrument (spread) function.

1063-7826/04/3812-1400$26.00 © 2004 MAIK "Nauka/Interperiodica"

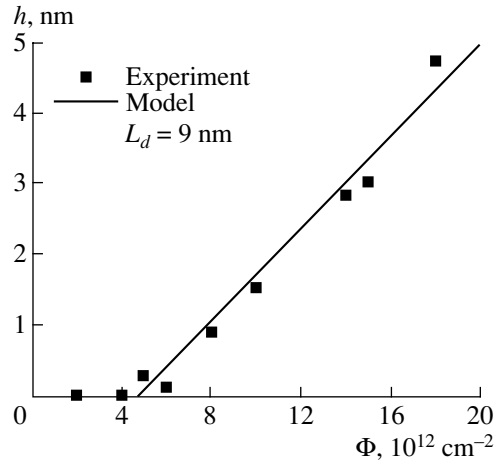

Fig. 2. Dependence of the thickness of the amorphous layer at the surface of Si (100) on the ion dose; the sample was irradiated at –196°C with 0.5–MeV Bi ions. Squares correspond to experimental data and the solid line represents the results of calculations.

attained. Previously, we suggested a model that described the kinetics of the growth of an amorphous layer in the course of irradiation of Si with light low-energy ions at room temperature [8]. It was assumed that the growth of the amorphous layer started from the interphase Si–SiO_2 boundary and then continued owing to the migration of mobile point radiation defects and their segregation at the interface between the amorphous layer and the crystal; it was also assumed that the threshold dose was governed by the concentration of saturable sinks that were initially present in the sample. The result of calculations performed on the basis of the above model for the diffusion length L_d = 9 nm, which is an adjustable parameter in this model, is represented by the solid line in Fig. 2. Note that L_d = 9 nm is close to the values of the diffusion length obtained in [6] for processes that occurred at room temperature. This circumstance may be related to the fact that a decrease in the diffusion coefficient for mobile point defects (it was shown in [9] that a decrease in temperature from 20 to –196°C reduces the diffusion coefficient by at least one and two orders of magnitude for interstitial atoms and vacancies, respectively) is compensated by an increase in the lifetimes of the corresponding defects.

The author thanks A.I. Titov and S.O. Kucheyev for helpful discussions.

REFERENCES

1. J. F. Ziegler, Nucl. Instrum. Methods Phys. Res. B **6**, 270 (1985).
2. J. S. Williams, R. G. Elliman, M. C. Ridgway, *et al.*, Nucl. Instrum. Methods Phys. Res. B **80–81**, 507 (1993).
3. A. I. Titov, S. O. Kucheyev, V. S. Belyakov, and A. Yu. Azarov, J. Appl. Phys. **90**, 3867 (2001).
4. A. I. Titov and G. Carter, Nucl. Instrum. Methods Phys. Res. B **119**, 491 (1996).
5. T. Lohner, M. Fried, N. Q. Khanh, *et al.*, Nucl. Instrum. Methods Phys. Res. B **147**, 90 (1999).
6. J. A. van den Berg, S. Zhang, S. Whelan, *et al.*, Nucl. Instrum. Methods Phys. Res. B **183**, 154 (2001).
7. K. Schmid, Radiat. Eff. **17**, 201 (1973).
8. A. I. Titov, V. S. Belyakov, and A. Yu. Azarov, Nucl. Instrum. Methods Phys. Res. B **212**, 169 (2003).
9. A. Hallén and B. G. Svensson, Radiat. Eff. Defects Solids **128**, 179 (1994).

Translated by A. Spitsyn

Semiconductors, Vol. 38, No. 12, 2004, pp. 1402–1408. Translated from Fizika i Tekhnika Poluprovodnikov, Vol. 38, No. 12, 2004, pp. 1447–1454.

LOW-DIMENSIONAL SYSTEMS

Formation and Optical Properties of $CuInSe_{2x}Te_{2(1-x)}$ Nanoparticles in a Silicate Glass Matrix

I. V. Bodnar'*, N. P. Soloveĭ*, V. S. Gurin^, and A. P. Molochko***

**Belarussian State University of Informatics and Radioelectronics, Minsk, 220072 Belarus*

***Physico-Chemical Research Institute, Belarussian State University, Minsk, 220080 Belarus*

^e-mail: gurin@bsu.by; gurinvs@lycos.com

Submitted April 26, 2004; accepted for publication May 11, 2004

Abstract—Glasses containing nanoparticles of semiconductor $CuInSe_{2x}Te_{2(1-x)}$ compounds ($0 \le x \le 1$) were fabricated by high-temperature melting of the mixtures of the glass-forming components and the corresponding compounds. Particles of average size 15–30 nm, whose characteristics were similar for compounds with different x, were formed. Optical absorption of the glasses near the fundamental absorption edge in the near-infrared and visible regions of the spectrum was studied, as well as the effect of additional heat treatment of glasses on their optical properties. The nature of the observed changes in the spectra with varying compound composition (the [Se]/[Te] ratio) was related to the possible transformations of the crystalline structure of nanoparticles.

1. INTRODUCTION

The formation of a semiconductor nanocrystalline phase in a dielectric matrix and the control of properties of this phase constitute important problems in the technology of preparation of nanostructured materials. The increased interest in such structures is related to the nontrivial size-dependent physical properties that determine the scientific and applied importance of these structures [1–3]. The effect of quantum confinement on the optical properties of semiconductor materials and glasses containing nanoparticles has been studied mainly for binary compounds [4–9]: sulfides and selenides of cadmium, lead, and zinc. Complex semiconductor compounds, in particular, ternary compounds of the I–III–VI_2 class (where usually I = Cu and Ag; III = Al, Ga, and In; and VI are chalcogene atoms), have a wider variety of properties and can also be obtained as nanoparticles in various media [10–14]. Compounds of the I–III–VI_2 class crystallize mainly in a tetragonal lattice of the chalcopyrite type, in contrast to binary compounds, for which such a lattice is practically never encountered. Transition metal atoms (Cu, Ag) also contribute to the electronic structure of the semiconductor and give rise to rather complicated dependences of optical properties on qualitative and quantitative composition, the degree of ordering of atoms in the crystalline lattice, the presence of defects, and the particle size [15, 16].

We have previously shown that it is possible to obtain $CuInS_2$, $CuInSe_2$, and $CuInTe_2$ compounds in the form of small-size particles in glasses [10–12]. The conditions of synthesis, structure, and linear and nonlinear optical properties of nanoparticles of $CuInS_2$ and $CuInS_{2x}Se_{2(1-x)}$ solid solutions for a limited range of [S]/[Se] ratios (x = 0.5–0.7) have been studied. The results of these studies allowed us to establish that $CuInS_2$ nanoparticles in a silicate glass matrix can have a cubic (rather than chalcopyrite) crystal lattice, which is not characteristic of the bulk material. This circumstance may be a consequence of disorder in copper and indium atomic sites in the cation sublattice. The dimensionality effect can facilitate the manifestation of disorder [17], and a mechanically strong glass matrix can effectively stabilize metastable nanophases. This fact leads to observable anomalies in the size dependence of optical properties of the nanoparticles.

Copper–indium tellurides and solid solutions based on them in the form of nanoparticles were studied to a much lesser degree. The compound $CuInTe_2$ has a lower melting point (1060 K) compared to $CuInS_2$ (1330 K) and $CuInSe_2$ (1260 K) [15, 16, 18]; the temperature of phase transition corresponding to the change in the crystal lattice from macroscopic (poly)crystalline chalcopyrite to zinc blende is equal to 940 K, and the band gap is E_g = 0.8–1.1 eV [16, 19, 20]. At the same time, the quantum confinement effect for this material can be more pronounced, since the exciton Bohr radii in tellurides usually exceed those in sulfides and selenides. Nanoparticles of solid solutions of the $CuInTe_2$–$CuInSe_2$ system have also been inadequately studied and are an object of the present study. The aim of this paper is to determine the conditions for the formation of $CuInSe_{2x}Te_{2(1-x)}$ nanoparticles ($0 \le x \le 1$) in a silicate glass matrix and to study their optical properties and structural state.

2. EXPERIMENTAL

Glasses containing $CuInSe_{2x}Te_{2(1-x)}$ nanoparticles were obtained by direct synthesis from the mixtures of oxides that form the glass matrix, with the addition of preliminarily prepared semiconductor compounds. This method has been previously used successfully to prepare glasses containing particles of other compounds of the $CuInS_{2x}Se_{2(1-x)}$ type [11, 21]. As a matrix, we used the glasses of the SiO_2–CaO–Na_2O system, which do not crystallize after repeated heat treatment and are stable to atmospheric effects. Previously, we optimized the composition of the glass matrix, improved its technical parameters, and managed to lower the synthesis temperature by introducing three alkaline components, Na_2O, K_2O, and Li_2O, in the ratio 1 : 1 : 1. To synthesize the glasses containing nanoparticles of semiconductor compounds, we used $CuInSe_2$, $CuInTe_2$, and solid solutions $CuInSe_{2x}Te_{2(1-x)}$ in a ready fine-dispersed form and synthesized them from elements in a one-zone vertical furnace at temperatures 1050–1300 K with subsequent homogenizing annealing for 150–240 h [22]. The crystal structure (of the chalcopyrite type) of the synthesized semiconductors was identified by X-ray analysis. In this study, the content of the semiconductor introduced into the glass matrix was taken to be constant (0.75 wt %), since it has been previously shown [23] that, for this content, glasses with rather high optical density are obtained, and if the content is increased to 1.0 wt % or more, the semiconductor cannot always be completely dissolved in glass without loss of uniformity. To prevent the oxidation of semiconductors in the charge, we introduced an additional 2.0 wt % of activated coal. The glasses containing the chosen semiconductors were obtained under regeneration conditions in an open gas furnace at a temperature of (1620 ± 20) K keeping the glass at the highest temperature for 1 h. After the synthesis, the melts were rapidly cooled and annealed in a muffle furnace at a temperature of 693 K with subsequent slow cooling to room temperature. Additional heat treatment of glasses was performed at temperatures in the range 500–600°C by keeping them in a muffle furnace for 6 h (above 600°C, the glasses begin to be deformed due to softening).

The size of the formed nanoparticles and their location in glass were determined by transmission electron microscopy (TEM) using a UÉMB-100LM electron microscope. We used "carbon replicas with extraction" taken from the surface of freshly etched glass samples, on which the carbon film with a thickness of 10–20 nm was sputtered. Absorption spectra were recorded on polished plane-parallel samples using a UV5270 Beckman and a CARY 17D spectrophotometer.

3. RESULTS AND DISCUSSION

The glasses containing semiconductor particles, immediately after fabrication and melt cooling, possessed a characteristic coloring and remained transparent (a glass matrix without a semiconductor is colorless). The presence of the coloring gives grounds to believe that a crystalline phase responsible for the characteristic absorption of light is formed at this stage. The $CuInSe_2$ and $CuInTe_2$ compounds have melting temperatures exceeding the glass transition temperatures of the matrix (see above); they melt practically without decomposition and can be separated from the melt during cooling as ultradisperse particles uniformly distributed in the bulk. The process of nanoparticle formation is affected by the matrix composition, in particular, by the nature of cations that are included in the structural glass network and polarize the atoms of the elements that form the particles in the glass matrix [24]. The regions enriched with alkali ions are the probable localization sites of nanoparticles in the glass. The composition of the matrices containing three alkali oxides takes into account the effect of these factors and, therefore, creates favorable conditions for the nucleation and growth of the crystalline phase of semiconductor compounds.

Assumptions concerning the nature of the coloring of the glasses under study are confirmed by electron microscopy and optical studies. The TEM data (Fig. 1) unambiguously indicate that, in the bulk of the matrix, particles are formed that differ considerably from the matrix in their transparency to the electron beam. In addition, in the microphotographs of the glasses under study, liquation cavities, where the particles are located, are clearly seen against the background of the matrix profile. The particles have a shape that is almost spherical and are mainly isolated; however, in some cases, there are aggregates and chains. The average size of the particles is in the range of 15–30 nm, and this value depends only slightly on the composition of the solid solution. On the whole, a similar character of particle distribution and localization was also observed in glasses with $CuInS_{2x}Se_{2(1-x)}$ [23] and $CdSe_xTe_{1-x}$ [25] nanoparticles obtained by the same method. Hence, it is the method of semiconductor nanophase formation rather than its chemical nature that is of primary importance for the dimensional and morphological characteristics of particles in glasses of this type.

As a result of additional heat treatment of glasses at temperatures of 550 and 600°C (for 6 h), the particle size somewhat increases, although their concentration remains virtually unchanged (Fig. 1). This fact indicates that no new particles appear after the secondary heat treatment of glasses, and their slight growth when heated is a common phenomenon for nanophases of various kinds.

We can understand these results concerning the state of nanoparticles in the glasses under study if we assume that these nanoparticles are formed during phase decomposition of the supersaturated solution (of the semiconductor in glass) and that the process is of the recondensation type [26]. During rapid cooling

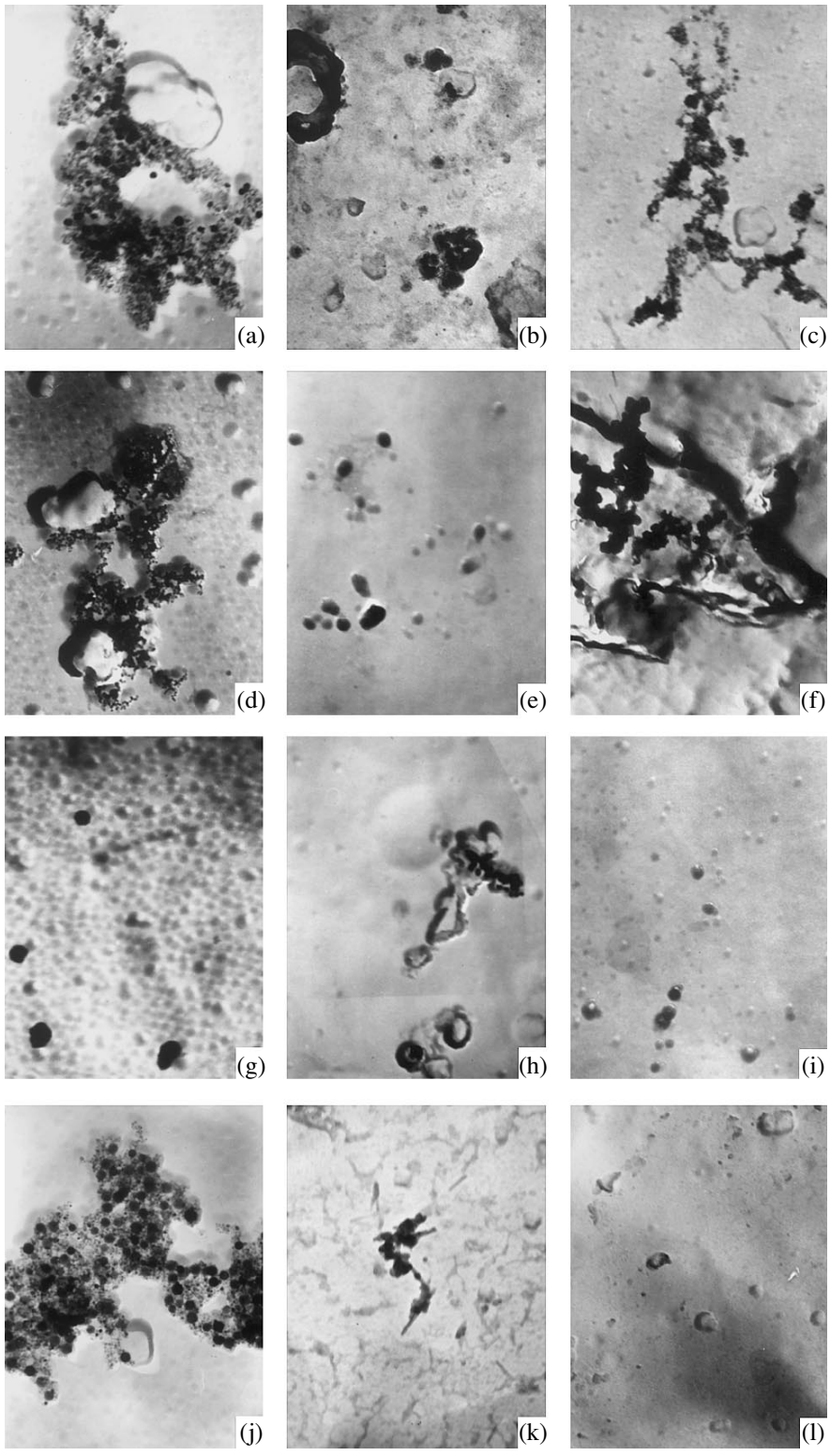

Fig. 1. Microphotographs of the particles formed in the glasses under study: (a–c) $CuInSe_2$, (d–f) $CuInSe_{1.4}Te_{0.6}$, (g–i) $CuInSe_{0.6}Te_{1.4}$, (j–l) $CuInTe_2$. (a, d, g, j) without additional heat treatment; the others after heat treatment (for 6 h) at temperatures (b, e, h, k) 550°C and (c, f, i, l) 600°C. Magnification: 26000.

(quenching) of the melts, nucleation and growth of crystals of the semiconductor phase occur simultaneously and continuously, resulting in an abrupt decrease in supersaturation of the melt, since the total concentration of the semiconductor is rather low and the viscosity high. As a result, a depletion region is formed around a growing nucleus; in this region, the probability of creating new nuclei is reduced, and the growth process stops. Hence, the particles that appear only reach certain sizes. The absence of very small particles (<10 nm) in the microphotographs indicates that the growth of larger particles occurs at the expense of the dissolution of fine particles, which is quite probable at high temperatures. After additional heat treatment following the complete cooling of the glass, new particles are no longer formed, since at the primary stage of the synthesis, most of the semiconductor is already precipitated as a separate phase. The resulting concentration of the particles therefore virtually coincides with their initial concentration, and it is quite possible they will grow slightly, since ion transport at such temperatures can produce additional particle growth at the expense of the neighboring particles. Thus, on the whole, the process of formation of $CuInSe_{2x}Te_{2(1-x)}$ nanoparticles in silicate glasses may be conceived as the melting and dissolution of the crystalline compound in the matrix at high temperatures with subsequent stages of nucleation and growth as the melt cools. The possibility of obtaining very small particles using this method (without any additional growth-limiting procedures) is restricted, because at high temperatures and in the molten glass matrix, the particle growth rate is rather high and the particle size is controlled only by the concentration of the semiconductor introduced into the matrix.

Absorption spectra of a series of glasses immediately after founding are shown in Fig. 2a (transmittance in the near-infrared (IR) region for samples 2 mm thick) and in Fig. 3a (optical density in the visible range for samples 0.2 mm thick). These separate representations of the spectra for the two wavelength regions is used because optical absorption for the same sample thickness may differ severalfold. The transmission spectrum curves in the region of the fundamental edge for the wavelengths 0.6–1.6 μm are relatively steep, and the transmittance gradually increases with wavelength. No pronounced peaks are observed in the spectra, except for the composition with $x = 0.5$ (CuInSeTe, Fig. 2a, curve *3*). This means that, for all compositions except the one above, the band structure of the semiconductor does not significantly change. The anomaly for CuInSeTe at 0.9–1.0 μm mentioned above means that, for this composition, there is an anomaly in the change in the semiconductor band structure. Indeed, such an anomaly is known for the x dependence of the band gap E_g of bulk $CuInSe_{2x}Te_{2(1-x)}$ [27]: for $x = 0.5$, the band gap is narrowest and is equal to $E_g = 0.86$ eV.

The spectra for the glasses with nanoparticles of $CuInSe_2$ and of a solid solution with an excess of selenium ($x = 0.7$) virtually coincide and are shifted to longer wavelengths compared to the other spectra (Fig. 2). As one passes to solid solutions with a larger tellurium content, the spectrum is slightly shifted to higher photon energies, whereas the change in E_g when

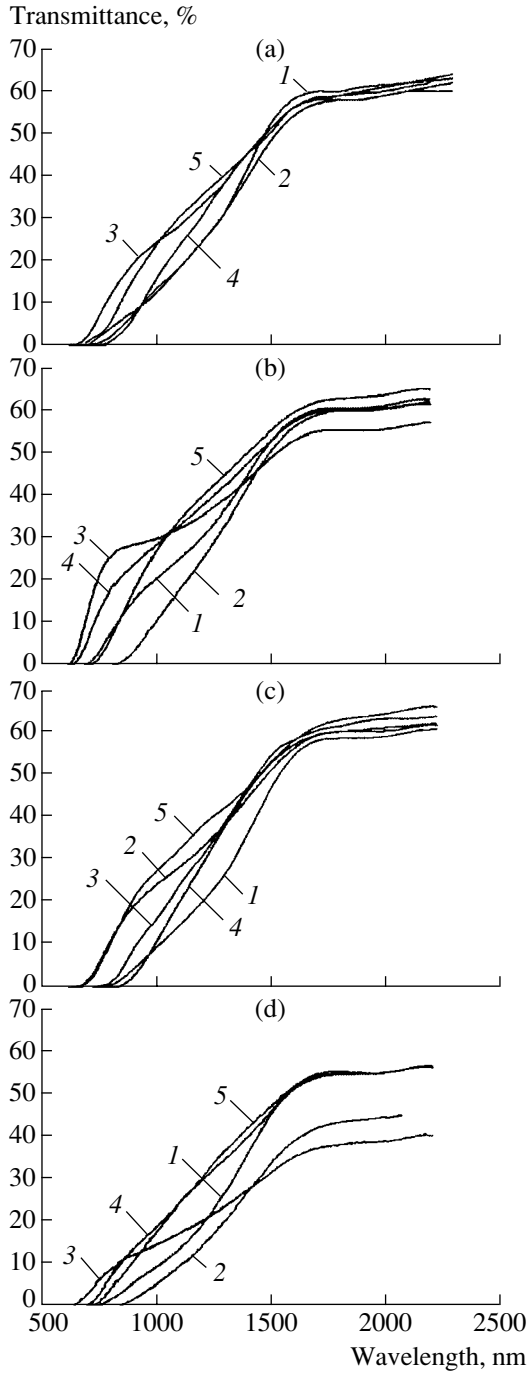

Fig. 2. Transmission spectra of glass samples of thickness 2 mm containing (*1*) $CuInSe_2$, (*2*) $CuInSe_{1.4}Te_{0.6}$, (*3*) CuInSeTe, (*4*) $CuInSe_{0.6}Te_{1.4}$, and (*5*) $CuInTe_2$ nanoparticles; (a) without additional heat treatment and after heat treatment (for 6 h) at temperatures (b) 500, (c) 550, and (d) 600°C.

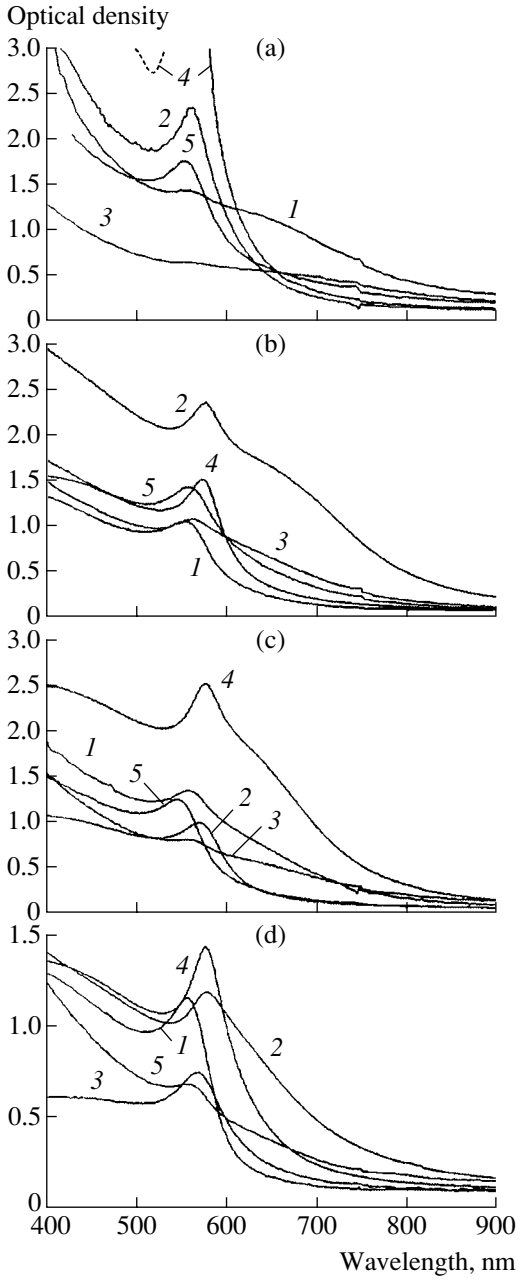

Fig. 3. Absorption spectra of glass samples of thickness 0.2 mm containing (*1*) $CuInSe_2$, (*2*) $CuInSe_{1.4}Te_{0.6}$, (*3*) CuInSeTe, (*4*) $CuInSe_{0.6}Te_{1.4}$, and (*5*) $CuInTe_2$ nanoparticles, (a) without additional heat treatment and after heat treatment (for 6 h) at temperatures of (b) 500, (c) 550, and (d) 600°C.

passing from selenides to tellurides is not monotonic for these compounds, and the minimum mentioned above lies at $x = 0.5$. Such a difference between the spectra of nanoparticles of selenide and selenium-enriched solid solutions, on the one hand, and the spectra of telluride and solid solutions with a tellurium content of 50% or more, on the other, can be related to the difference in the crystal lattice of the nanoparticles for these two types of compositions. The chalcopyrite-type lattice, which is most typical of these compounds in the crystalline state [15, 16], can be transformed into the cubic lattice of the zinc blende type for Te-containing particles; this circumstance gives rise to a nonmonotonic variation in the properties with x. The possibility that a lattice of zinc blende type exists for $CuInTe_2$ and $CuInSe_2$ was mentioned in [28–30].

In the visible region of the spectrum in the curves for optical density for glasses with $CuInSe_2$ nanoparticles (Fig. 3), a wide band is observed in the range of 500–700 nm with a poorly pronounced peak at 560–570 nm. For nanoparticles of solid solutions containing tellurium (except for the composition with $x = 0.5$) and $CuInTe_2$, this band and the peak are more pronounced. The presence of the same peak near 560 nm in samples of different stoichiometric composition may indicate that the presence of tellurium in the composition is responsible for the appearance of this peak; again, the CuInSeTe composition (with $x = 0.5$) is anomalous.

Additional heat treatment of glasses with ternary $CuInSe_2$ and $CuInTe_2$ compounds does not significantly change the shape of the spectral curve in the IR region (Fig. 2). Only after heat treatment of the samples with $CuInSe_2$ particles at 500°C the spectrum shifted to shorter wavelengths, and an additional structure near 0.9 μm appears. For samples with $CuInTe_2$, heat treatment in the temperature range 500–600°C shifts the spectral curve to longer wavelengths without changing its shape. The variation in the spectra in the visible region after heat treatment is more pronounced (Fig. 3): for $CuInSe_2$, a sharp absorption peak appears at ~560 nm and the spectrum is slightly shifted to higher energies. The intensity of the peak in the spectra of the samples with $CuInTe_2$ after heat treatment remains unchanged and the peak is slightly shifted to higher energies.

In the systems containing solid solutions with an excess of selenium and an excess of tellurium (Fig. 2), heat treatment produces a significant shift of the spectrum in the IR region and it becomes complicated: an additional structure appears in the region 0.8–0.9 μm after heat treatment at 550°C ($x = 0.7$) and at 500°C ($x = 0.3$). These changes are consistent with the optical-density curves (Figs. 3b, 3c): the maximum intensity in the region of ~560 nm is reduced. Heat treatment of glasses with CuInSeTe nanoparticles (i.e., with $x = 0.5$) produces a significant change in the shape of the transmission spectrum (Fig. 2): at 500°C, it has a steplike shape and a peak in the region of 0.9–1.0 μm, and at higher temperatures, this structure becomes more diffuse. In the absorption spectra in the visible region (Fig. 3) for these samples after heat treatment, an absorption peak at 560–570 nm appears, whereas for glasses with nanoparticles of other compositions, similar peaks are also observed before additional heat treatment.

The peaks appearing in the visible spectral region may be attributed to the exciton 1*s*–1*s* transition charac-

teristic of nanoparticles with a confinement effect [3]; then the shift of the peak may be related to the change in the particle size stimulated by the effect of temperature on glasses. Such a shift is rather significant for small-size particles (of a few nm), and in the glasses under study, the particles formed have a larger size, so the shift of the exciton peak must be small. At the same time, the position of this peak indicates that, for these glasses with $CuInSe_{2x}Te_{2(1-x)}$ nanoparticles, a pronounced quantum confinement effect occurs producing a high-energy shift (up to 1 eV with respect to the absorption edge of the bulk crystal). In addition to size, other particle characteristics can contribute to a possible explanation of the above shift: the presence of defects due to deviations from stoichiometry of the crystal during the synthesis of glasses at high temperatures, and the crystal structure, which for $CuInSe_2$ particles before heat treatment differs from the structure of solid solutions and $CuInTe_2$ and does not provide conditions for the formation of the excitonic absorption peak. Thus, the zinc blende structure, which is assumed here for $CuInTe_2$ nanoparticles, results in a more pronounced quantum-confinement effect, because at higher symmetry, some energy levels can be degenerate and thus increase E_g compared to the bulk semiconductor with a chalcopyrite lattice of tetragonal symmetry [15, 16]. Hence, the spectra of samples with $CuInTe_2$ particles contain only the contribution from the zinc blende component and are only slightly changed by heat treatment. Significant changes in the spectra occur during the transformation of the crystal lattice stimulated by heating the glass.

Apparently, the crystal structure of $CuInSe_2$ nanoparticles must be classified as a chalcopyrite tetragonal lattice. The absence or weak manifestation of an excitonic peak in the optical-density curves for the samples before heat treatment may be explained by the imperfection of the nanoparticles produced and their thermodynamic instability. A mixed structure that has chalcopyrite and zinc blende (sphalerite) components seems to be characteristic of the nanoparticles of solid solutions. In the $CuInSe_2$–$CuInTe_2$ phase diagram in the interval 950–1070 K, there is a two-phase region in which two separate phases with chalcopyrite (*c*) and sphalerite (*s*) crystal structures coexist (Fig. 4) [22]. The possibility of the coexistence of two nanophases with different crystal structures was suggested, e.g., for ZrO_2 particles [31]. In our case, this assumption can be justified by the fact that crystal lattices of the chalcopyrite and zinc blende types are not very different; to be more exact, chalcopyrite consists of two zinc blende parts, in which the sites of Cu and In atoms are interchanged.

A particular case of the CuInSeTe solid solution deserves a special discussion; in the phase diagram, there are no special features corresponding to it but it has a number of anomalous physical properties in the system of $CuInSe_{2x}Te_{2(1-x)}$ solid solutions [27, 32]. In Fig. 3 the absorption spectra of glasses with CuInSeTe particles feature no peaks before the second heat treatment (Fig. 3a, curve *3*), and, for the samples after heat treatment at 500–550°C, the peaks appear but are less pronounced (Figs. 3b, 3c) compared to solid solutions of other compositions; however, at 600°C, a peak is clearly seen (Fig. 3d). In this case, the most significant changes are observed in the transmission spectra of glasses with particles as well (Fig. 2d, curve *3*). We may assume that this solid solution composition corresponds to the highest disorder, since neither the $CuInSe_2$ nor the $CuInTe_2$ lattice is preferential if the numbers of selenium and tellurium atoms are equal.

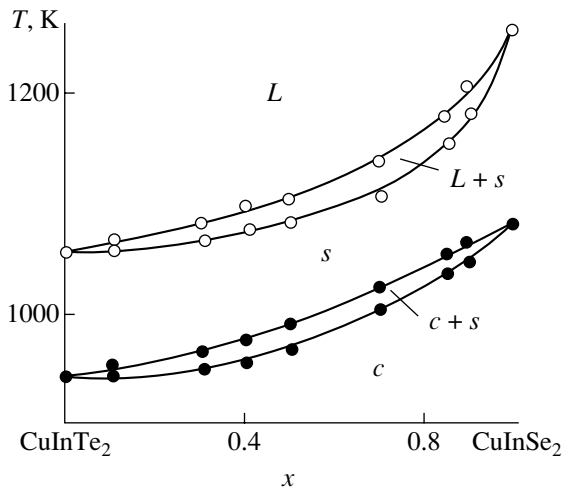

Fig. 4. Phase diagram of the $CuInSe_2$–$CuInTe_2$ system [22]. *L* corresponds to the liquid phase.

As the particle size decreases, the difference in the energies of the crystal lattices can increase due to the contribution of surface energy, and the two-phase state may appear thermodynamically favorable for some solid solution compositions; this results in the appearance of the peaks in excitonic absorption in the zinc blende phase. At the same time, heat treatment facilitates the phase separation and leads to a complication of the spectra both in the visible and in the IR regions, a shift of the position of the absorption edge, and the evolution of the excitonic peaks. The assumptions about the contributions of different phases can be justified after studying the phase composition of glasses with nanoparticles at various *x* at different stages of heat treatment.

4. CONCLUSIONS

We studied the process of formation of nanoparticles of compounds with the general formula $CuInSe_{2x}Te_{2(1-x)}$ ($0 \le x \le 1$) in a glass matrix by directly introducing the corresponding synthesized crystalline semiconductors into the glass charge; we also studied the effect of secondary heat treatment of glasses on their structure and optical properties. We can formulate the main results of the study as follows.

(i) Electron microscopy study allowed us to establish that the semiconductor phase in the cooled glass consists of nanoparticles with an average size of 15–30 nm. The mechanism of particle formation is probably related to the decomposition of the supersaturated solution of the semiconductor in glass; it has a universal character for the method of glass preparation used and is similar to that for glasses with $CuInS_{2x}Se_{2(1-x)}$ ($0 \le x \le 1$) [11] and $CdSe_xTe_{1-x}$ ($0 \le x \le 1$) nanoparticles [25].

(ii) The optical properties of glasses containing $CuInSe_{2x}Te_{2(1-x)}$ nanoparticles depend in a complicated manner on the [Se]/[Te] ratio in the compound introduced, and the anomaly in the properties related to the corresponding anomaly for macroscopic CuInSeTe is observed for the [Se]/[Te] = 1 ratio ($x = 0.5$).

(iii) The effect of secondary heat treatment is not identical for glasses with nanoparticles that have different [Se]/[Te] ratios and manifests itself in the position of both the fundamental absorption edge in the near-IR region and the excitonic peaks in the region of 550–580 nm. The greatest changes occur for the compounds containing both selenium and tellurium (intermediate compositions, $0.3 \le x \le 0.7$); this behavior is related to changes in the nanoparticle crystalline lattice between the chalcopyrite and zinc blende types (the latter is, presumably, stabilized during rapid cooling of glasses for particles enriched with tellurium).

ACKNOWLEDGMENTS

This study was supported by the Ministry of Education of Belarus.

We thank A.V. Kaparikha for his help in performing the electron microscopy experiment.

REFERENCES

1. A. D. Pomogaĭlo, A. S. Rozenberg, and I. E. Uflyand, *Metal Nanoparticles in Polymers* (Khimiya, Moscow, 2000) [in Russian].
2. A. I. Gusev, *Nanocrystalline Materials: Methods of Synthesis and the Properties* (Ural. Otd. Ross. Akad. Nauk, Yekaterinburg, 1998) [in Russian].
3. S. V. Gaponenko, *Optical Properties of Semiconductor Nanocrystals* (Cambridge Univ. Press, Cambridge, 1998).
4. N. Peyghambarian, E. Hanamura, S. W. Koch, *et al.*, in *Nanomaterials: Synthesis, Properties, and Applications*, Ed. by A. S. Edelstein and R. C. Cammarata (Inst. of Physics, Bristol, 1996), p. 395.
5. N. R. Kulish, V. P. Kunets, and M. P. Lisitsa, Opt. Eng. **34**, 1054 (1995).
6. A. Gaĭsin, S. V. Karpov, E. V. Kolobkova, *et al.*, Fiz. Tverd. Tela (St. Petersburg) **41**, 1505 (1999) [Phys. Solid State **41**, 1378 (1999)].
7. Sh. Mochizuki and K. Umezawa, J. Phys.: Condens. Matter **8**, 7509 (1996).
8. N. F. Borrelli and D. W. Smith, J. Non-Cryst. Solids **180**, 25 (1994).
9. A. D. Andreev, E. V. Kolobkova, and A. A. Lipovskii, J. Appl. Phys. **88**, 750 (2000).
10. I. V. Bodnar', A. P. Molochko, and N. P. Soloveĭ, Neorg. Mater. **22**, 1226 (1993).
11. I. V. Bodnar', A. P. Molochko, N. P. Soloveĭ, and V. S. Gurin, Neorg. Mater. **33**, 23 (1997).
12. I. V. Bodnar', A. P. Molochko, and N. P. Soloveĭ, Zh. Prikl. Spektrosk. **63**, 264 (1996).
13. V. S. Gurin, V. V. Sviridov, A. S. Lyakhov, *et al.*, Zh. Neorg. Khim. **41**, 5 (1996).
14. H. Grisaru, O. Palchik, A. Gedanken, *et al.*, Inorg. Chem. **42**, 7148 (2003).
15. N. A. Goryunova, *Complex Diamond-Like Semiconductors* (Sovetskoe Radio, Moscow, 1968) [in Russian].
16. L. L. Kazmerski and S. Wagner, in *Current Topics in Photovoltaics*, Ed. by T. Coutts and J. Meakin (Academic, London, 1985; Mir, Moscow, 1988).
17. V. N. Strekalovskiĭ, Yu. M. Polezhaev, and S. F. Pal'guev, *Oxides with Impurity Disordering* (Nauka, Moscow, 1987) [in Russian].
18. *Physicochemical Properties of Semiconductor Materials: A Handbook*, Ed. by A. V. Novoselova and V. B. Lazarev (Nauka, Moscow, 1979) [in Russian].
19. G. C. Bhar and R. C. Smith, Phys. Status Solidi A **13**, 157 (1972).
20. *Landolt–Börnstein. Physics of Ternary Compounds, New Series, Group III* (Springer, Berlin, 1985), Vol. 17h, p. 47.
21. I. V. Bodnar', A. P. Molochko, and N. P. Soloveĭ, Neorg. Mater. **36**, 1527 (2000).
22. I. V. Bodnar', I. A. Zabelina, B. V. Korzun, and A. P. Chernyakova, Zh. Neorg. Khim. **36**, 1062 (1991).
23. I. V. Bodnar', V. S. Gurin, A. P. Molochko, *et al.*, Zh. Prikl. Spektrosk. **67**, 350 (2000).
24. A. A. Appen, *Chemistry of the Glass* (Khimiya, Leningrad, 1970), p. 354 [in Russian].
25. I. V. Bodnar', V. S. Gurin, A. P. Molochko, *et al.*, Fiz. Tekh. Poluprovodn. (St. Petersburg) **36**, 317 (2002) [Semiconductors **36**, 298 (2002)].
26. V. V. Golubkov, A. I. Ekimov, A. A. Onushchenko, and V. A. Tsekhomskiĭ, Fiz. Khim. Stekla **7**, 397 (1981).
27. I. V. Bodnar' and I. A. Zabelina, Zh. Prikl. Spektrosk. **60**, 320 (1994).
28. N. Yamamoto, S. Ishida, and H. Horisaka, Jpn. J. Appl. Phys., Part 1 **28**, 1780 (1989).
29. F. J. Pern, R. Noufi, A. Mason, and A. Franz, Thin Solid Films **202**, 1299 (1991).
30. J. Vedel, L. Thouin, and D. Lincot, J. Electrochem. Soc. **143**, 2173 (1996).
31. V. Ya. Shevchenko, A. E. Madison, and V. B. Glushkova, Fiz. Khim. Stekla **27**, 419 (2001) [Glass Phys. Chem. **27**, 400 (2001)].
32. L. I. Soliman, Indian J. Pure Appl. Phys. **32**, 166 (1994).

Translated by I. Zvyagin

Semiconductors, Vol. 38, No. 12, 2004, pp. 1409–1415. Translated from Fizika i Tekhnika Poluprovodnikov, Vol. 38, No. 12, 2004, pp. 1455–1462.

LOW-DIMENSIONAL SYSTEMS

Intersubband Absorption of Light in Selectively Doped Asymmetric Double Tunnel-Coupled Quantum Wells

V. L. Zerova*^, V. V. Kapaev, L. E. Vorob'ev*, D. A. Firsov*, S. Schmidt***, E. A. Zibik***, A. Seilmeier***, and E. Towe******

**St. Petersburg State Polytechnical University, St. Petersburg, 195251 Russia*

^e-mail: VZerova@rphf.spbstu.ru

***Lebedev Physical Institute, Russian Academy of Sciences, Moscow, 117924 Russia*

****Institute of Physics, University of Bayreuth, Germany*

*****Carnegie Mellon University, Pittsburgh, PA 15213, USA*

Submitted May 14, 2004; accepted for publication May 24, 2004

Abstract—The spectrum of equilibrium intersubband absorption has been studied in selectively doped asymmetrical double tunnel-coupled quantum wells designed for research into the modulation of IR light in a longitudinal electric field. The comparison of calculated and experimental spectra at different temperatures is carried out. In calculations, the influence of the space charge on the energy spectra of electrons and the difference in the electron effective mass in different subbands are taken into account. The data obtained on the intersubband absorption spectra in equilibrium conditions and under electron excitation by high-power picosecond pulses of light in the mid-IR range allow us to refine the energy spectrum of electrons in the actual structure. © *2004 MAIK "Nauka/Interperiodica".*

1. INTRODUCTION

The current interest in optical intersubband electron transitions in quantum wells (QW) is related to the advent of new QW-based optoelectronic devices for the mid-IR range: unipolar noninjection lasers, photodetectors, and modulators of IR light. Asymmetrical tunnel-coupled QWs (ATCQW) offer new possibilities for the design of devices. For example, ATCQWs are used as an active region in quantum-cascade lasers [1], fountain lasers with intraband optical pumping [2], and high speed modulators of IR light [3, 4].

The ATCQWs studied in this paper (Fig. 1) are designed for research into the modulation of IR light in a strong longitudinal electric field. When electrons are heated by the longitudinal field, they are redistributed in real space: the tunneling of hot electrons from subband $e1$ of the narrow well to the wide well, with the filling of subband $e2$, is possible. Owing to the increase in electron density in subband $e2$ of the wide well, the light absorption coefficient for intersubband transitions $e2 \longrightarrow e3$ must increase.

As the first stage in this study, we investigate the spectra of intersubband light absorption in selectively doped ATCQWs, which allows us to determine the energy spectrum of electrons.

2. OBJECT OF STUDY

The absorption was studied in a structure containing 150 pairs of ATCQWs. The structure was MBE-grown on a semi-insulating GaAs substrate. QW pairs were separated by $Al_{0.42}Ga_{0.58}As$ barriers, which were not transparent for tunneling. The central part of barriers was selectively doped with Si, so that the surface density of electrons in QWs was $n_s = 3 \times 10^{11}$ cm^{-2}. One of the tunnel-coupled QWs was formed by a 5-nm-thick GaAs layer; the other, by a 7.5-nm-thick $Al_{0.06}Ga_{0.94}As$ layer; the thickness of the tunnel-transparent $Al_{0.42}Ga_{0.58}As$ barrier between the wells was 2.5 nm (Fig. 1).

The energy spectrum and wave functions of electrons taking into account the space charge were obtained by self-consistent solution of the Poisson and Schrödinger equations. According to our calculations, five energy levels exist in the system of tunnel-coupled QWs. Levels $e1$ and $e4$ are associated with the narrow QW, $e2$ and $e3$ with the wide one. Therefore, the elec-

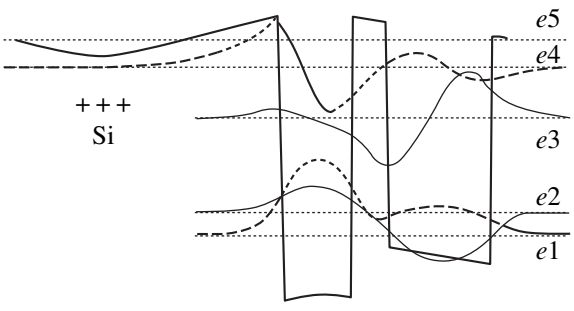

Fig. 1. Profile of potential, energy levels ei, and smooth envelopes of the electron wave functions on levels in an ATCQW.

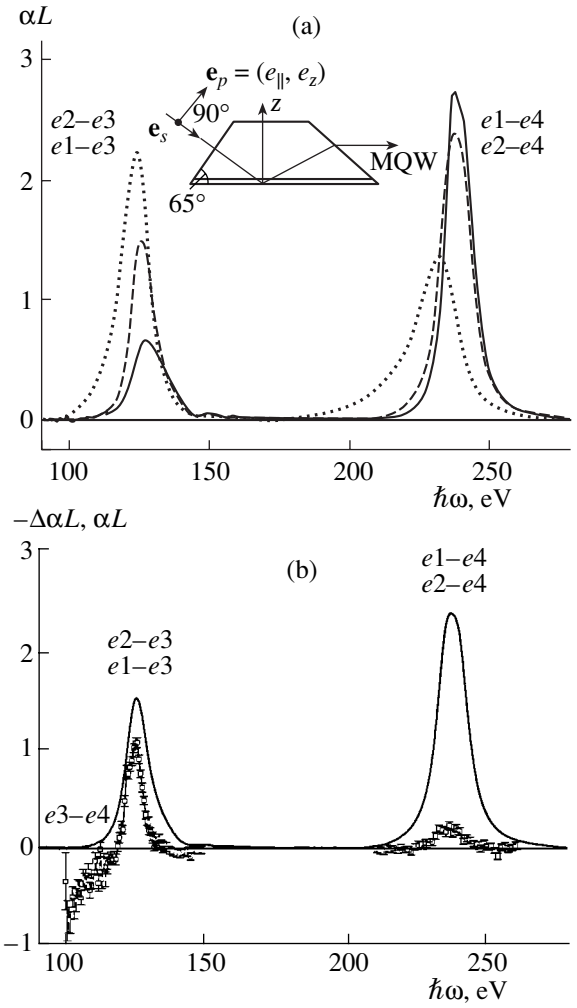

Fig. 2. Experimental absorption spectra and changes in absorption with high-power intersubband excitation of a structure with multiple ATCQWs (MQW). Inset: the configuration of the experiment to study the absorption of polarized light. (a) Equilibrium absorption spectra αL at different temperatures: solid line, 14 K; dashed line, 80 K; dotted line, 300 K. (b) Points: the change in absorption $-\Delta\alpha L$ under intersubband excitation at the frequency of the long-wavelength peak of the equilibrium absorption at $T = 80$ K; solid line, the equilibrium absorption spectrum αL at the same temperature.

tron wave function in subband $e1$ is almost completely localized within the narrow well, whereas the electron wave function in subband $e2$ is localized mainly within the wide well (Fig. 1). This implies that, under equilibrium conditions, the majority of electrons are concentrated in the narrow QW. The level $e5$ is a bound state of the QW in a wide barrier, which arises due to the distortion of the potential of the structure by the space charge.

At the temperature $T = 80$ K, the calculated energy levels (reckoned from the chemical potential level) are $\mathscr{E}_1 = -5.65$ meV, $\mathscr{E}_2 = 5.13$ meV, $\mathscr{E}_3 = 138.95$ meV, $\mathscr{E}_4 = 236.59$ meV, and $\mathscr{E}_5 = 265.23$ meV. The values of the matrix elements of the z coordinate, $z_{ij} = |\int \psi_j^*(z) z \psi_i(z) dz|$, which describe the probabilities of intersubband optical transitions $ei \longrightarrow ej$ (where $\psi_i(z)$ and $\psi_j(z)$ are the smooth envelopes of the electron wave functions in the initial and final states), are $z_{13} = 0.165$ nm, $z_{23} = 2.12$ nm, $z_{14} = 1.26$ nm, and $z_{24} = 0.52$ nm. The maximum contribution to the intersubband absorption is made by the transitions between the levels associated with one and the same QW, whose wave functions overlap considerably. This is the source of the large difference between the values of z_{ij} for different pairs of levels: $z_{23} \gg z_{13}$, $z_{14} > z_{24}$.

3. EXPERIMENTAL INVESTIGATION OF THE INTERSUBBAND ABSORPTION OF LIGHT

Figure 2a shows the experimentally obtained equilibrium absorption spectra $\alpha(\hbar\omega)L$ (ω is the frequency of light, L the effective optical path, α the absorption coefficient) in the structure under study for different temperatures. The absorption of light in p-polarization was measured using a Fourier spectrometer; the experimental configuration is shown in the inset to Fig. 2a. The spectra comprise two absorption bands. The spectral position of these bands allows us to attribute the long-wavelength band to $e1 \longrightarrow e3$ and $e2 \longrightarrow e3$ transitions, and the short-wavelength one to $e1 \longrightarrow e4$ and $e2 \longrightarrow e4$. Peaks related to transitions from levels $e1$ and $e2$ are not resolved in the spectra.

Note that, in analyzing the absorption spectrum, it was necessary to correct the initially calculated QW parameters, because they did not correspond to the experimental absorption spectrum. Specifically, the analysis of the experimental spectrum shows that the energy spacing Δ_{12} between levels $e1$ and $e2$ is significantly less than the prescribed value of 24 meV. We believe that the real parameters of the grown QWs differ from the calculated ones. The parameters listed above are the corrected values.

The energy Δ_{12} was refined by analyzing the change (decrease) in absorption, $-\Delta\alpha(\hbar\omega)L$, at high-power intersubband excitation of electrons at 80 K (Fig. 2b). The experiments were performed using pump-and-probe spectroscopy with a picosecond time resolution. A high-power pumping pulse with an energy corresponding to the long-wavelength peak of the equilibrium absorption (125 meV) excited carriers from level $e2$ (and, to a lesser extent, from $e1$) to level $e3$. The change in absorption was measured at different instants of time, using a weak probe pulse whose frequency was tuned within the absorption bands. In this situation, a decrease in absorption was observed in the range of both long- and short-wavelength peaks; the latter corresponds to transitions to level $e4$. Furthermore, the spectrum exhibited a range with a peak at 102 meV, where the nonequilibrium absorption was stronger than the equilibrium one.

The energy of 102 meV corresponds to $e3 \longrightarrow e4$ transitions with the frequency $\Delta_{34}/\hbar$. This fact allows us to suggest that the absorption at this frequency is photoinduced and is related to the transition of photoexcited electrons from level $e3$ to level $e4$. Based on the relation between the values of optical matrix elements $z_{23} \gg z_{13}$ and $z_{14} > z_{24}$, we can assume that the frequency of the long-wavelength peak in equilibrium absorption corresponds to the frequency of the $e2 \longrightarrow e3$ transition (i.e., equals $\Delta_{23}/\hbar$), and the frequency of the short-wavelength peak corresponds to the $e1 \longrightarrow e4$ transition (i.e., equals $\Delta_{14}/\hbar$). From the known energies Δ_{14}, Δ_{23}, and Δ_{34}, we can calculate the distance between the first and second levels: $\Delta_{12} = \Delta_{14} - \Delta_{34} - \Delta_{23} \approx 237 - 125 - 102 \approx 10$ meV.

The value $\Delta_{12} = (10 \pm 1)$ meV, determined at 80 K, agrees well with the other specific features of the experimental equilibrium absorption spectrum. Specifically, for this value of Δ_{12} and the broadening of the absorption band ~10 meV, the absorption peaks related to the $e1 \longrightarrow e4$ and $e2 \longrightarrow e4$ transitions are not resolved spectrally, though the matrix elements for these transitions differ only by a factor of 2.

When we selected the QW parameters at which $\Delta_{12} \approx 10$ meV, we increased the thickness of the tunnel-transparent barrier by 0.5 nm, decreased the width of the wide QW by 0.8 nm, and also decreased the initially prescribed Al content in the wide QW from 10 to 6%.

When varying the position of the bottom of the wide well, we paid attention to the behavior of the optical matrix elements. It turned out that, at a certain composition of the material of the wide QW, the matrix element z_{13} for the $e1 \longrightarrow e3$ transition can be zero. In our structure, the matrix element z_{13} is indeed very small, because the long-wavelength peak does not split into two peaks for the $e1 \longrightarrow e3$ and $e2 \longrightarrow e3$ transitions even at low temperatures.

4. CALCULATION OF EQUILIBRIUM ABSORPTION SPECTRA AT DIFFERENT TEMPERATURES

The absorption coefficient $\alpha_{ij}(\hbar\omega)$ for z-polarized light of frequency ω for the electron transition from the states of subband ei to those of subband ej can be found in the 1st approximation of the perturbation theory, as was done in [5]:

$$\alpha_{ij}(\hbar\omega) = \frac{4\pi^2 e^2}{cSL\sqrt{\varepsilon_\infty}\omega m_0^2} \times \sum_{\mathbf{k}_i}\sum_{\mathbf{k}_j}\left|e_z\delta_{\mathbf{k}_i,\mathbf{k}_j}\int\psi_j^*(z)\hat{p}_z\psi_i(z)dz\right|^2 \times [f_i(\mathscr{E}_i) - f_j(\mathscr{E}_j)]\delta[\mathscr{E}_j - \mathscr{E}_i - \hbar\omega], \quad (1)$$

$$\mathscr{E}_i = \mathscr{E}_{0i} + \frac{\hbar^2 k_i^2}{2m_i}, \quad \mathscr{E}_j = \mathscr{E}_{0j} + \frac{\hbar^2 k_j^2}{2m_j}, \quad (2)$$

where $\mathbf{k}_i$ and $\mathbf{k}_j$ are 2D wave vectors of electrons in subbands ei and ej ($k_i = |\mathbf{k}_i|$, $k_j = |\mathbf{k}_j|$); the Kronecker δ symbol reflects the conservation law for the wave vector $\mathbf{k}_i \equiv \mathbf{k}_j \equiv \mathbf{k}$; $\psi_i(z)$ and $\psi_j(z)$ are the smooth envelopes of the electron wave functions in the initial and final states; $f_i(\mathscr{E}_i)$ and $f_j(\mathscr{E}_j)$, the Fermi distribution functions of electrons in subbands ei and ej; ε_∞, the high-frequency dielectric constant of GaAs (assuming that the refractive indices for the well and barrier materials are similar); c, the velocity of light in free space; e, the elementary charge; e_z, the z component of the polarization vector $\mathbf{e}_p$; S, the area of the structure; m_0, the free electron mass; m_i, m_j, and $\mathscr{E}_i$, $\mathscr{E}_j$, the effective masses and energies of electrons in the initial and final states; $\mathscr{E}_{0i}$ and $\mathscr{E}_{0j}$, the bottom energies of subbands ei and ej; and $\hat{p}_z$, the z component of the momentum operator, whose matrix element can be expressed via the dipole moment of the transition: $(\hat{p}_z)_{ij} = i\omega_{ij}m_0 z_{ij}$. Substituting this into (1) and replacing the summation over $\mathbf{k}$ by integration, we obtain the interband absorption coefficient

$$\alpha_{ij}(\hbar\omega) = \frac{4\pi^2 e^2 \omega_{ij}^2}{cSL\sqrt{\varepsilon_\infty}\omega}\cos^2\theta z_{ij}^2 \times \int\frac{2S}{(2\pi)^2}[f_i(\mathscr{E}_i) - f_j(\mathscr{E}_j)]\delta[\mathscr{E}_j - \mathscr{E}_i - \hbar\omega]d\mathbf{k}, \quad (3)$$

where $\omega_{ij} = (\mathscr{E}_j - \mathscr{E}_i)/\hbar$ is the frequency of the intersubband transition $ei \longrightarrow ej$, which generally depends on k ($k = |\mathbf{k}|$), and θ is the angle between the polarization vector and the z axis.

The spectral broadening of the absorption peak for the intersubband transition $ei \longrightarrow ej$ can be taken into account, for example, by using the Lorentzian function [6]. Several researchers (see, e.g., [7]) have proposed using, instead of the Lorentzian function, some other functions with a faster decay, because they allow one to describe the experimental data better. We calculated the absorption spectrum with the broadening taken into account in two ways, using either a Lorentzian function or a Gaussian function. If the broadening is taken into account, the possible variation of the transition frequency $\hbar\omega_{ij}$ is taken into account phenomenologically. If the broadening is taken into account in the Lorentzian form,

$$\tilde{\alpha}_{ij}(\hbar\omega) = \frac{\int_{\hbar\omega_{ij}}^{\infty}\alpha_{ij}(\hbar\omega_{ij})\{(\Gamma_i/\pi)/[\Gamma_i^2 + (\hbar\omega - \hbar\omega_{ij})^2]\}d\hbar\omega_{ij}}{\int_{\hbar\omega_{ij}}^{\infty}\{(\Gamma_i/\pi)/[\Gamma_i^2 + (\hbar\omega - \hbar\omega_{ij})^2]\}d\hbar\omega_{ij}}, \quad (4)$$

where $\alpha_{ij}(\hbar\omega_{ij})$ is described by Eq. (3) with the substitution $\hbar\omega \longrightarrow \hbar\omega_{ij}$ and $2\Gamma_i$ is the FWHM of the absorption line for the $ei \longrightarrow ej$ transitions. If the broadening is considered in the Gaussian form,

$$\tilde{\alpha}_{ij}(\hbar\omega) = \frac{(1/\pi\Gamma_i)\int_{\hbar\omega_{ij}} \alpha_{ij}(\hbar\omega_{ij})\exp(-[(\hbar\omega-\hbar\omega_{ij})/\Gamma_i]^2)d\hbar\omega_{ij}}{(1/\pi\Gamma_i)\int_{\hbar\omega_{ij}} \exp(-[(\hbar\omega-\hbar\omega_{ij})/\Gamma_i]^2)d\hbar\omega_{ij}}. \quad (5)$$

Note that different broadening parameters Γ_1 and Γ_2 correspond to electron transitions from subbands $e1$ and $e2$. As electrons in subbands $e1$ and $e2$ are mainly localized in QWs of different width and the collision broadening, which makes the main contribution to the spectral broadening of the absorption line, depends on the QW width, the values of Γ_1 and Γ_2 may differ. The dependence of broadening on the QW width is defined mainly by the rate of the electron scattering on the irregularities of the QW boundaries, and it can be quite strong.

The absorption coefficient spectrum is obtained by the summation of the absorption spectra (4) or (5) for separate transitions:

$$\alpha(\hbar\omega) = \sum_{i,j} \tilde{\alpha}_{ij}(\hbar\omega). \quad (6)$$

Changes in temperature cause a modification of the electron energy spectrum and wave functions, due to the changed impact of the space charge. As temperature increases, the electron filling increases in subband $e2$, and its wave function is localized mainly in the wide QW. Therefore, at the transition from the first to the second subband, electrons are simultaneously redistributed in real space. This leads to a more uniform distribution of electrons between the wells, and, subsequently, to a reduction in the effect of the space charge. As a result, levels $e2$ and $e3$, which are associated with the wide QW, are shifted relative to levels $e1$ and $e4$, which are associated with the narrow QW. Thus, when temperature changes, electrons are redistributed between the levels in accordance with the distribution function taking into account the change in the energy spacing between the levels. The modification of the energy spectrum results in a modification of the matrix elements z_{ij}.

Figures 3a–3d show temperature dependences of the energy spacing between the two lowest levels Δ_{12}, matrix elements z_{ij}, chemical potential, and electron densities on levels $e1$ and $e2$. These dependences determine the behavior of the absorption coefficient with temperature. It can be seen that, as temperature increases from 14 to 300 K, the energy Δ_{12} increases by about 2.5 meV, and the matrix elements z_{ij} change only slightly. The most significant is the temperature dependence of z_{13} and z_{24}, which are determined by the wave functions of levels associated with different wells. The electron density on the two lowest levels n_i ($i = 1, 2$) can be found using the Fermi distribution function (here, the electron energy $\mathscr{E}$ is reckoned from the bottom of subband $e1$):

$$\begin{aligned} n_1(T) &= \frac{m_1}{\pi\hbar^2}\int_0^\infty \left\{1/\left[\exp\frac{\mathscr{E}-\mathscr{E}_F(T)}{k_BT}+1\right]\right\}d\mathscr{E} \\ &= \frac{m_1k_BT}{\pi\hbar^2}\ln\left(1+\exp\frac{\mathscr{E}_F(T)}{k_BT}\right), \\ n_2(T) &= \frac{m_2}{\pi\hbar^2}\int_{\Delta_{12}}^\infty \left\{1/\left[\exp\frac{\mathscr{E}-\mathscr{E}_F(T)}{k_BT}+1\right]\right\}d\mathscr{E} \\ &= \frac{m_2k_BT}{\pi\hbar^2}\ln\left(1+\exp\frac{\mathscr{E}_F(T)-\Delta_{12}(T)}{k_BT}\right), \end{aligned} \quad (7)$$

where $\mathscr{E}_F(T)$ is the chemical potential at the temperature T and k_B is the Boltzmann constant. The energy $\mathscr{E}_F(T)$ can be found from the equation which is obtained when (7) is substituted into the condition $n_s = n_1 + n_2$. The total number of electrons in an ATCQW, n_s, is determined mainly by the sum of electron densities on levels $e1$ and $e2$, because the upper levels $e3$ and $e4$ are not filled under equilibrium conditions, $n_j \approx 0$ ($j = 3, 4$).

Temperature dependences of the parameters Γ_1 and Γ_2 are defined by the mechanisms of electron scattering in QWs. At different temperatures, different scattering mechanisms can dominate. For example, at low temperatures, the broadening is mainly defined by the rate of scattering on the irregularities of the QW boundaries and by the processes of optical phonon emission. At high temperatures, along with these processes, a significant contribution is made by the absorption of optical phonons. We determined Γ_1 and Γ_2 as fitting parameters by comparing the theoretically calculated spectrum with that obtained experimentally.

At first, we consider the situation with equal electron effective masses in different subbands: $m_i = m_j = m$. Then $\hbar\omega_{ij} = \mathscr{E}_{0j} - \mathscr{E}_{0i} = \Delta_{ij}$, where $\Delta_{ij} = \text{const}(k)$ is the energy spacing between levels ei and ej at $k = 0$. Therefore, the dependence on $\mathbf{k}$ is present in (3) only in the distribution functions, and the integration over $\mathbf{k}$ yields the difference between the electron densities in subbands ei and ej:

$$\int \frac{2S}{(2\pi)^2}[f_i(\mathscr{E}_i) - f_j(\mathscr{E}_j)]d\mathbf{k} = S(n_i - n_j). \quad (8)$$

In this case, taking into account the temperature dependence, the relation (3) for the coefficient of intersubband absorption in transition $ei \longrightarrow ej$ takes the form

$$\alpha_{ij}(\hbar\omega, T) = \frac{K_{ij}(T)z_{ij}^2(T)}{\hbar\omega}n_i(T)\delta[\hbar\omega - \Delta_{ij}(T)], \quad (9)$$

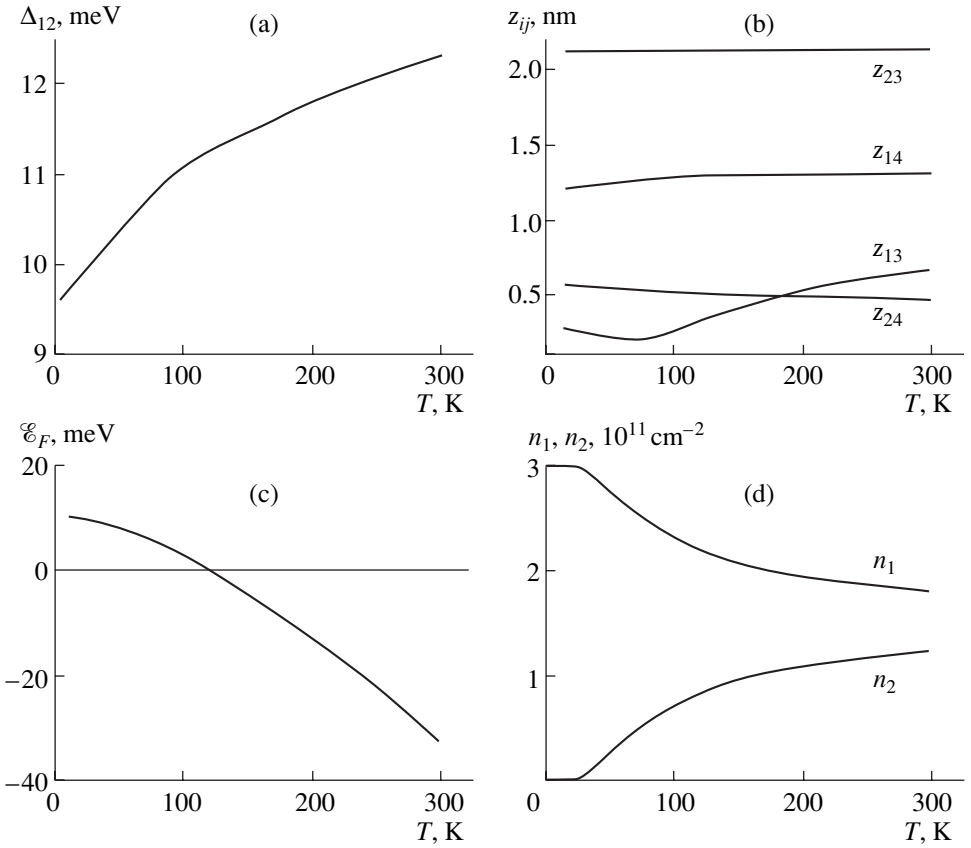

Fig. 3. Temperature dependences of the quantities defining the intersubband absorption in ATCQWs. (a) Energy spacing between the lowest subbands, Δ_{12}; (b) optical matrix elements, z_{ij}; (c) chemical potential, $\mathscr{E}_F$; (d) distribution of electrons between the lowest subbands (densities n_1, n_2).

where the filling of upper levels is neglected: $n_j \approx 0$ (j = 3, 4); the coefficients $K_{ij}(T)$ contain frequency-independent terms:

$$K_{ij}(T) = \frac{4\pi^2 e^2 \Delta_{ij}^2(T)}{x\sqrt{\varepsilon_\infty} L\hbar}. \quad (10)$$

The Lorentzian or Gaussian broadening can be taken into consideration by substituting (9) into (4) or (5), respectively.

Figure 4 shows the comparison of spectra calculated for the Lorentzian or Gaussian broadening of peaks with the experimental absorption spectrum at T = 14 K. For clarity, in this figure we superposed the positions of calculated and experimental spectra, whereas the real calculated spectra are slightly blue-shifted in respect to the experimental absorption spectrum. At T = 14 K, the long- and short-wavelength peaks are shifted by 6 and 3 meV, respectively. This discrepancy may be related to the effect of depolarization and exchange interaction, which were disregarded in our model, on the position of energy levels. As can be seen in Fig. 4, the agreement between the calculated and experimental spectrum is better in the calculation using the Gaussian broadening than in the Lorentzian one.

However, at higher temperatures good agreement with the experimental spectrum is not obtained. Assuming that this is due to the enhanced effect of the nonparabolicity of the energy subbands at elevated temperatures, we took into account in further calculations the difference between the electron effective masses in different subbands, $m_i \neq m_j$, in terms of the Ekenberg model [8]. In doing so, we also assumed that the dispersion relations within the subbands remain parabolic but differ in the longitudinal effective masses of electrons near k = 0, whereas the transverse effective masses remain unchanged:

$$m_{i,j} = m[1 + (2\alpha + \beta)\mathscr{E}_{i,j}]. \quad (11)$$

Here, $m = 0.0665m_0$ is the electron effective mass in GaAs, and $\alpha = 0.64$ (eV)$^{-1}$ and $\beta = 0.7$ (eV)$^{-1}$ are parameters [8]. The relation (11) is a fair approximation for a QW width of ~5 nm, and it is independent of the boundary conditions. For T = 80 K, the masses determined from (11) are $m_1 = 0.0665m_0$, $m_2 = 0.0796m_0$, $m_3 = 0.0975m_0$, and $m_4 = 0.1106m_0$. Now we use the inequality $m_i \neq m_j$ in the dispersion relations. We introduce the reduced mass m_{ij}, which is determined by the

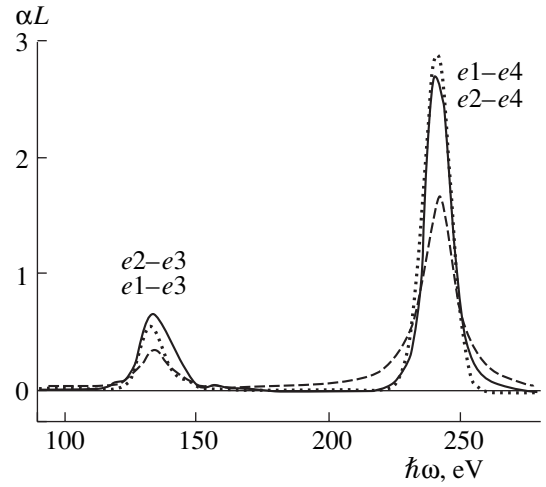

Fig. 4. Equilibrium absorption spectrum at $T = 14$ K (nonparabolicity is disregarded). Dashed line, calculation with Lorentzian broadening; dotted line, Gaussian broadening; solid line, experiment.

masses in both subbands, and the corresponding energy $\tilde{\mathscr{E}}_{ij}$:

$$m_{ij}^{-1} = \frac{m_j - m_i}{m_j m_i}, \quad \tilde{\mathscr{E}}_{ij} = \frac{\hbar^2 k^2}{2m_{ij}}. \tag{12}$$

Then, the transition frequency $\hbar\omega_{ij} = \mathscr{E}_j - \mathscr{E}_i = \Delta_{ij} - \tilde{\mathscr{E}}_{ij}$ starts to depend on **k**, and the δ function in (3) takes the form $\delta[\Delta_{ij} - \tilde{\mathscr{E}}_{ij} - \hbar\omega]$. In this case, an analytical integration over **k** in (3) with the use of the δ function is possible:

$$\alpha_{ij}(\hbar\omega) = \frac{K_{ij}(T) z_{ij}^2(T)}{\hbar\omega} \times \frac{2\tilde{m}_{ij}(T)}{\hbar^2} \Big/ \left\{ \exp\left(\frac{\tilde{m}_{ij}(T)}{m_i(T)} \frac{[\Delta_{ij}(T) - \hbar\omega]}{k_B T} - \frac{\mathscr{E}_F(T)}{k_B T} \right) + 1 \right\}. \tag{13}$$

The Lorentzian and Gaussian broadening can be taken into account by substituting (13) into (4) or (5), respectively.

The summation of the obtained absorption coefficients for separate transitions $\tilde{\alpha}_{ij}(\hbar\omega_{ij})$, in accordance with (6), yields the absorption coefficient spectrum $\alpha_{ij}(\hbar\omega_{ij})$ taking into account the nonparabolicity of the energy subbands. Figure 5 shows the contribution of separate transitions to the long- and short-wavelength absorption peaks. In accordance with the relation between the matrix elements, $z_{23} \gg z_{13}$, the long-wavelength peak is defined mainly by the electrons from the second level. The transitions from the first level make a significant contribution only at low temperatures, when virtually all electrons are localized on this level (Fig. 5a). In contrast, the short-wavelength peak is defined mainly by the electrons from the first level, because $z_{14} > z_{24}$. Therefore, the contribution of $e2 \longrightarrow e4$

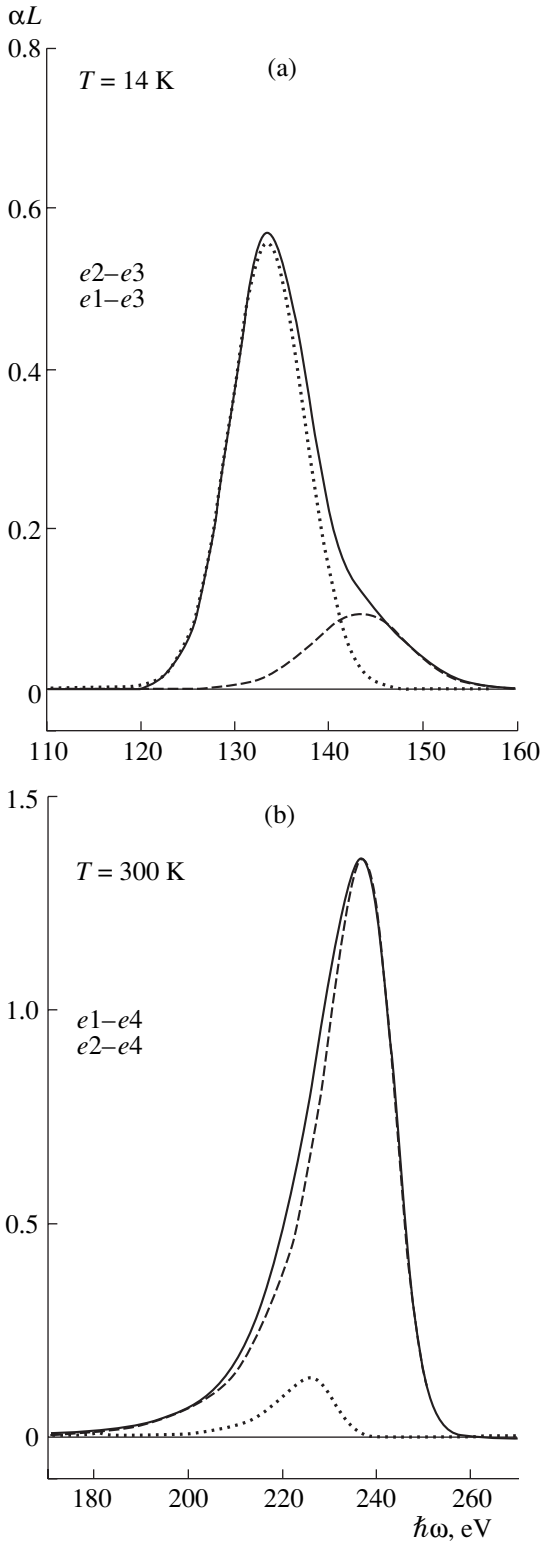

Fig. 5. Contribution of separate electron transitions to the equilibrium absorption spectrum. (a) Long-wavelength peak, $T = 14$ K; (b) short-wavelength peak, $T = 300$ K. Dashed and dotted lines, calculations for electron transitions from the first and second levels, respectively; solid line, total contribution to absorption. The calculations were performed taking into account the nonparabolicity and Gaussian broadening.

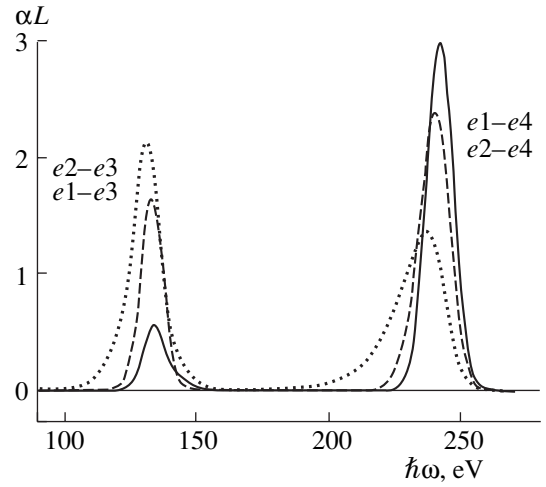

Fig. 6. Equilibrium absorption spectrum calculated taking into account the Gaussian broadening and the nonparabolicity effect. Temperature: solid line, 14 K; dashed line, 80 K; dotted line, 300 K.

transitions is noticeable only at high temperatures, when the filling of the second level is large (Fig. 5b).

Figure 6 shows the calculated spectra of the intersubband absorption coefficient for three temperatures, for the case of $m_i \neq m_j$. They agree well with the experimental equilibrium spectra (see Fig. 2a). The spectra consist of two absorption bands at frequencies close to those of the $e1, e2 \longrightarrow e3$ and $e1, e2 \longrightarrow e4$ transitions. As temperature increases, the absorption increases in the first and decreases in the second peak. Since two transitions contribute to each peak, the absorption is mainly defined by the filling of that level for which the probability of optical transition is the highest.

The temperature dependence of the width of the absorption peaks is related to two factors. First, the specific times of the principal scattering mechanisms, which define the broadening, can depend on temperature. The best-fit values of Γ_1 and Γ_2 are about 7 and 5.6 meV, respectively. Their relative values correlate with the known dependences of the probability of scattering on the interface irregularities as functions of the QW width [9]. The variation in these values with temperature was found to be negligible, which may be attributed to the enhancement of some scattering mechanisms simultaneously with the depression of other ones. Second, two transitions with different frequencies contribute to the width of each peak (see Figs. 5a, 5b).

For example, the long-wavelength peak at $T = 14$ K is rather wide. This can be explained by the fact that at low temperatures the contributions of $e1 \longrightarrow e3$ and $e2 \longrightarrow e3$ transitions to the total absorption peak are virtually comparable, and the total width of the absorption band is defined by the widths of two partially overlapped peaks. As temperature increases, the electron density on the second level increases, and, since $|z_{23}|^2 \gg |z_{13}|^2$, the contribution of $e2 \longrightarrow e3$ transitions to the absorption band of the first peak sharply increases and becomes dominant and, consequently, defines its width.

As temperature increases, both peaks demonstrate the rise of a long-wavelength shoulder, which arises due to the nonparabolicity of the quantum-confinement subbands.

In addition, as temperature increases, the red shift of the absorption peaks is observed. When the temperature increases from 14 to 300 K, the long-wavelength peak shifts by 3 meV, and the short-wavelength one by 5 meV. These shifts are well described in terms of the proposed model, with the account for nonparabolicity of subbands and using the Gaussian function.

5. CONCLUSION

The spacing between the energy levels in ATCQWs was determined from the analysis of intersubband absorption spectra. The most important result is that obtained in determining the energy spacing between the lowest subbands in an ATCQW, $\Delta_{12} = (10 \pm 1)$ meV. This distance defines the redistribution of electrons in real space, which gives rise to the modulation of mid-IR light in the longitudinal electric field.

The simulated theoretical spectra of intersubband absorption of light by electrons in ATCQWs under equilibrium conditions at different temperatures agree well with the experimental data. Magnitudes and widths of the absorption peaks at different temperatures are accounted for by the corresponding values of the electron density at lower levels and the values of optical matrix elements of intersubband transitions. The asymmetry and temperature shift of the spectral peaks are related to the nonparabolicity of the quantum-confinement subbands.

ACKNOWLEDGMENTS

This study was supported by programs of the Russian Foundation for Basic Research, the International Science & Technology Center, and the Ministry of Education and Science of the Russian Federation.

REFERENCES

1. J. Faist, F. Capasso, D. L. Sivco, *et al.*, Science **264**, 553 (1994).
2. O. Gauthier-Lafaye, P. Boucaud, F. H. Julien, *et al.*, Appl. Phys. Lett. **71**, 3619 (1997).
3. E. Dupont, D. Delacourt, V. Berger, *et al.*, Appl. Phys. Lett. **62**, 1907 (1993).
4. V. Berger, E. Dupont, D. Delacourt, *et al.*, Appl. Phys. Lett. **61**, 2072 (1992).
5. L. E. Vorob'ev, E. L. Ivchenko, D. A. Firsov, and V. A. Shalygin, *Optical Properties of Nanostructures* (Nauka, St. Petersburg, 2001) [in Russian].
6. S. W. Corzine, Ran-Honh Yan, and L. A. Coldren, in *Quantum Well Lasers*, Ed. by Peter S. Zory, Jr. (Academic, Boston, 1993), Chap. 1, p. 17.
7. Masahio Asada, in *Quantum Well Lasers*, Ed. by Peter S. Zory, Jr. (Academic, Boston, 1993), Chap. 2, p. 97.
8. U. Ekenberg, Phys. Rev. B **40**, 7714 (1989).
9. V. A. Kulbachinskii, N. V. Kytin, V. I. Kadushkin, *et al.*, J. Appl. Phys. **75**, 2081 (1994).

Translated by D. Mashovets

Semiconductors, Vol. 38, No. 12, 2004, pp. 1416–1418. Translated from Fizika i Tekhnika Poluprovodnikov, Vol. 38, No. 12, 2004, pp. 1463–1465.

AMORPHOUS, VITREOUS, AND POROUS SEMICONDUCTORS

Size Distribution of Cobalt Nanoclusters in an Amorphous Carbon Matrix

V. I. Ivanov-Omskiĭ, A. V. Kolobov, A. B. Lodygin^, and S. G. Yastrebov

Ioffe Physicotechnical Institute, Russian Academy of Sciences, St. Petersburg, 194021 Russia

^e-mail: lodygin@mail.ioffe.ru

Submitted May 12, 2004; accepted for publication May 15, 2004

Abstract—Results obtained in a study of electron micrographs of cobalt-doped amorphous hydrogenated carbon are presented. The micrographs were obtained by transmission electron microscopy, including high-resolution electron microscopy. Layers of amorphous carbon were grown by magnetron cosputtering of a graphite and a cobalt target in an atmosphere of argon–hydrogen plasma. It is shown that nanosize crystalline clusters are formed in the process. The influence exerted by 1-h thermal annealing at 800°C in an atmosphere of argon on the size distribution of nanoclusters was studied. It is shown that the distribution function is described by a Gaussian curve that is peaked at ~7 nm for as-grown samples and is strongly broadened upon annealing, with the peak position shifted to larger sizes and the curve exhibiting deviations from the Gaussian shape. A characteristic structure, attributed to nanosize carbon capsules that envelop the clusters, is seen at cluster boundaries in the high-resolution mode. © *2004 MAIK "Nauka/Interperiodica".*

1. INTRODUCTION

Hydrogenated amorphous carbon (*a*-C:H) is of particular interest because of the unique ability of carbon atoms to form various chemical bonding configurations by passing from one state of *sp*-hybridization to another. These properties of *a*-C:H may turn out to be useful in solving the problem of encapsulating metallic nanoclusters into solid media. The importance of this problem is well illustrated by nanostructures based on magnetic metals [1]. In this case, the encapsulation can exert a double influence by protecting the nanoclusters from the aggressive action of the ambient and by weakening the exchange interaction between neighboring particles, which opens up prospects for using nanocomposites as ultrahigh-density magnetic recording media. The fact that *a*-C:H can protect well a metal surface from degradation in corrosive media has been illustrated for such a corrosion-sensitive material as Ag [2].

a-C:H films grown by magnetron cosputtering of carbon and a metal contain nanosize metallic clusters [3]. These clusters appear via self-organization in the course of film growth. The cluster size distribution function reflects the basic features of the nucleation and growth of the clusters [4]. In the present study, the distribution functions were determined by analyzing electron micrographs of cobalt-doped *a*-C:H, i.e., *a*-C:H(Co). The micrographs were obtained by means of transmission electron microscopy (TEM) [5]. An *a*-C:H(Co) film was used for analysis. The film thickness did not exceed 250 nm. The modification of the distribution function in postgrowth treatment was studied upon isothermal annealing of the film in an atmosphere of argon at 800°C for 1 h. According to the data furnished by the Rutherford backscattering method, the concentration of cobalt in the film increases substantially, which is an indication of rapid evaporation of the amorphous carbon matrix. The content of cobalt in the film, found by means of the Rutherford backscattering technique, was ~18 at % for the as-grown film. Upon annealing, the content of cobalt becomes as high as 80 at %, and the film thickness decreases nearly twofold.

2. CLUSTER SIZE DISTRIBUTION FUNCTION AND THE EFFECT OF ANNEALING ON THE FILM STRUCTURE

Figures 1 and 2 show typical TEM micrographs of a film of cobalt-doped amorphous carbon before and after annealing. Figure 3 shows a micrograph of clus-

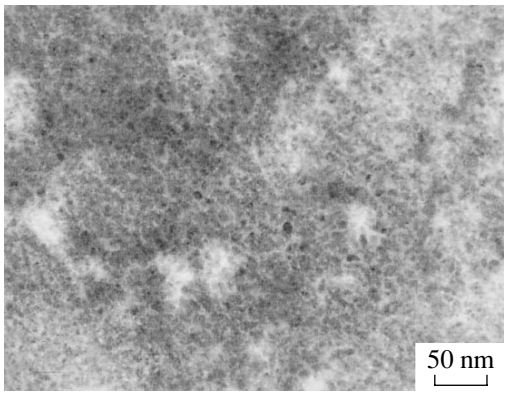

Fig. 1. Electron micrograph of an *a*-C:H(Co) film; fragment dimensions, $0.3 \times 0.5\ \mu m^2$; the dark inclusions are nanosize clusters.

ters upon annealing, which was obtained in the high-resolution mode. The dark inclusions are identified as nanosize clusters of cobalt. A clearly pronounced regular structure can be seen within the clusters, which probably indicates that the clusters are crystalline (Fig. 3).

Because the optical contrast between the dark inclusions and the light background is weak and the cluster boundaries are not clearly pronounced, the image processing is a nontrivial task. In regions with better pronounced clusters, the images were filtered using a method similar to that described in [6]. This made it possible to diminish the background intensity and to reveal more clearly dense objects in the image. Then, the positions of clusters were determined automatically and verified visually. The processing was performed in the dark-field mode with light cluster images, and for this the micrograph in Fig. 1 was inverted. In the calculation, the cluster image was defined as a compact area in the micrograph, whose intensity was at least 50% higher than the background averaged over a square exceeding in size the largest cluster image by a factor of 2–3. The size of this square was determined by visual estimation before the automatic processing. The contour along which the intensity decreased to a preset value (as a rule, 80% of the maximum) was taken as the cluster image boundary. By varying this parameter, the accuracy of the method could be determined, which was very important for constructing the distribution function. The doubled root-mean-square distance from the geometric center of a cluster image to the envelope of its boundary contour was taken as the cluster diameter.

In regions with less clearly pronounced cluster images, the cluster boundaries were also determined by means of expert estimation. In this case, two measurements were made: the linear dimensions of the cluster images were determined along two mutually perpendicular lines passing through the center of mass of a cluster image and then averaged. A comparison of the results of the automatic and manual analyses ruled out the inaccuracy associated with the increased sensitivity of the method used in this study to larger or smaller cluster images and further decreased the error in measuring the cluster image diameter. This error was ~1 nm for unannealed films and ~3 nm for those subjected to annealing (because of the considerably greater size of cluster images in the latter case). The distribution function was defined as the probability density of finding a cluster of a specified size, with the unit cluster represented by a Gaussian curve with a peak position corresponding to the measured cluster diameter and half-width equal to the error of the method. The sought distribution function was found by summing up the probability density functions over all cluster images, with the average number of cluster images in the micrograph being analyzed equal to about 200. The distribution functions constructed in this way were normalized such that the area under a curve was equal to unity (probability density per cluster). This is necessary for comparing the distribution functions obtained for different micrographs.

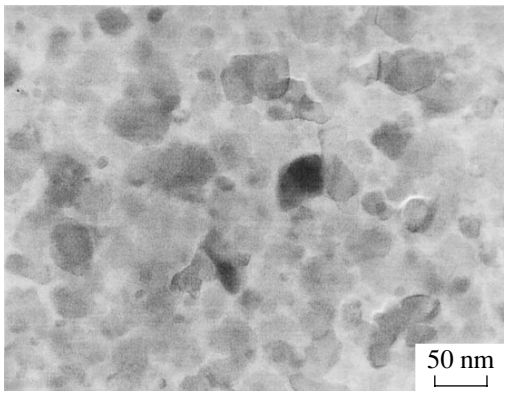

Fig. 2. Electron micrograph of an annealed *a*-C:H(Co) film; fragment dimensions, 0.3×0.5 μm^2; the dark inclusions are nanosize clusters.

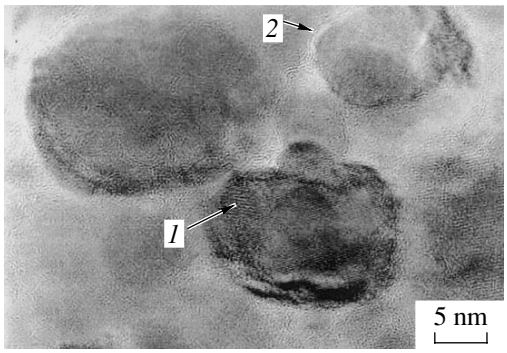

Fig. 3. Large-scale micrograph of an annealed *a*-C:H(Co) film; the arrows show atomic planes (*1*) within and (*2*) outside a cluster.

This technique for obtaining distribution functions is considerably more reliable than the method of histogram drawing frequently used for this purpose, because it is free of the arbitrariness associated with the choice of the width and position of columns in a histogram.

The distribution functions obtained by processing the micrographs in Figs. 1–3 are shown in Fig. 4. The function exhibits a clearly pronounced maximum at a cluster size of ~7 nm. After the annealing, the cluster size increases and the distribution function itself is strongly broadened. The corresponding curve is markedly non-Gaussian in shape.

A bent layered structure can be seen at cluster boundaries (Fig. 3), with an interplanar spacing of ~3 Å, which corresponds to that in graphite and onion-like modifications of carbon [7]. The presence of characteristic structures in the micrographs may be due to the formation of nanosize carbon capsules that envelop crystalline clusters.

Now the distribution functions will be analyzed in terms of a theory that assumes the formation of a new phase [8]. According to this theory, the distribution functions should be described quite well in the initial

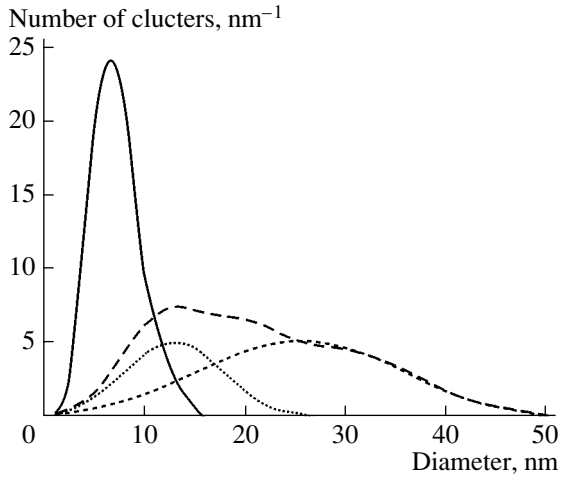

Fig. 4. Size distributions of cobalt clusters: solid line, before annealing; long-dashed line, after annealing. Short-dashed and dotted lines represent the decomposition of the distribution function for an annealed sample into two Gaussian curves.

stages of formation of the crystalline phase by a normal distribution law. To verify this hypothesis, the experimental points for as-grown samples were approximated with a normal distribution law in the form of

$$y = \frac{A}{w\sqrt{\pi/2}}\exp\left[-2\frac{(x-x_c)^2}{w^2}\right].$$

Here, the parameters w, x_c, and A are the half-width of the Gaussian curve, the most probable cluster size, and the amplitude, respectively. Before annealing, the parameters w and x_c are equal to 4.7 and 6.9 nm, respectively. With these parameters, the normal distribution law describes the experimental data for unannealed samples rather well.

After annealing, the distribution function is largely non-Gaussian in shape. However, it can be well approximated with the sum of two Gaussian functions with maxima at around 12 and 26 nm. The reasons why two different sets of clusters are presumably formed in this case remain unclear. It follows from Fig. 4 that the set of coarser clusters contains a larger part of the total cobalt. The parameters w and x_c for this set are 19 and 26 nm, respectively.

The results obtained are in a good agreement with the data of [5], where similar cobalt-containing films were studied by means of EXAFS. It was noted in [5] that the main contribution to the EXAFS spectrum of an unannealed film comes from the C–Co bond, which indicates that cobalt carbide is present in the layers studied. After annealing, the spectra point to the overwhelming predominance of Co–Co bonds. The Co–Co pair-interaction energy is lower than the C–Co pair-interaction energy, and the average cluster size is equal to the ratio between the specific surface and volume energies of cluster formation [8]. Therefore, if it is assumed that, in both cases, compounds of cobalt and carbon are present on the cluster surface, the most probable size of cobalt clusters in annealed samples should exceed the average cluster size before annealing. This is the behavior observed in the experiments performed in the present study.

3. CONCLUSIONS

(1) Crystalline clusters are formed in films grown by magnetron cosputtering of a cobalt and a graphite target. These clusters are several nanometers in size.

(2) Thermal annealing leads to a significant increase in the size of clusters and to a change in their size distribution function. The distribution function for annealed samples is described well by a Gaussian curve on the assumption that two sets of clusters exist with different parameters.

(3) A characteristic layered structure is seen at boundaries between clusters 15–20 nm in size. This structure can be attributed to the formation of nanosize carbon capsules that envelop the crystalline clusters.

ACKNOWLEDGMENTS

This study was supported by the Russian Foundation for Basic Research (grant no. 03-02-16289a).

REFERENCES

1. T. Hayashi, S. Hirono, M. Tomito, and S. Umemura, Nature **381**, 772 (1996).
2. G. A. Dyuzev, V. I. Ivanov-Omskii, E. K. Kuznetsova, *et al.*, Mol. Mater. **8**, 103 (1996).
3. T. N. Vasilevskaya, S. G. Yastrebov, N. S. Andreev, *et al.*, Fiz. Tverd. Tela (St. Petersburg) **41**, 2088 (1999) [Phys. Solid State **41**, 1918 (1999)].
4. S. A. Kukushkin and V. V. Slezov, *Disperse Systems on Solid Surface* (Nauka, St. Petersburg, 1996) [in Russian].
5. A. V. Kolobov, J. Tominaga, T. K. Zvonareva, *et al.*, J. Appl. Phys. **92**, 6195 (2002).
6. V. I. Ivanov-Omskiĭ, A. B. Lodygin, and S. G. Yastrebov, Fiz. Tekh. Poluprovodn. (St. Petersburg) **36**, 797 (2002) [Semiconductors **36**, 743 (2002)].
7. L. C. Qin and S. Iijima, Chem. Phys. Lett. **262**, 252 (1996).
8. L. D. Landau and E. M. Lifshitz, *Course of Theoretical Physics*, Vol. 5: *Statistical Physics*, 4th ed. (Fizmatlit, Moscow, 2001; Pergamon Press, Oxford, 1980), Part 1.

Translated by M. Tagirdzhanov

Semiconductors, Vol. 38, No. 12, 2004, pp. 1419–1425. Translated from Fizika i Tekhnika Poluprovodnikov, Vol. 38, No. 12, 2004, pp. 1466–1472.

PHYSICS OF SEMICONDUCTOR DEVICES

Infrared Light-Emitting Diodes Based on GaInAsSb Solid Solutions Grown from Lead-Containing Solution–Melts

A. P. Astakhova, E. A. Grebenshchikova, É. V. Ivanov, A. N. Imenkov, E. V. Kunitsyna, Ya. A. Parkhomenko^, and Yu. P. Yakovlev

Ioffe Physicotechnical Institute, Russian Academy of Sciences, Politekhnicheskaya ul. 26, St. Petersburg, 194021 Russia

^e-mail: parkhomen@mail.ioffe.ru

Submitted April 21, 2004; accepted for publication April 28, 2004

Abstract—Light-emitting diodes (LEDs) were fabricated on the basis of GaInAsSb alloys grown from lead-containing solution–melts. Electroluminescence characteristics and their current and temperature dependences were studied. The external photon yield at room temperature was 1.6 and 0.11% for LEDs with emission wavelengths $\lambda = 2.3$ and 2.44 μm, respectively. For LEDs with emission wavelength $\lambda = 2.3$ μm, the average emission power $P = 0.94$ mW was attained in the quasi-continuous mode at room temperature. In the pulsed mode, the peak radiation power was $P = 126$ mW at a current of 3 A, a pulse duration of 0.125 μs, and a frequency of 512 Hz. © *2004 MAIK "Nauka/Interperiodica".*

1. INTRODUCTION

The spectral range 1.8–4.0 μm is of considerable interest for laser ranging and location systems [1], radio-frequency atmospheric wireless communications [2], and for medicine and environmental monitoring [3, 4]. GaSb-based GaInAsSb solid solutions are widely used in optoelectronic devices for this spectral range. High-efficiency light-emitting diodes (LEDs) based on such solid solutions, which completely overlap with the range 1.6–2.4 μm, were reported [4]. Increasing the operational wavelength of LEDs based on GaInAsSb solid solutions now remains the most important problem.

We studied the properties of GaInAsSb alloys grown from lead-containing solution–melts previously [5–7]. The use of lead allowed us to grow $Ga_{1-x}In_xAs_ySb_{1-y}$ solid solutions that were lattice-matched to the GaSb (100) substrate at $T = 560$°C. Here, $x = 0.14$–0.27, $y = 0.12$–0.22, and the band gap $E_g = 0.59$–0.49 eV at $T = 300$ K. For a limiting composition with the In content in the solid phase $x = 0.27$, we managed to obtain an epitaxial layer 1.5 μm thick. For all samples, we failed to detect Pb using qualitative X-ray spectral microanalysis. We studied the galvanomagnetic properties of undoped [6], Te-doped [7], and Ge-doped GaInAsSb solid solutions grown from lead-containing solution–melts. We showed that these solid solutions are promising for the development of optoelectronic devices for the spectral range 1.8–3.0 μm.

In this study, we report the fabrication of LED2.3 and LED2.44 LEDs with the wavelength of the peak in the emission spectrum $\lambda = 2.3$ and 2.44 μm. These LEDs are based on GaInAsSb solid solutions grown from lead-containing solution–melts.

2. PROCEDURE FOR FABRICATING AND STUDYING LIGHT-EMITTING DIODE HETEROSTRUCTURES

The LED heterostructures were grown by liquid-phase epitaxy on *n*- and *n*-GaSb (100) substrates. An epitaxial GaSb layer 2.5 μm thick was used as a wide-gap emitter. The energy diagram of the LED heterostructures is shown in Fig. 1a. We calculated equilibrium molar fractions of components in the liquid and solid phases for the Pb–InAs–InSb–GaAs–GaSb sys-

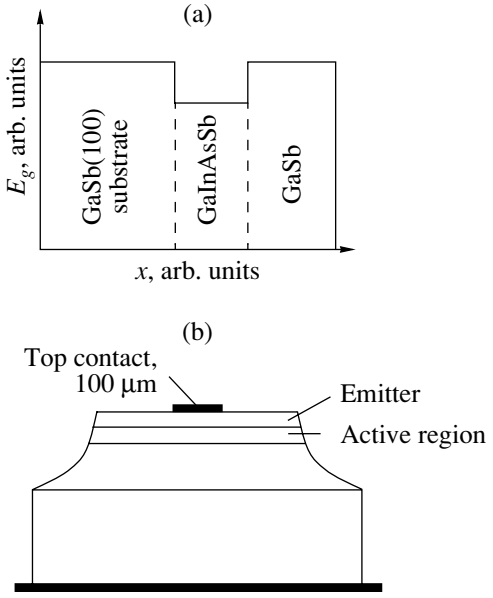

Fig. 1. (a) Energy diagram of the light-emitting diode structures; (b) light-emitting diode design.

1063-7826/04/3812-1419$26.00 © 2004 MAIK "Nauka/Interperiodica"

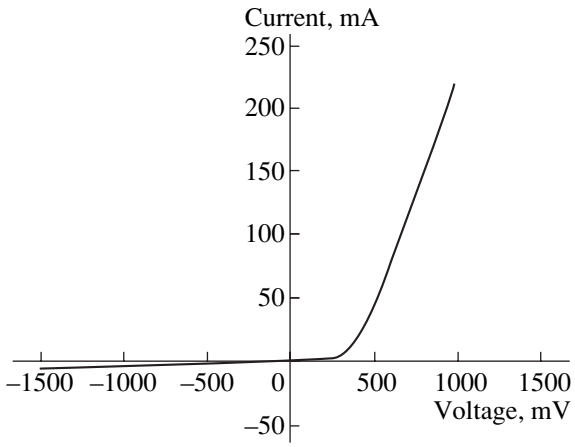

Fig. 2. Current–voltage characteristic of the LED2.3 light-emitting diode at $T = 300$ K, off-duty factor $Q = 2.0$, and frequency $f = 512$ Hz.

tem at a specified temperature (560°C) and supercooling ($\Delta T = 3$ K). For this purpose, we used the Excess Functions–Linear Combinations of Chemical Potentials method [8, 9]. The charge components for the $Ga_{1-x}In_xAs_ySb_{1-y}$ epitaxial layers were In of purity 99.999 wt %, Sb of purity 99.999 wt %, Pb of purity 99.9999 wt %, and the binary compounds GaSb and InAs. According to the X-ray diffraction data, the relative lattice mismatch between the layer and the GaSb substrate ($\Delta a/a$) was no larger than 1.0×10^{-3}.

The LEDs based on GaSb/GaInAsSb/GaSb heterostructures, which were fabricated using the standard lithography technique, were mesa structures of diameter 300 μm. The structures had a continuous contact (Fig. 1b) on the GaSb substrate side and a point contact of diameter 100 μm on the wide-gap GaSb layer side. Nonrectifying contacts to *n*- and *p*-type conductivity materials were formed by vacuum deposition. For this purpose, Cr/Au + Te/Au and Cr/Au + Ge/Au systems were used, respectively. The chips 500×500 μm^2 in size were mounted on standard TO-18 headers.

The spectral characteristics of the LEDs were studied using an automated installation based on a DK-480 monochromator (CVI Laser Corp., United States) and an InSb photodiode (Judson Technologies) cooled with liquid nitrogen. The photodetector signal was processed using the synchronous detection method with an SR 810 selective amplifier (SRS Inc., United States). The measurements were carried out at temperatures $T =$ 300 and 77 K. The LEDs were supplied with a pulsed current; the duration and repetition frequency of pulses were variable.

To study the temperature dependences of electroluminescence characteristics, the LED chips were mounted onto the Peltier thermoelectric cooler located on the TO-5 header.

The external emission quantum yield (η_{ext}) was determined from the current dependence of the optical emission power using the formula

$$\eta_{ext} = \lambda \frac{e}{hc} \frac{P}{I} \times 100\%, \quad (1)$$

where P is the integrated emission power, I is the current, λ is the wavelength, e is the elementary charge, h is Planck's constant, and c is the speed of light.

The spatial distribution of emission intensity of the LEDs was studied using an installation in which the sample was rotated around the axis lying in the *p–n* junction plane. The polar patterns were recorded for two directions of the axis of rotation, namely, parallel to the side opposite facets of the chip and at an angle of 45° to them. The chips were mounted on the TO-18 headers with a flat stage. The measurements were carried out at room temperature. Rectangular current pulses with off-duty factor $Q = 2$ and repetition frequency $f = 523$ Hz were supplied to the LED. As a detector, we used an uncooled PbSe photoresistor with a photosensitive element area of 1×4 mm^2, which was installed at 0.05 m from the LED.

3. LIGHT-EMITTING DIODES WITH EMISSION WAVELENGTH $\lambda = 2.3$ μm

A $Ga_{0.79}In_{0.21}As_{0.16}Sb_{0.84}$ solid solution ($E_g =$ 0.534 eV at $T = 300$ K) 2 μm thick was used as the active layer of the LED structure. The highest efficiency of radiative recombination was attained for LEDs with an undoped active region and Hall hole concentration $p = 3 \times 10^{18}$ cm^{-3} at $T = 300$ K ($p = 4.6 \times 10^{16}$ cm^{-3} at $T = 77$ K). The GaSb emitter layer was Te-doped to the electron concentration $n = (1–4) \times 10^{18}$ cm^{-3} at $T = 300$ K.

The current–voltage (*I–V*) characteristics of the LEDs at $T = 300$ K are shown in Fig. 2. The cutoff voltage for the forward portion of the *I–V* characteristic is 0.4 V, and the calculated series resistance is 2.5 Ω.

The spectral characteristics at $T = 300$ and 77 K, which were recorded on supplying the LEDs with a pulsed current with off-duty factor $Q = 2$ (meander) and frequency $f = 512$ Hz, are shown in Fig. 3.

Figure 3 shows that the emission spectra at $T = 300$ K include a single band with a wavelength corresponding to the intensity peak, $\lambda = 2.29$ μm (the photon energy $h\nu = 0.541$ eV) for current $I = 100$ mA. As the current increases to $I = 220$ mA, the peak of the emission spectrum shifts to longer wavelengths by $\Delta\lambda = 0.02$ μm. This shift is accompanied by a variation in the full-width at half-maximum (FWHM) of the emission band from 0.20 to 0.23 μm. These data indicate that the current-induced heating of the structure affects electroluminescence characteristics only slightly.

On cooling to $T = 77$ K, the peak of the emission spectrum shifts by $\Delta\lambda = 0.24$ μm to shorter wavelengths, and the wavelength is $\lambda = 2.05$ μm ($h\nu = 0.605$ eV),

which corresponds to the band gap of the active region E_g(77 K) = 0.608 eV. As the current increases from 50 to 200 mA, the spectral peak position remains unchanged. The FWHM for a current of 200 mA is 0.1 μm.

The temperature coefficient of variation in the spectral peak wavelength is $\Delta\lambda/\Delta T$ = 1.5 nm/K, which is consistent with the temperature coefficient of the band gap variation. The emission intensity decreases by a factor of e as the temperature increases by 110°C in the temperature range 0–120°C.

The directivity diagram of the LED emission (Fig. 4) shows that the intensity is peaked at angles of deviation from the normal to the plane of the outer face facet $\theta = \theta_{max} = \pm 31°$. At average angles of deviation in the plane parallel to side facets, the peak intensity of emission is lower than in the plane including the diagonal of the epitaxial layer of the LED chip. For this design, the LED emits through both the face facet and the side facets of the crystal. The emission intensity at the diagram center is mainly governed by the emission escape through the face facet of the crystal normally to the p–n junction plane. Let us denote this plane as $P_\perp$. At nonzero angles, the emission through side facets is added to the emission through the face facet. When the axis of revolution lying in the p–n junction plane is parallel to two opposite side facets and normal to two other facets, the escape of emission only through one side facet is added. When the axis of revolution is directed at an angle of 45° to the side facets, the escape of emission from two side facets is added. Therefore, the emission intensity is higher in the diagonal direction. The analysis of the shape of the directivity diagram shows that the distribution of emission through each facet is close to a cosine distribution. This finding allows us to determine the effective emission intensity normally to the side facet: $P_\parallel = P_\perp \tan\theta_{max}$. The emission intensity at an angle of deviation from the normal to the face facet of $\theta = 90°$ is lower than $P_\parallel$ mainly because of the restricted header area reflecting the emission. Because the front facet emits into the half-space, while the side facet emits only into the quarter-space, the total intensity P_Σ is proportional to $(P_\perp + 2P_\parallel)$. The LEDs under consideration with $\theta_{max} = \pm 31°$ emit through the four side facets at a 20% higher intensity than through the face facet.

Figure 5 shows the current dependence of the integrated optical power of the LED. In a quasi-continuous mode (Q = 2) (see Fig. 5, inset), the highest power P = 0.94 mW is attained at a current of I = 220 mA. For currents I < 50 mA, the $P(I)$ dependence is superlinear. In the current range 50–200 mA, the dependence is almost linear, which indicates that the heating of the active regions of the LEDs by the current is insignificant. The extrapolation of a linear portion of the $P(I)$ dependence to the zero value of power yields the cutoff current I_{cut} = 20 mA. For currents I > 200 mA, the measurements were carried out in the pulsed mode with pulse duration τ = 0.125, 2, or 32 μs. The $P(I)$ dependence is almost linear up to $I \approx 2.5$ A at τ = 0.125 and 2 μs and up to $I \approx 1$ A at τ = 32 μs. The dependence then becomes sublinear for all τ. One can see that a decrease in the pulse duration lengthens the straight-line portion of the $P(I)$ dependence. The highest peak power of emission P = 126 mW is attained at I = 3 A, pulse duration τ = 0.125 μs, and frequency f = 512 Hz.

The external quantum yield of emission for the LEDs studied at room temperature is $\eta_{ext} \approx 1.6\%$ at a current I = 220 mA. The differential external photon yield is highest at a current of I = 100 mA and is equal to η_{ed} = 2%.

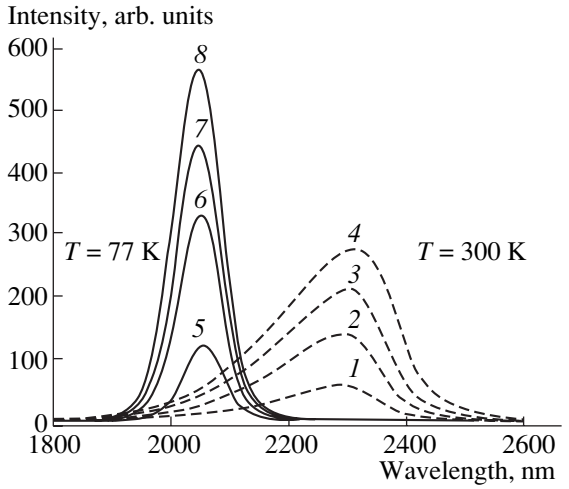

Fig. 3. Electroluminescence spectra of the LED2.3 light-emitting diodes. (*1*–*4*) T = 300 K, pumping current: (*1*) 50, (*2*) 100, (*3*) 150, and (*4*) 220 mA; (*5*–*8*) T = 77 K, pumping current: (*5*) 50, (*6*) 100, (*7*) 150, and (*8*) 200 mA.

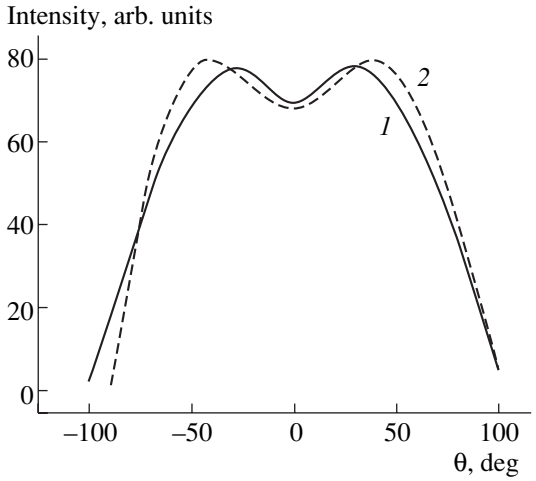

Fig. 4. Directivity diagram of emission of the LED2.3 light-emitting diodes in the plane normal to the p–n junction plane: (*1*) plane is parallel to side facets of the light-emitting diode; (*2*) plane includes the diagonal of the light-emitting diode chip in the p–n junction plane.

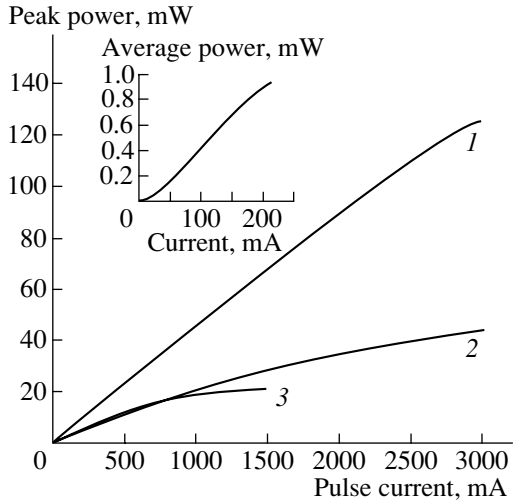

Fig. 5. Current dependence of the peak optical power of the LED2.3 light-emitting diode at frequency $f = 512$ Hz and pulse duration τ = (*1*) 0.125, (*2*) 2, and (*3*) 32 μs. Inset: current dependence of the average optical power of the light-emitting diode for off-duty factor $Q = 2$ and frequency $f = 512$ Hz.

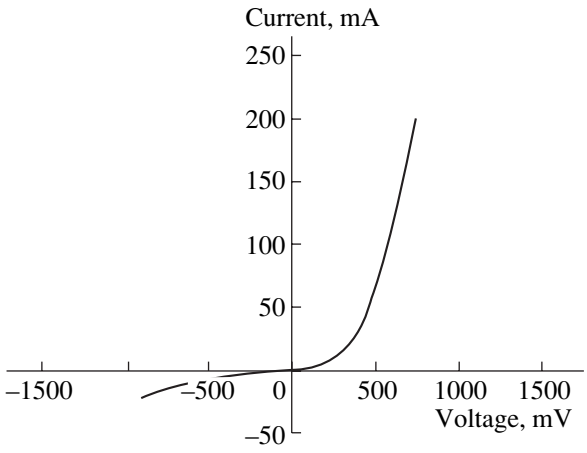

Fig. 6. Current–voltage characteristic of the LED2.44 light-emitting diode at $T = 300$ K, off-duty factor $Q = 2$, and frequency $f = 512$ Hz.

4. LIGHT-EMITTING DIODES WITH EMISSION WAVELENGTH $\lambda = 2.44$ μm

We used the 1.2-μm-thick Te-doped $Ga_{0.75}In_{0.25}As_{0.22}Sb_{0.78}$ solid solution ($E_g = 0.506$ eV at $T = 300$ K) with electron concentration $n = 3 \times 10^{18}$ cm^{-3} as the active layer of the LED structure. As the wide-gap emitter, we used the Ge-doped GaSb epitaxial layer with hole concentration $p \approx 5 \times 10^{18}$ cm^{-3}.

The LED *I–V* characteristic shown in Fig. 6 is of the diode type with a cutoff voltage of 0.4 V (at $T = 300$ K) and a series resistance of 1.7 Ω with a forward bias.

The spectral characteristics of the LED emission with a pulsed current with off-duty factor $Q = 2$ (meander) and repetition rate $f = 512$ Hz at $T = 300$ and 77 K

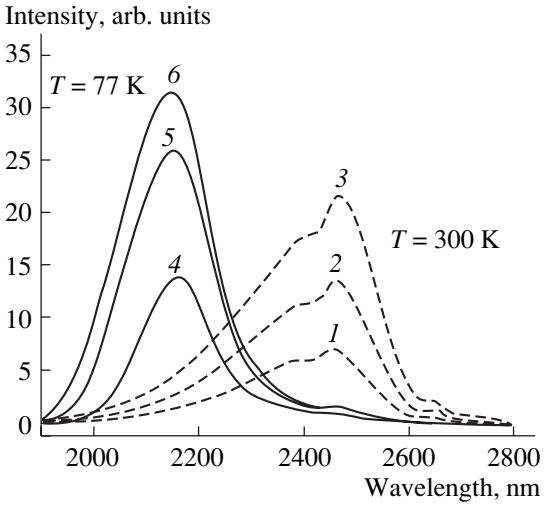

Fig. 7. Electroluminescence spectra of the LED2.44 light-emitting diodes. (*1–3*) $T = 300$ K, pumping current: (*1*) 100, (*2*) 150, and (*3*) 220 mA; (*4–6*) $T = 77$ K, pumping current: (*4*) 100, (*5*) 150, and (*6*) 200 mA.

are shown in Fig. 7. Figure 7 shows that the electroluminescence spectrum at $T = 300$ K is peaked at the wavelength $\lambda = 2.44$ μm, which corresponds to $h\nu = 0.508$ eV. This value is somewhat larger than the calculated band gap of the material of the active region, $E_g = 0.506$ eV. The peak has an FWHM of ~0.26 μm at a current of $I = 100$ mA.

As the current is varied from 50 to 200 mA, the position of the spectral peak of the LED emission remains unchanged. In this case, the FWHM also remains unchanged, which indicates that the heating of the structure under flowing current is insignificant at a low excitation level. The observed valley in the electroluminescence spectrum of the LED at $\lambda \approx 2.42$ μm is caused by the specific features of the spectral characteristic of the diffraction grating used (300 grooves/mm). In addition, intense absorption lines of water and carbon dioxide are present in the wavelength range 2.60–2.72 μm.

At $T = 77$ K, the peak wavelength of the emission spectrum decreases with increasing current from $\lambda = 2.18$ μm ($h\nu = 0.569$ eV) at current $I = 50$ mA to $\lambda = 2.14$ μm ($h\nu = 0.579$ eV) at current $I = 200$ mA. In this case, the FWHM of the spectral band also increases from ~0.14 to 0.20 μm. An increase in the peak photon energy of the LED electroluminescence spectrum and the spectral-band broadening indicates a high excitation level of the active region at $T = 77$ K.

In the pulsed supply mode ($\tau = 2$ μs, $f = 512$ Hz), the wavelength of the emission-band peak decreases from $\lambda = 2.41$ μm ($h\nu = 0.515$ eV) to $\lambda = 2.39$ μm ($h\nu = 0.519$ eV) as the current is varied from 0.5 to 3.0 A. In this case, the FWHM of the spectral band increases from 0.28 to 0.36 μm. This increase is attributed to the fact that the excitation level at room temperature is also high.

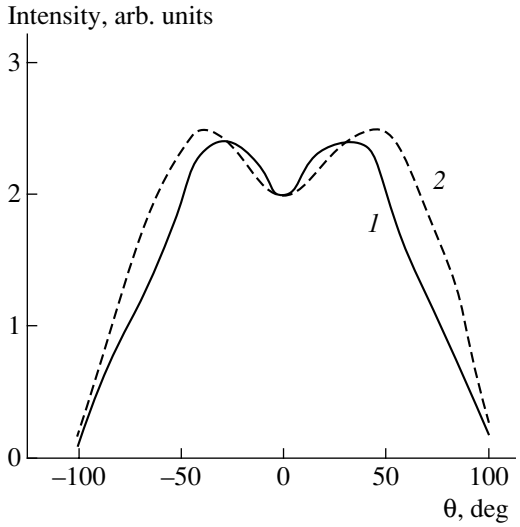

Fig. 8. Directivity diagram of emission of the LED2.44 light-emitting diodes in the plane normal to the *p–n* junction plane: (*1*) plane is parallel to side facets of the light-emitting diode; (*2*) plane includes the diagonal of the light-emitting diode chip in the *p–n* junction plane.

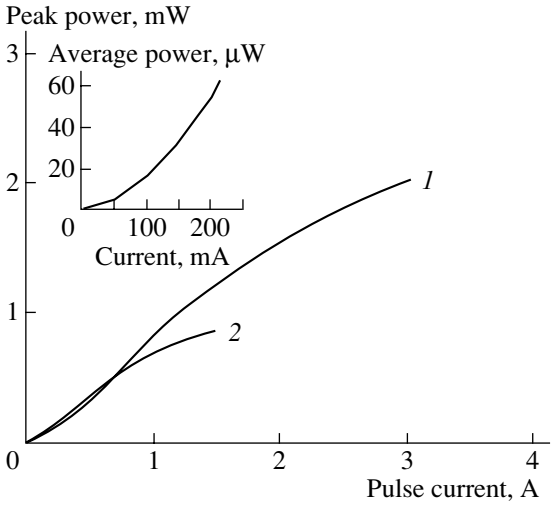

Fig. 9. Current dependence of the peak optical power of the LED2.44 light-emitting diode at frequency f = 512 Hz and pulse duration τ = (*1*) 2 and (*2*) 32 μs. Inset: current dependence of the average optical power of the light-emitting diode for off-duty factor Q = 2 and frequency f = 512 Hz.

The directivity diagram of this LED is shown in Fig. 8. We can see that the emission intensity has low peaks at angles of deviation $\theta_{max} = \pm 40°$ in the plane parallel to two opposite side facets and $\theta_{max} = \pm 45°$ in the plane located at an angle of 45° to them. The ratio of intensities of light emitted through the four side facets and the face facet, which is found from the peak angle, is $2\tan\theta_{max} = 2\tan 40° = 1.68$. Thus, the intensity of light emitted through the side facets is 68% higher than that emitted through the face facet.

In a quasi-continuous mode (Q = 2, Fig. 9, inset), the current dependence of the LED emission power is superlinear up to I = 50 mA and further increases linearly up to I = 200 mA. In the pulsed mode (Fig. 9), the dependence $P(I)$ at τ = 2 μs is close to linear up to $I \approx 1$ A. In the current range 1–3 A, the dependence is weakly sublinear. For the pulse duration τ = 32 μs, the sublinearity is clearly pronounced apparently due to the heating of the active region during the pulse passage.

The highest average optical power is 62 μW at current I = 218 mA. In this case, the external photon yield at room temperature equals $\eta_{ext} \approx 0.11\%$. The highest differential external photon yield $\eta_{ed} = 0.17\%$ corresponds to a current of 600 mA.

The highest peak emission power in the pulsed mode P = 2 mW was attained at current I = 3 A, pulse duration τ = 2 μs, and frequency f = 512 Hz.

5. RESULTS AND DISCUSSION

The emission spectra of the LEDs with an emission wavelength of 2.3 μm have the main features of band-to-band radiative recombination. These features are the following. (i) The peak photon energy slightly exceeds ($\sim k_BT$) the band gap of the narrow-gap layer. (ii) The spectral peak energy is independent of current at small currents, which corresponds to a low excitation level. However, this energy slightly increases with current at large currents, when a high excitation level is attained. (iii) The width of the spectral emission band is $(1.5–2)k_BT$, and this magnitude slightly increases with current at high excitation levels. We may conclude that the radiative recombination is caused by electron injection into the narrow-gap *p*-type layer and by electron–hole recombination in this layer due to band-to-band electron transitions.

The superlinearity of the current dependence of the emission power at $I < 20$ mA is most probably associated with deep levels of nonradiative recombination in the narrow-gap layer; these levels are also present in the GaSb layers. For currents exceeding the cutoff current (I_{cut} = 20 mA), the levels are saturated, and the corresponding current remains equal to the cutoff current. The ohmic leakage currents estimated from the reverse portion of the *I–V* characteristic are an order of magnitude smaller.

Thus, for currents exceeding the cutoff current, the predominant recombination mechanism is the band-to-band recombination. This may be not only radiative recombination, since the differential internal photon yield in the region of large currents is equal to the photon yield for band-to-band transitions.

When estimating the internal quantum yield, we will assume that emission is generated in the narrow-gap layer, where reemission is possible. The volume of the narrow-gap layer is only 0.28% of the total volume of

the structure, while the coefficient of photoinactive absorption α_d is on average ~10 cm^{-1}. Therefore, only the photons with energy exceeding the band gap of the narrow-gap material by 45 meV or more will be mainly absorbed during photoactive band-to-band transitions. The fraction of these short-wavelength photons is 1/4 of all initially emitted photons. In the LEDs under study, there are factors that give rise to emission nondirectivity. These factors are the surface roughness of the substrate and the steps at the side surface of the mesas, which scatter the emission during reflection. Therefore, formula (4) from [10] is applicable in this case. This formula relates the external photon yield η_{ext} to the internal quantum yield of long-wavelength photons η_l and short-wavelength photons η_s, as well as to the coefficients of photoinactive absorption α_d and effective absorption caused by the escape of emission from the crystal α_e. The latter can be found from formula (6) [10]:

$$\alpha_e = \frac{S}{Vn(n+1)^2}, \quad (2)$$

where S is the area of a free light-emitting surface, V is the crystal volume, and n is the refractive index.

Let us expand the formula for η_{ext} relative to η_l:

$$\eta_l = \left[k + \eta_{ext}^{-1}\left(1 + \frac{\alpha_d}{\alpha_e}\right)^{-1}\right]^{-1}, \quad (3)$$

where $k = \eta_s/\eta_l$.

In our case, $k = 1/3$, $\alpha_e = 1.48$ cm^{-1}, and $\alpha_d = 10$ cm^{-1}.

For $\eta_{ext} = 1.6\%$, we find $\eta_l = 12\%$, $\eta_s = 4\%$, and the total internal photon yield $\eta_{int} = \eta_l + \eta_s = 16\%$.

To determine the emission quantum yield for the band-to-band emission, let us use the differential external photon yield $\eta_{ed} = 2\%$ instead of η_{ext}. In this case, the internal quantum yield of long-wavelength photons $\eta_{ld} = 15\%$, of the short-wavelength photons $\eta_{sd} = 5\%$, and the total quantum yield for the band-to-band emission $\eta_d = 20\%$. It then follows that 80% of band-to-band transitions are nonradiative. Since the values of the band gap and the spin–orbit splitting energy are almost the same, the Auger process is most probable in the *p*-type material due to electron transfer from the conduction band into the valence band and hole transfer from the valence band to the spin–orbit split-off band (the CHHS process). The rate of this process depends on the excitation level in almost the same way as the rate of radiative recombination. This fact explains the linearity of the current dependence of the emission intensity.

The emission spectra of the LEDs with peak wavelength $\lambda = 2.44$ μm exhibit the same indications of band-to-band recombination as the spectra of LEDs with $\lambda = 2.3$ μm. However, the width of the spectral emission band for these LEDs is $2k_BT$ at $I < 200$ mA, and it increases noticeably at large currents, attaining $3k_BT$ at current $I = 3$ A. This behavior is caused by the electron conduction in the active narrow-gap region, in which the electrons are degenerate even for small currents due to the small effective mass of these electrons. The degree of degeneracy increases with current due to the small thickness of the narrow-gap region. The peak energy of the spectral band slightly increases with current as one would expect for a case of band-to-band recombination for a low excitation level. For the impurity recombination, the peak energy is independent of current, and this mechanism can be disregarded. In the case of considerable involvement of band "tails" or in the case of diagonal tunneling, the peak energy of the spectral band should increase more sharply for small currents than for large ones. Since we observe a reverse pattern, these recombination mechanisms may also be considered insignificant. Thus, we may conclude that the emission is caused by band-to-band recombination.

Most of the emission is apparently adsorbed in the active region, since the width of the emission spectral band is less than the theoretically calculated one at a specified level of electron degeneracy by a factor of 3. The fraction of long-wavelength photons in the primary emission is ~20%, which corresponds to the value $k = \eta_s/\eta_l = 4$.

The magnitudes of internal photon yield determined by formula (2) at $k = 4$, $\alpha_e = 1.48$ cm^{-1}, $\alpha_d = 20$ cm^{-1}, and $\eta_{ext} = 0.11\%$ are $\eta_l = 1.52\%$, $\eta_s = 6\%$, and $\eta_{int} = 7.5\%$. By substituting the differential external photon yield $\eta_{ed} = 0.17\%$ for η_{ext}, we find $\eta_{ld} = 2.2\%$, $\eta_{sd} = 9\%$, and $\eta_d = 11.2\%$. Thus, about 90% of the band-to-band recombination is nonradiative. In this case, CHCC Auger recombination is most probable. This recombination is characteristic of *n*-type semiconductors. In this process, one electron from the conduction band transfers to the valence band, while the second electron participates in the intraband transition. Thus, the almost linear current dependence of the emission power is retained.

6. CONCLUSIONS

The light-emitting diodes (LEDs) with spectral peak wavelengths $\lambda = 2.3$ and 2.44 μm were fabricated on the basis of GaInAsSb solid solutions grown from lead-containing solution–melts. The external photon yield at room temperature was 1.6 and 0.11%, respectively. These LEDs may find wide application in systems for environmental monitoring and medical diagnostics.

ACKNOWLEDGMENTS

We thank N.V. Vlasenko, E.V. Kuznetsova, and M.Yu. Putilovskaya for deposition of the contacts, mounting the samples, and measuring the *I–V* characteristics.

REFERENCES

1. R. J. Becherer, Suppl. Laser Focus World, May, 71 (1993).
2. K. Kincade, Suppl. Laser Focus World, December, 69 (2003).
3. T. L. Troy and S. N. Thennadil, J. Biomed. Opt. **6** (2), 167 (2001).
4. N. D. Stoyanov, B. E. Zhurtanov, A. P. Astakhova, *et al.*, Fiz. Tekh. Poluprovodn. (St. Petersburg) **37**, 996 (2003) [Semiconductors **37**, 971 (2003)].
5. I. A. Andreev, E. V. Kunitsyna, Yu. V. Solov'ev, *et al.*, Pis'ma Zh. Tekh. Fiz. **25** (19), 77 (1999) [Tech. Phys. Lett. **25**, 792 (1999)].
6. T. I. Voronina, T. S. Lagunova, E. V. Kunitsyna, *et al.*, Fiz. Tekh. Poluprovodn. (St. Petersburg) **35**, 941 (2001) [Semiconductors **35**, 904 (2001)].
7. T. I. Voronina, T. S. Lagunova, E. V. Kunitsyna, *et al.*, Fiz. Tekh. Poluprovodn. (St. Petersburg) **36**, 917 (2002) [Semiconductors **36**, 855 (2002)].
8. A. M. Litvak and A. N. Charykov, Zh. Fiz. Khim. **64**, 2331 (1990).
9. N. A. Charykov, V. V. Sherstnev, and A. Krier, J. Cryst. Growth **234**, 762 (2002).
10. E. A. Grebenshchikova, A. N. Imenkov, B. E. Zhurtanov, *et al.*, Fiz. Tekh. Poluprovodn. (St. Petersburg) **38**, 745 (2004) [Semiconductors **38**, 717 (2004)].

Translated by N. Korovin

Semiconductors, Vol. 38, No. 12, 2004, pp. 1426–1429. Translated from Fizika i Tekhnika Poluprovodnikov, Vol. 38, No. 12, 2004, pp. 1473–1476.

PHYSICS OF SEMICONDUCTOR DEVICES

Luminescence Properties of Cylindrical ZnO Microcavities

A. N. Gruzintsev^, V. T. Volkov, S. V. Dubonos, M. A. Knyazev, and E. E. Yakimov

Institute of Microelectronic Technology and Ultra-High-Purity Materials, Russian Academy of Sciences, Chernogolovka, Moscow oblast, 142432 Russia

^e-mail: gran@ipmt-hpm.ac.ru

Submitted April 21, 2004; accepted for publication April 28, 2004

Abstract—Luminescence properties of thin-film cylindrical ZnO microcavities 1.8 μm in diameter obtained by electron-beam lithography and reactive ion etching were studied. Narrow luminescence peaks were detected in the excitonic and green spectral regions of zinc oxide and were attributed to spatial quantization of photon wave functions. It was found that stimulated ultraviolet luminescence arises with coupled photon modes of microcavities as optical pump power increases. *© 2004 MAIK "Nauka/Interperiodica".*

1. INTRODUCTION

Recently, the wide-gap semiconductor ZnO (band gap E_g = 3.37 eV) has been intensively studied due to the prospects for developing short-wavelength semiconductor laser diodes based on it. Due to the high exciton binding energy (60 meV) in zinc oxide, it became possible to attain stimulated luminescence in bulk single crystals [1, 2] and epitaxial films [3, 4] not only at cryogenic temperatures, but also at room temperature. Depending on the crystal structure and defect composition in zinc oxide films, recombination emission of excitons arises with a photon energy of 3.28 eV (at temperature T = 300 K) or green luminescence with a peak at 2.3 eV, caused by intrinsic defects (oxygen vacancies). The high crystalline quality of ZnO epitaxial films results in the fact that the luminescence spectrum only contains an excitonic peak up to 550 K [3].

We obtained laser radiation with a wavelength of 397 nm in [5] using polycrystalline nonepitaxial ZnO films produced by magnetron-sputtering deposition onto oxidized silicon substrates. Stimulated room-temperature luminescence was observed in the range of electron–hole plasma recombination under optical excitation by a pulsed nitrogen laser. In this case, the threshold pump power was rather high, 6 MW/cm^2. Such a large value is caused not only by the fact that the film is polycrystalline, but also by the absence of feedback along the film for stimulated light photons. The Fabry–Perot cavity exists with total internal reflection at the upper and lower faces of the film and single-pass lasing in the horizontal plane. To decrease the lasing threshold, it is advisable to fabricate cavities with mirrors on the lateral faces of the structure, which requires flat cleaved surfaces of optical quality.

However, there is an alternative technological method for fabricating cavities with a high quality factor for semiconductor lasers used in this study. The point here is that a multiple-pass pulsed lasing mode can develop only in micrometer-size cavities due to the short lifetime (10 ps) of excited excitonic states of a semiconductor medium. Recently [6, 7], it was suggested that coupled or weakly coupled quantum modes of three-dimensional (3D) photon dots be used to attain lasing in semiconductor lasers. In that case, a semiconductor shaped like a parallelepiped, cylinder, or sphere with size on the order of the wavelength of light that is placed into a transparent medium with a smaller refractive index has several coupled states, i.e., emitted light modes. The mode lifetime controls the quality factor of the microcavity and optical pump threshold for stimulated emission.

In this study, we consider the effect of spatial quantization of photon wave functions in cylindrical ZnO microcavities 1.8 μm in diameter on the spectral shape of excitonic and green luminescence lines, as well as on the initiation of stimulated emission during optical pulsed excitation.

2. EXPERIMENTAL

We used zinc oxide films 0.25 μm thick deposited by magnetron sputtering on oxidized silicon substrates. The thermal oxide thickness was 0.27 μm. Immediately after magnetron-sputtering deposition, the zinc oxide films had an amorphous structure and exhibited no luminescence. However, as a result of annealing in an oxygen atmosphere at 700°C for a few minutes, the films crystallized with the formation of crystalline grains with average sizes of ~0.3–0.5 μm. The film surface remained optically smooth with an average roughness of ~10 nm. An excitonic peak with a maximum at 3.28 eV was predominant in the luminescence spectrum of annealed films at room temperature. Lasing was observed when pumping by a pulsed nitrogen laser was used at a threshold pump power of 6 MW/cm^2 [5].

Thin-film cylindrical ZnO microcavities 1.8 μm in diameter were obtained by electron-beam lithography and reactive ion etching in argon plasma using prelim-

inarily annealed Si–SiO_2–ZnO structures. An aluminum mask used during ion etching was then removed using a diluted alkali solution. Ion etching made it possible to obtain vertical walls of cylindrical microcavities arranged as a chain with a distance between nearby cylinders of 10 μm (see Figs. 1, 2). A film area of ~4 mm^2 was intentionally not subjected to lithography; it remained as an island and was treated in the same way as cylindrical microcavities. This was done to determine the influence of size effects on luminescence spectra, rather than the influence of changes caused by plasma or electrochemical treatment. Thus, linear arrays of cylindrical photon dots 1.8 μm in diameter were produced. Figures 1 and 2 show the electron-microscopy images of a single microcavity (side view, 1.8 μm in diameter) and an array of 11 microcavities (top view 1). A set of arrays of identical microcavities was formed to increase the intensity of the luminescence signal in optical measurements.

The luminescence spectra were measured under excitation by an ILGI-505 pulsed nitrogen laser with a wavelength of 337.1 nm, a pulse duration of 9 ns, and a peak power of 1.5 kW. The laser beam was focused onto a spot 0.5 mm in diameter, which provided an optical excitation density as high as $I_0 = 0.4$ MW/cm^2. The photoluminescence (PL) spectra of microcavities of various diameters were studied at room temperature and various pump powers, $I = 0.1I_0$, $0.15I_0$, $0.5I_0$, $0.75I_0$, and $1I_0$. To this end, a light absorber with a preset transmittance was placed between the sample and the laser. The excitation light of the laser was incident on the microcavity normally to its surface. Luminescence was measured at an angle of 45°, which decreased the contribution of reflected laser light. Luminescence was measured using an MDR-23 monochromator, an FÉU-106 photomultiplier, and a Unipan-237 variable-signal amplifier connected to a computer. The spectral resolution was no worse than 0.2 nm in all the experiments.

3. RESULTS AND DISCUSSION

Figure 3 shows the PL spectra of cylindrical ZnO microcavities 1.8 μm in diameter (curve *1*) and the island film (curve *2*) for the lowest power $I = 0.1I_0$ of excitation radiation. It is worth noting that both spectra contain a green-emission band peaked at about 2.2 eV and caused by oxygen vacancies in zinc oxide [8]. Excitonic luminescence is almost absent at low-intensity pumping. We note that the intensity of green PL of microcavities (curve *1*) is somewhat higher than that of the island film (curve *2*) and has a pronounced fine structure with two peaks at 2.03 and 2.22 eV, as well as two shoulders on the short-wavelength side at energies of 2.43 and 2.61 eV.

As the excitation-radiation intensity increases to $I_0 = 0.4$ MW/cm^2 (Fig. 4), excitonic luminescence with a peak in the violet spectral region at 3.28 eV begins to prevail in the PL spectra. In this case, the shape and

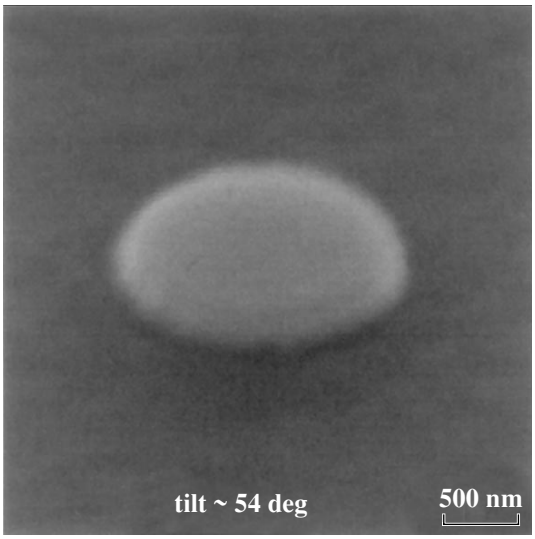

Fig. 1. Electron-microscopy image of the cylindrical ZnO microcavity 1.8 μm in diameter, obtained at an angle of 45°.

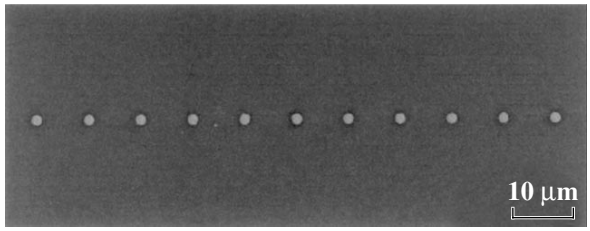

Fig. 2. Electron-microscopy image (top view) of an array of ZnO microcavities 1.8 μm in diameter (top view).

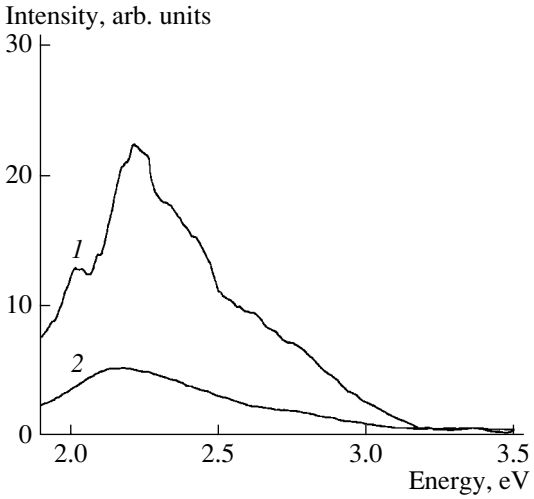

Fig. 3. Photoluminescence spectra excited using a nitrogen laser with power density $I = 0.1I_0$ of (*1*) the linear array of microcavities 1.8 μm in diameter and (*2*) the ZnO film grown on oxidized silicon; $T = 300$ K, $I_0 = 0.4$ MW/cm^2.

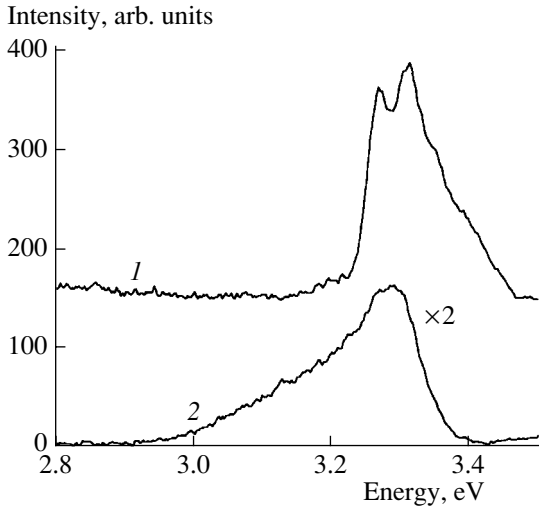

Fig. 4. Photoluminescence spectra (excited by the nitrogen laser with power density $I = I_0$) of (*1*) the linear array of microcavities 1.8 μm in diameter and (*2*) the ZnO film grown on oxidized silicon; $T = 300$ K, $I_0 = 0.4$ MW/cm^2.

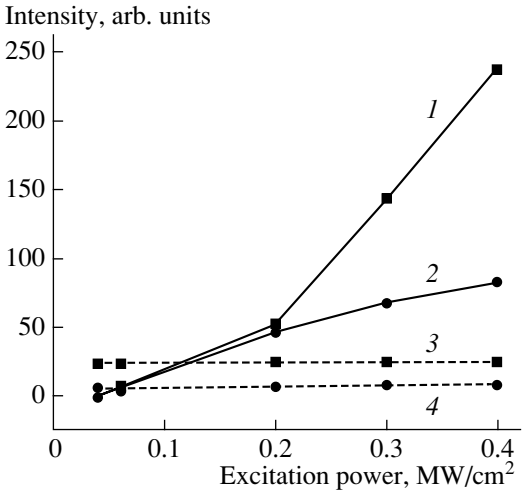

Fig. 5. Dependences of the intensity of the mode with the highest intensity in the excitonic region of (*1*) microcavities 1.8 μm in diameter and (*2*) ZnO film, as well as in the green region of (*3*) microcavities and (*4*) ZnO film, on the power density of the excitation laser radiation; $T = 300$ K.

intensity of green-emission bands is almost unchanged (Fig. 5). In contrast to the island ZnO film (Fig. 4, curve *2*), the spectra of excitonic PL of microcavities (curve *1*) are significantly narrower and have a fine structure, which is caused by coupled and weakly coupled modes of 3D photon dots with peak positions at 3.26, 3.31, 3.35, and 3.38 eV. Uncoupled modes in fact represent interference of outgoing light at microcavity lateral faces, while coupled photon states should be completely localized inside it. However, due to scattering at polycrystal boundaries inside the film, even coupled electromagnetic oscillations sooner or later leave the film and contribute to the PL signal. Therefore, the microcavities under consideration, like any laser cavities, exhibit a finite quality factor that controls the width of the emission line. We can see in Fig. 4 that the FWHM of the line corresponding to the single most intense mode (with a peak at 3.31 eV) of the cavity 1.8 μm in diameter (curve *1*) is ~25 meV in the case under consideration. Is this quality factor sufficiently large for the generation of lasing pumped by pulses of the nitrogen laser?

Figure 5 shows the dependence of the intensity of the brightest mode at 3.31 eV in the excitonic spectral region of this microcavity on the power density of excitation radiation of the nitrogen laser. We note the almost linear dependence for the island ZnO film (curve *2*). For microcavities 1.8 μm in diameter (curve *1*), the luminescence intensity evidently increases nonlinearly, which suggests that stimulated luminescence arises if the power density of laser excitation is higher than 0.2 MW/cm^2. This is in agreement with the dependence of the intensity of green-emission bands of the microcavities and ZnO film on the pump power (Fig. 5, curves *3*, *4*). The point here is that the green PL intensity of the film slightly increases, while that of cavities even slightly decreases with the excitation-radiation power. This observation confirms that lasing arises in the excitonic spectral region of microcavities. In this case, the excitonic line becomes narrower in comparison with the film spectrum, which is especially distinct in the long-wavelength spectral region, where phonon replicas of the excitonic line are observed.

The use of coupled modes of small microcavities reduces the threshold powers of optical pumping needed for lasing. Specifically, the use of cylinders with diameters from 1 to 3 μm makes it possible to obtain ZnO microcavities (using the technology under discussion) with the highest quality factor for generating violet radiation with a peak at 3.31 eV (Fig. 4, curve *1*). Note that the dependence of the intensity of excitonic luminescence of simple ZnO films used to obtain microcavities, which we studied in [5], was linear up to a power of 6 MW/cm^2.

4. CONCLUSIONS

Thus, optical cylindrical microcavities 1.8 μm in diameter were obtained by electron-beam lithography and ion etching on the Si–SiO_2–ZnO structure with a thin zinc oxide film (0.25 μm). The mode structure of photoluminescence spectra was experimentally detected in the excitonic and green spectral regions of ZnO microcylinders.

The study of photoluminescence spectra of microcavities in relation to the optical pump intensity showed stimulated emission in the excitonic region of zinc oxide at an excitation-power density higher than 0.2 MW/cm^2. Note also that stimulated emission of the ZnO film itself required an excitation density of 6 MW/cm^2 [5].

Hence, the use of three-dimensional cavities with cylinders 1.8 μm in diameter allows the pump threshold to be decreased more than tenfold compared with the one-dimensional Si–SiO_2–ZnO cavity structure of the Fabry–Perot type.

ACKNOWLEDGMENTS

This study was supported by the Russian Foundation for Basic Research (project no. 04-02-16437), the "Quantum Calculations" program of the Russian Academy of Sciences, and INTAS (grant no. 2002-0796).

REFERENCES

1. J. M. Hvam, Phys. Rev. B **4**, 4459 (1971).
2. C. Klingshirn, Adv. Mater. Opt. Electron. **3**, 103 (1994).
3. D. M. Bagnall, Y. F. Chen, M. Y. Shen, *et al.*, J. Cryst. Growth **184–185**, 605 (1998).
4. Z. K. Tang, G. K. Wong, P. Yu, *et al.*, Appl. Phys. Lett. **72**, 3270 (1998).
5. A. N. Gruzintsev, V. T. Volkov, C. Barthou, and P. Benalloul, Fiz. Tekh. Poluprovodn. (St. Petersburg) **36**, 741 (2002) [Semiconductors **36**, 701 (2002)].
6. M. Obert, B. Wild, G. Bacher, *et al.*, Phys. Status Solidi A **190**, 357 (2002).
7. T. Gutbrod, M. Bayer, A. Forhel, and J. P. Reithmaier, Phys. Rev. B **57**, 9950 (1998).
8. H. S. Kang, J. S. Kang, J. W. Kim, and S. Y. Lee, J. Appl. Phys. **95**, 1246 (2004).

Translated by A. Kazantsev

Semiconductors, Vol. 38, No. 12, 2004, pp. 1430–1439. Translated from Fizika i Tekhnika Poluprovodnikov, Vol. 38, No. 12, 2004, pp. 1477–1486.

PHYSICS OF SEMICONDUCTOR DEVICES

Ultralow Internal Optical Loss in Separate-Confinement Quantum-Well Laser Heterostructures

S. O. Slipchenko, D. A. Vinokurov, N. A. Pikhtin^, Z. N. Sokolova, A. L. Stankevich, I. S. Tarasov, and Zh. I. Alferov

Ioffe Physicotechnical Institute, Russian Academy of Sciences, St. Petersburg, 194021 Russia

^e-mail: nike@hpld.ioffe.rssi.ru

Submitted May 12, 2004; accepted for publication May 17, 2004

Abstract—Internal optical loss in separate-confinement laser heterostructures with an ultrawide (>1 μm) waveguide has been studied theoretically and experimentally. It is found that an asymmetric position of the active region in an ultrawide waveguide reduces the optical confinement factor for higher-order modes and raises the threshold electron density for these modes by 10–20%. It is shown that broadening the waveguide to above 1 μm results in a reduction of the internal optical loss only in asymmetric separate-confinement laser heterostructures. The calculated internal optical loss reaches ~0.2 cm^{-1} (for $\lambda \approx 1.08$ μm) in an asymmetric waveguide 4 μm thick. The minimum internal optical loss has a fundamental limitation, which is determined by the loss from scattering on free carriers at the transparency carrier density in the active region. An internal optical loss of 0.34 cm^{-1} was attained in asymmetric separate-confinement laser heterostructures with an ultrawide (1.7 μm) waveguide, produced by MOCVD. Lasing in the fundamental transverse mode has been obtained owing to the significant difference in the threshold densities for the fundamental mode and higher-order modes. The record-breaking CW output optical power of 16 W and wallplug efficiency of 72% is obtained in 100-μm aperture lasers with a Fabry–Perot cavity length of ~3 mm on the basis of the heterostructures produced. © *2004 MAIK "Nauka/Interperiodica".*

1. INTRODUCTION

This paper continues a series of publications on studies aimed at developing and producing high-power semiconductor lasers [1–9]. Success in attaining record high power of optical emission is related to the optimization of the parameters of laser heterostructures, such as the threshold current density, threshold gain, differential quantum efficiency, internal optical loss, serial resistance, and temperature stability [1–10]. It was established that the principal factor that defines the power of optical emission of a semiconductor laser is the reduction of internal optical loss, and this can be attained by increasing the thickness of the waveguide layer. A detailed study and determination of parameters of a symmetric laser heterostructure characterized by low internal optical loss were reported in our previous publication [9]. A natural limitation on the thickness of a symmetric waveguide is imposed by the threshold conditions for higher-order waveguide modes [11]. The generation of higher-order modes deteriorates the far-field pattern in the plane normal to the *p–n* junction. At the same time, several attempts have been made to maintain lasing in only one fundamental transverse mode in lasers with a waveguide as thick as several micrometers [12–17]. The best results, where the angle of divergence of emission was reduced to 10°, were obtained using the effect of mode leakage from the waveguide of the laser heterostructure [16, 17]. However, this approach, like other cases we are aware of, resulted in an increase in internal loss and a reduction in the optical power [12–17].

In [8] we demonstrated the first successful application of an ultrawide asymmetric waveguide, with the goal of simultaneously reducing both the internal optical loss and emission divergence in the plane normal to the *p–n* junction. The enlargement of the waveguide thickness to 4 μm allowed us to reduce the internal optical loss to 0.7 cm^{-1} and the emission divergence to 16°–18° without significant loss of the maximum emission power, which was 8.6 W [8].

In this paper, we present theoretical and experimental studies of internal optical loss in separate-confinement quantum-well (SC QW) laser heterostructures with an asymmetric position of the active region in an ultrawide waveguide. The influence of the asymmetric position of the active region in an ultrawide waveguide on the suppression of higher-order modes is discussed. Semiconductor lasers based on optimized MOCVD-grown heterostructures have been fabricated, and their properties are studied. Record-breaking values of internal optical loss of 0.34 cm^{-1}, output optical power of 16 W, and a wallplug efficiency of 72% are obtained.

2. EXPERIMENTAL LASER STRUCTURES

All the theoretical and experimental studies were performed for SC QW laser heterostructures with a symmetric or asymmetric position of the active region

in the waveguide. Experimental laser heterostructures based on InGaAs/GaAs/AlGaAs solid solutions were grown by MOCVD in an Emcore GS-3100 setup. Depending on the material of the emitter layers, two series of structures were considered; their band structure is shown Fig. 1. Structures of series 1 consisted of two wide-gap emitters $Al_xGa_{1-x}As$ with $x = 0.6$, a GaAs waveguide layer, and an InGaAs QW 90 Å thick. In structures of series 2, another composition of solid solution, $Al_{0.3}Ga_{0.7}As$, was used in the emitters.

The two series differed only in the difference of the refractive indices between the emitter and waveguide layers (the waveguide efficiency). Multimode lasers with 100-μm-wide contacts and an emission wavelength of ~1μm were fabricated from the laser heterostructures.

3. MAIN DEFINITIONS

Optical loss in a laser heterostructure is constituted by the loss related to the emergence of emission from the cavity, α_{ext}, and the loss related to the processes within the laser heterostructure, α_{int}. The internal optical loss is related mainly to the scattering of photons on free carriers and layer inhomogeneities, α_S. The general relation for the internal loss by optical scattering, α_{int}, in a laser heterostructure has the form

$$\alpha_{int} = \sum \Gamma_{jm}\alpha_j + \alpha_S, \quad (1)$$

where Γ_{jm} is the optical confinement factor for mode m in the layer j; α_j, the loss related to scattering of light on free carriers in the jth layer; and α_S, loss related to inhomogeneities. The modern technology of laser heterostructures allows the production of homogeneous epitaxial layers, so that α_S becomes negligible. We therefore assume below that the internal optical loss is defined only by photon scattering on free carriers. In this study, we analyze separate-confinement double QW laser heterostructures of classical design (Fig. 1). In this case, the relation for internal optical loss (1) takes the form

$$\alpha_{int} = \alpha_{QW} + \alpha_{CL} + \alpha_W, \quad (2)$$

where α_{QW}, α_{CL}, and α_W are the internal optical loss in the active region, emitters, and the waveguide, respectively.

As shown in our earlier study [9], the major portion of loss in lasers with wide a waveguide (up to 1 μm) is related to the absorption in the active region and in the emitter layers. To reduce the internal optical loss, two approaches are possible. The first way is to enhance the change in the refractive index across the interface between the emitter and the waveguide. The second way is to enlarge the thickness of the waveguide layer [9]. In the first case, the possibilities are limited by the semiconductor materials currently available; in the second, by the condition that higher-order modes appear.

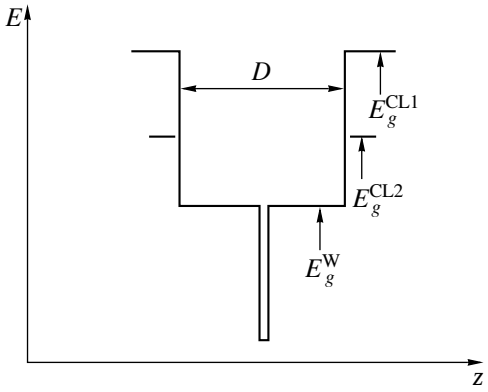

Fig. 1. Upper edge of the band gap in separate-confinement laser heterostructures with the waveguide layer width D and band gap E_g^W. Band gaps: E_g^{CL1}, for the emitter in series 1 structures; E_g^{CL2}, for the emitter in series 2 structures.

4. SELECTION OF HIGHER-ORDER MODES IN MULTIMODE ULTRAWIDE WAVEGUIDES

The fulfillment of threshold conditions for higher-order modes along with the principal mode is an inevitable consequence of enlarging the waveguide thickness in a double laser heterostructure [18]. To select the higher-order modes, three methods are known. The first is to enhance the absorption loss for higher-order modes in heavily doped emitter layers [11]. In the second method, the higher-order modes are selected by using the specific configuration that provides the leakage of these modes from the main waveguide [16]. In the third method, the higher-order modes are selected using the difference in the losses related to the emergence of emission from the cavity through the face of the mirror with an antireflection coating. This is performed by making the angle between the planes of the cavity mirror and the waveguide other than normal [19]. In this case, the output loss for higher-order modes in the plane normal to the p–n junction is higher than the loss for the fundamental mode. The methods listed above are related to the increase in total optical loss in the laser, which is not consistent with the concept we are developing of high-power semiconductor lasers.

The lasing threshold condition can be presented in the form

$$\Gamma_{QW}g(n_{QW}, p_{QW}) = \alpha_{int} + \alpha_{ext}, \quad (3)$$

where $g(n_{QW}, p_{QW})$ is the material gain in the active medium; n_{QW} and p_{QW}, the threshold densities of electrons and holes in the active region; and Γ_{QW}, the optical confinement factor of the active region. Note that, in the heterostructures under study, the threshold densities of electrons and holes do not coincide; this is related to

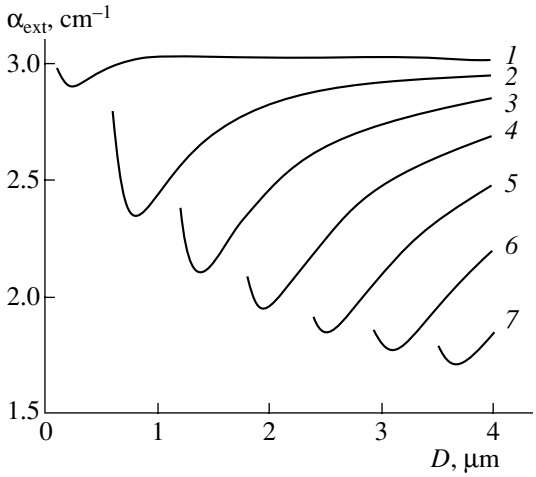

Fig. 2. External optical loss α_{ext} vs. the waveguide thickness D for laser diodes with cavity length L = 4 mm, fabricated from series 2 heterostructures with $Al_{0.3}Ga_{0.7}As$ emitters. Mode numbers: (*1*) zeroth, (*2*) 1st, (*3*) 2nd, (*4*) 3rd, (*5*) 4th, (*6*) 5th, and (*7*) 6th.

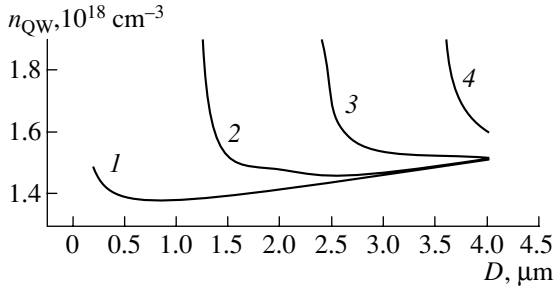

Fig. 3. Threshold electron density n_{QW} vs. the waveguide thickness D for symmetric laser heterostructures of series 2 with $Al_{0.3}Ga_{0.7}As$ emitters, with cavity length L = 4 mm. Mode numbers: (*1*) zeroth, (*2*) 2nd, (*3*) 4th, and (*4*) 6th.

electron emission from the QW in the active region, which is not deep enough [1, 9].

As follows from the lasing threshold condition (3), the fulfillment of the threshold conditions can be controlled by varying the threshold carrier density, the optical confinement factor for the corresponding mode, or the balance in total optical loss between the fundamental mode and higher-order modes. The expression for $g(n_{QW}, p_{QW})$, which relates the material gain in the active region with the free carrier density in the QW, was obtained experimentally in [20]; using this relation and Eq. (3), we can represent the threshold densities of electrons and holes as

$$n_{QW} = n_0 \exp\left\{\frac{2[\alpha_{int}(n_{QW}) + \alpha_{ext}]}{\Gamma_{QW} g_0}\right\}, \quad (4)$$

$$p_{QW} = p_0 \exp\left\{\frac{2[\alpha_{int}(p_{QW}) + \alpha_{ext}]}{\Gamma_{QW} g_0}\right\}, \quad (5)$$

where n_0 and p_0 are the transparency densities for electrons and holes, and g_0 is the gain. The coefficients n_0, p_0, and g_0 were determined experimentally. They characterize the properties of the active region and do not depend on the specific design of a laser heterostructure [20].

The calculation of threshold densities (4), (5) for the fundamental mode and higher-order modes as functions of the waveguide thickness includes the calculation of external optical loss, in which it is necessary to take into consideration that the reflectivities for different modes are different and depend on the thickness of the waveguide [19]. The reflectivity in a dielectric waveguide has been studied in detail by several authors [19, 21–25]. In our calculations, we used the simplest model based on the calculation of the average reflectivity in a dielectric waveguide. The average reflectivity was obtained as a sum of reflectivities in different layers of a heterostructure, taken in proportion to their volumes. Figure 2 shows dependences of external optical loss for different modes as functions of the thickness of the laser waveguide. The calculated results agree well with the data from [19, 21–25].

The calculated dependences of the external optical loss on the waveguide thickness and the relations (3)–(5) were used for the analysis of the dependence of the threshold carrier density in the active region on the waveguide thickness for the fundamental and higher-order modes. In this procedure, the internal optical loss $\alpha_{int}(n_{QW})$ for the fundamental and higher-order modes were calculated using the method derived in our earlier study [9]. A detailed discussion and calculation of the internal optical loss for higher-order modes in separate layers of laser heterostructures is presented below. In our calculation of internal optical loss and threshold densities, we chose the length of 4 mm for the Fabry–Perot cavity in the laser diode. For this cavity length, the saturation of gain in its dependence on the density $g(n_{QW}, p_{QW})$ is negligible [20].

Figure 3 shows the data calculated for a symmetric laser heterostructure of series 2 with a waveguide of lower efficiency (with the emitters made of $Al_{0.3}Ga_{0.7}As$ solid solution). The balance between the threshold densities for fundamental and higher-order modes depends on several parameters. Specifically, it depends on the waveguide efficiency Δn and the emission wavelength λ, which define the reflectivity and its dependence on the waveguide thickness and on the length of the Fabry–Perot cavity L, which, in turn, defines the ratio between the external and internal optical loss. In our case, for thick waveguide layers and long (L > 4 mm) Fabry–Perot cavities, the difference between the threshold density for the fundamental mode and that for higher-order modes did not exceed 1.8–6.4%. Such a small difference between the threshold densities for the fundamental and higher-order modes leads to simultaneous fulfillment of the threshold conditions for all modes in a laser diode. We believe that this fact can be attributed

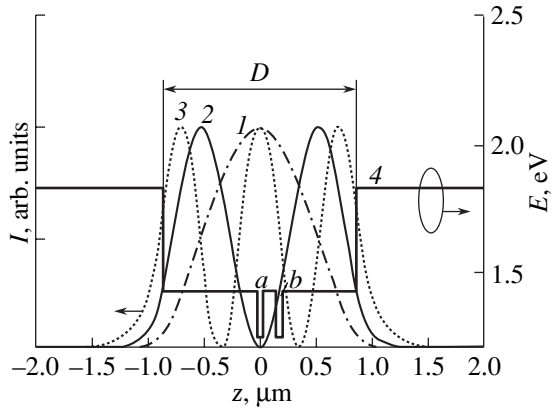

Fig. 4. Distribution of the intensity of the electromagnetic field in a laser heterostructure of series 2 with $Al_{0.3}Ga_{0.7}As$ emitters, with waveguide thickness $D = 1.7$ μm. Mode numbers: (*1*) zeroth, (*2*) 1st, and (*3*) 2nd. (*4*) Energy diagram of the upper edge of the band gap in (*a*) symmetric and (*b*) asymmetric laser heterostructure of series 2.

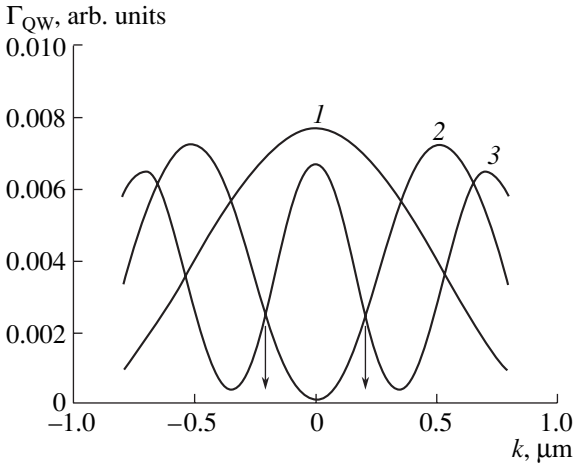

Fig. 5. Optical confinement factor of the active region, Γ_{QW}, as a function of the position of the active region in the waveguide, *k*. Mode numbers: (*1*) zeroth, (*2*) 1st, and (*3*) 2nd. The calculations were performed for a laser heterostructure of series 2, with $Al_{0.3}Ga_{0.7}As$ emitters and waveguide thickness $D = 1.7$ μm. Arrows indicate the positions of the active region with $\Gamma_{QW\_0}/\Gamma_{QW\_N} = \max$, where *N* is the mode number.

to fluctuations of carrier density within a QW and to a certain increase in the threshold density above the lasing threshold.

As stated earlier, several transverse modes exist in symmetric ultrawide waveguides. For example, we will now consider a heterostructure of series 2 ($Al_{0.3}Ga_{0.7}As$ emitters) with a waveguide thickness of 1.7 μm. In this case, the wave equation has three solutions, with the corresponding three stable configurations of the field (Fig. 4). In this laser heterostructure, the difference between the optical confinement factors of the active region (Γ_{QW_N}, where *N* is the mode number) for the

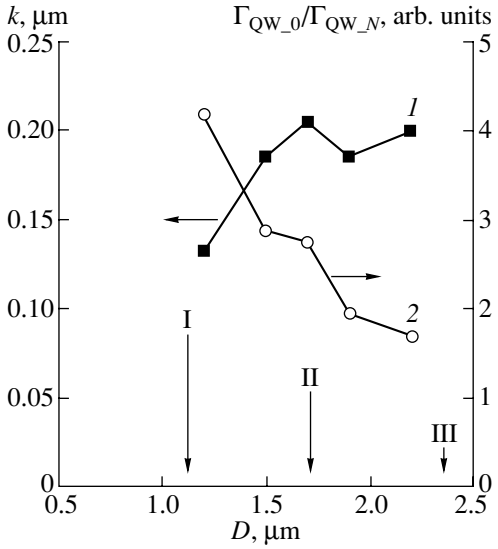

Fig. 6. Dependences on the waveguide thickness *D* for laser heterostructures of series 2 with $Al_{0.3}Ga_{0.7}As$ emitters: (*1*) optimal shift of the active region relative to the waveguide center, *k*; (*2*) the ratio $\Gamma_{QW\_0}/\Gamma_{QW\_N}$. Arrows indicate the thickness corresponding to the onset of the first, second, and third modes.

fundamental and higher-order modes is small. At the same time, the optical confinement factors of the active region are different for different modes, depending on the position of the active region within the waveguide (Fig. 5). At some specific positions of the active region within the waveguide, the optical confinement factor for the fundamental mode is higher than for higher-order modes (Fig. 5). If the ratio Γ_{QW_0} provides a sufficient difference between the threshold densities for the fundamental and higher-order modes, the threshold conditions for mode *N* will not be fulfilled. Our calculations allowed us to determine the manner in which the waveguide layer thickness affects the optimal position of the active region. The shift of the active region in respect to the waveguide center, which corresponds to the optimal position, steadily increases as the waveguide thickness increases (Fig. 6). However, when the waveguide thickness passes through the range in which a new higher-order mode arises, a sharp dip is observed in the dependence presented in Fig. 6. Figure 6 also shows the dependence $\Gamma_{QW\_0}/\Gamma_{QW\_N}$ for the optimal active region position as a function of the waveguide thickness. The increase in the waveguide thickness is followed by a decrease in selectivity. Especially sharp drops are observed when new higher-order modes appear.

In order to estimate the efficiency of selection of higher-order modes in asymmetric separate-confinement laser heterostructures, we have determined the threshold densities for all the modes existing in a multimode waveguide. The calculation was performed for symmetric and asymmetric structures with waveguide

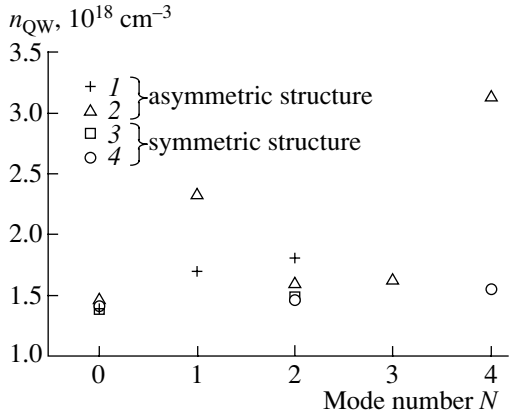

Fig. 7. Threshold electron density in the QW, n_{QW}, as a function of the mode number N for structures of series 2 with $Al_{0.3}Ga_{0.7}As$ emitters. The cavity length in laser diodes $L = 4$ mm. The waveguide thickness, D: (*1*, *3*) 1.7 μm and (*2*, *4*) 2.8 μm. The position of the active region: (*3*, *4*) in the center of the waveguide and (*1*, *2*) shifted to the optimal position.

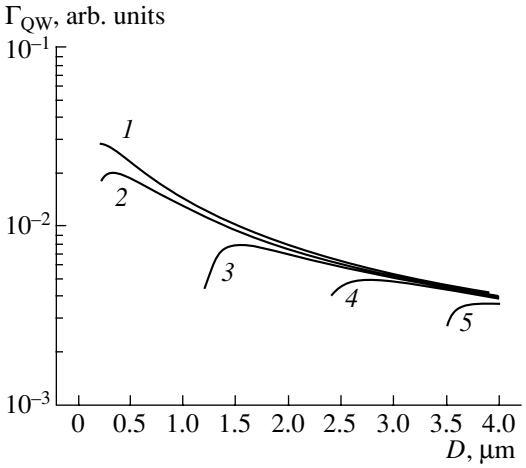

Fig. 8. Optical confinement factor of the active region, Γ_{QW}, as a function of the waveguide thickness D. (*1*) Zeroth mode in symmetric structures of series 1, with $Al_{0.6}Ga_{0.4}As$ emitters. For symmetric structures of series 2, with $Al_{0.3}Ga_{0.7}As$ emitters, mode numbers: (*2*) zeroth, (*3*) 2nd, (*4*) 4th, and (*5*) 6th.

thicknesses of 1.7 and 2.8 μm (Fig. 7). It was assumed that the active region is shifted into one of its optimal positions (Figs. 5, 6). In an asymmetric structure, the threshold density for a higher-order mode exceeds the threshold density for the fundamental mode ($N = 0$) at worst by 19.4 and 8.5% for laser heterostructures with a waveguide thickness of 1.7 and 2.8 μm, respectively (Fig. 7). According to the experimental data, this excess is sufficient for the selection of higher-order modes, the confirmation of which will be presented below. At the same time, in a symmetric structure the difference in the threshold densities for the fundamental and higher-order modes does not exceed 5% (Fig. 7).

5. INTERNAL OPTICAL LOSS BY SCATTERING IN THE ACTIVE REGION

The internal optical loss by scattering in the active region is usually presented in the form [18]

$$\alpha_{QW} = \Gamma_{QW}(\sigma_n n_{QW} + \sigma_p p_{QW}). \quad (6)$$

For a given material of the active region, with the cross sections σ_p and σ_n for hole and electron scattering, respectively, the magnitude of α_{QW} depends on the optical confinement factor of the active region, Γ_{QW}, and on the free carrier densities, n_{QW} and p_{QW}. To reduce α_{QW}, it is necessary that Γ_{QW}, n_{QW}, and p_{QW} have the lowest possible values.

Now we discuss the influence of the parameters of a laser heterostructure on the magnitudes of these variables. Figure 8 shows Γ_{QW} in symmetric structures as a function of the waveguide thickness D for fundamental modes in structures with emitters made of $Al_{0.6}Ga_{0.4}As$ and $Al_{0.3}Ga_{0.7}As$ solid solutions (curves *1* and *2*, respectively). The corresponding energy diagrams are shown in Fig. 1. The difference between the values of Γ_{QW} is observed only in the vicinity of their peaks. As the waveguide thickness increases, Γ_{QW} for fundamental modes in both structures becomes virtually equal. Thus, the increase in the waveguide efficiency does not lead to a significant increase in Γ_{QW} for structures with ultrawide waveguide layers.

Figure 8 also shows the optical confinement factor of the active region for higher-order modes in symmetric structures with $Al_{0.3}Ga_{0.7}As$ emitters (curves *3*–*5*). The values of Γ_{QW_N} for even higher-order modes virtually coincide with Γ_{QW_0} for the fundamental mode. Therefore, the principal contribution to the balance of gain between the fundamental mode and even higher-order modes is made by the internal optical loss in emitter layers and external loss at the exit.

The increase in the waveguide thickness results in the reduction of the optical confinement factor for the fundamental mode, as well as for higher-order modes (Fig. 8). However, the optical confinement factor and the free carrier density in a QW are related by the lasing threshold condition (3). This implies that, in a semiconductor laser with fixed internal and external optical loss, simultaneous reduction of the free carrier density and the optical confinement factor in the active region is impossible. However, in [20] we presented an experimental dependence of the material gain $g(n_{QW}, p_{QW})$ for the QW used as an active region in this study and a logarithmic approximation to this dependence. At a high density of free carriers, the material gain demonstrates a specific range of saturation. Therefore, the main specific feature of dependences (4) and (5) is that when the inequality

$$\Gamma_{QW} g_0 \geqslant \alpha_{int} + \alpha_{ext} \quad (7)$$

is fulfilled, the variation of Γ_{QW} has little or no effect on the free carrier density in the active region. To maintain

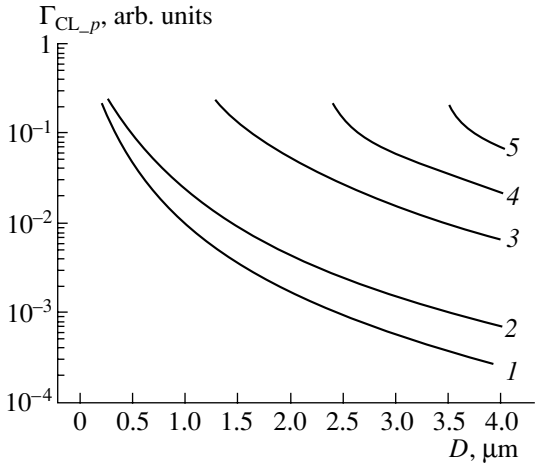

Fig. 9. The optical confinement factor of the *p*-type emitter, Γ_{CL_p}, as function of the waveguide thickness *D*. (*1*) Zeroth mode in structures of series 1, with $Al_{0.6}Ga_{0.4}As$ emitters. Mode numbers for structures of series 2, with $Al_{0.3}Ga_{0.7}As$ emitters: (*2*) zeroth, (*3*) 2nd, (*4*) 4th, and (*5*) 6th.

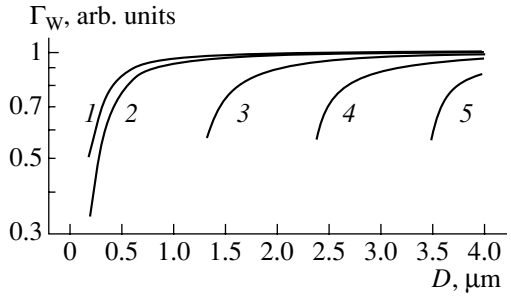

Fig. 10. Optical confinement factor of the waveguide, Γ_W, as a function of the waveguide thickness *D*. (*1*) Zeroth mode in structures of series 1, with $Al_{0.6}Ga_{0.4}As$ emitters. Mode numbers for structures of series 2, with $Al_{0.3}Ga_{0.7}As$ emitters: (*2*) zeroth, (*3*) 2nd, (*4*) 4th, and (*5*) 6th.

the validity of (3), it is clear that the reduction of Γ_{QW} must be compensated for by a high material gain *g*. The increase in the material gain for the given composition of the active region can be reached only by increasing the free carrier density. However, due to the superlinearity of dependence $g(n_{QW}, p_{QW})$, the initial increase in densities n_{QW} and p_{QW} is insignificant. In other words, when the inequality (7) is valid, the increase in the waveguide thickness, which reduces Γ_{QW}, makes it possible to reduce α_{QW}. Therefore, the widening of the waveguide is the most effective way to reduce the internal optical loss by scattering on free carriers in the active region.

6. INTERNAL OPTICAL LOSS BY SCATTERING IN THE WAVEGUIDE AND EMITTERS

The total optical loss by scattering in the emitters (CL) can be presented in the form

$$\alpha_{CL} = \Gamma_{CL\_n}\sigma_n n_{CL\_n} + \Gamma_{CL\_p}\sigma_p p_{CL\_p}, \quad (8)$$

where σ_n and σ_p are the cross sections of scattering for electrons and holes; Γ_{CL_n} and Γ_{CL_p}, the optical confinement factors of *n*- and *p*-type emitters; and n_{CL_n} and p_{CL_p}, carrier densities in *n*- and *p*-type emitters.

Figure 9 shows the calculated optical confinement factors of the *p*-type emitter, Γ_{CL_p}, for different modes at different waveguide thicknesses *D* for the structures under study (see Fig. 1). In contrast to the active region, in emitter layers the difference between the optical confinement factors for the fundamental mode and higher-order modes is significant; this factor must be taken into account in the discussion of the gain balance and threshold densities for different modes in an ultrawide waveguide.

The waveguide efficiency has a strong effect on Γ_{CL_p}; namely, the difference between the values of Γ_{CL_p} for structures with different waveguide efficiency increases when the waveguide layer thickness *D* increases (Fig. 9, curves *1* and *2*). With similar conditions of doping, the loss in emitters, α_{CL}, will be higher in structures with a lower change in the refractive index across the interface between the waveguide and emitter. Despite this factor, the widening of the waveguide allows the reduction of Γ_{CL_p} to a fraction of one percent in both types of structures (Fig. 9), when the depth of penetration of the field of a mode into emitters is reduced to fractions of a micrometer. In contrast to the active region, the free carrier density in emitters is determined by the technology of the laser heterostructure growth, so the density can be varied over a wide range. Therefore, the optimization of the density profile of carries in emitter layers can be an effective method for the reduction of α_{CL}. Thus, the use of ultrawide waveguides and optimized profiles of emitter doping makes it possible to minimize the α_{CL} contribution to the total optical loss, regardless of the waveguide efficiency.

The internal optical loss in the waveguide layers is calculated as

$$\alpha_W = \Gamma_W(\sigma_n n_W + \sigma_p p_W), \quad (9)$$

where Γ_W and n_W, p_W are, respectively, the confinement factor and the electron and hole densities in the waveguide. Figure 10 shows the calculated optical confinement factor of the waveguide, Γ_W, for different modes as functions of the waveguide thickness *D* for the structures under study (Fig. 1). For both types of laser heterostructures with an ultrawide (over 1 μm) waveguide, Γ_W is virtually independent of the waveguide thickness and efficiency, except in the ranges where new modes appear (Fig. 10). Therefore, the only way to reduce α_W is to reduce the concentration of uncontrolled impurities in the waveguide layers.

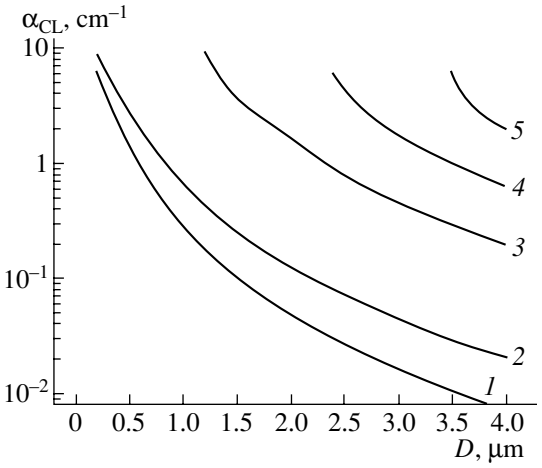

Fig. 11. Internal optical loss in two emitter layers, α_{CL}, as a function of the waveguide thickness, *D*. (*1*) Zeroth mode in symmetric structures of series 1, with $Al_{0.6}Ga_{0.4}As$ emitters. Mode numbers for symmetric structures of series 2, with $Al_{0.3}Ga_{0.7}As$ emitters: (*2*) zeroth, (*3*) 2nd, (*4*) 4th, and (*5*) 6th.

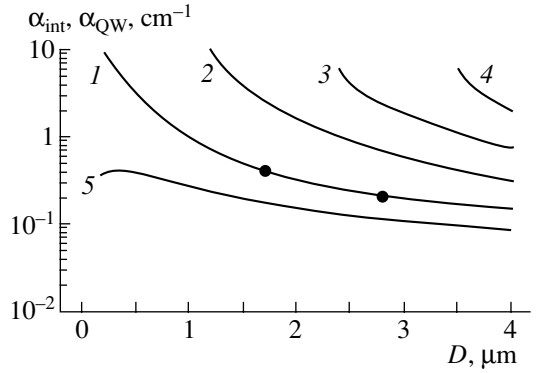

Fig. 12. Total optical loss α_{int} as a function of the waveguide thickness *D* for symmetric laser heterostructures of series 2, with $Al_{0.3}Ga_{0.7}As$ emitters. Mode numbers: (*1*) zeroth, (*2*) 2nd, (*3*) 4th, and (*4*) 6th. (*5*) Internal optical loss in the active region, α_{QW}, for the zeroth mode in the same structure. Points are the total optical loss α_{int} for the zeroth mode in heterostructures with an asymmetric position of the active region.

7. CALCULATION OF TOTAL INTERNAL OPTICAL LOSS

In the previous sections, we analyzed the dependences of the main components of internal optical loss on the parameters of a separate-confinement laser heterostructure. Below, we are going to perform a quantitative analysis of total optical loss α_{int} for two series of symmetric and asymmetric laser heterostructures. To calculate the internal optical loss, it is necessary to know the optical confinement factors for modes in each layer of the structure, the absorption cross sections for electrons and holes, and the free carrier densities. The calculated dependences of the optical confinement factors for both series of structures were already shown in Figs. 8–10. In the calculations, we used the following values of the scattering cross section for electrons and holes: $\sigma_n = 3 \times 10^{-18}$ cm^2 and $\sigma_p = 7 \times 10^{-18}$ cm^2 [26]. We also used the free carrier densities in the heterostructure layers, with the parameters preset by the technology. The electron and hole densities in *n*- and *p*-type emitters were $n = 10^{18}$ cm^{-3} and $p = 3.5 \times 10^{18}$ cm^{-3}. The waveguide layers were regarded as undoped, with a residual impurity concentration of 3×10^{15} cm^{-3}.

For both types of heterostructures, the internal optical loss in the waveguide layers was calculated from (9); the value obtained was about 0.03 cm^{-1}, with the wavelength thickness varying from 1 to 4 μm. In the calculation of the internal optical loss in two emitter layers in the structures under study, we used the relation (8). The obtained dependences are shown in Fig. 11.

The internal optical loss in the active region, α_{QW}, was calculated using the relation (6). The density of free carriers in the active region was determined from (4), (5). Since the threshold density is determined not only by the internal loss but also by the loss related to the emergence of emission from the cavity [see (3)], a constant cavity length of $L = 4$ mm was assumed. Figure 3 shows the threshold density of electrons in the active region for a symmetric structure (Fig. 1) as a function of the waveguide thickness. In the calculation of the threshold density of free carriers in the active region, the electron emission from the QW was taken into account using the technique proposed in [27]. Therefore, in the calculation of α_{QW}, the density of electrons localized in the Coulomb QW was taken into account. Based on these calculations, we obtained α_{QW} as functions of the waveguide thickness in symmetric laser heterostructures (Fig. 12, curve *5*). Figure 12 also shows the dependences of total internal loss in a symmetric separate-confinement structure on the waveguide thickness. Points indicate the total internal optical loss for the fundamental mode in asymmetric structures with waveguide thicknesses of 1.7 and 2.8 μm. For these thicknesses, the total internal optical loss in an asymmetric structure virtually coincides with the loss for the fundamental mode in a symmetric structure. At a waveguide thickness over 1 μm, the principal contribution to the total loss is made by the internal loss in the active region, α_{QW}, because the loss is small in the emitters and negligible in the waveguide. In fact, α_{QW} defines the internal optical loss α_{int} in laser heterostructures with an ultrawide waveguide. When the waveguide thickness exceeds 3 μm, increasing it further does not change Γ_{QW} (Fig. 8). The lower limit of the threshold carrier density in a QW is determined by the transparency densities for electrons and holes, n_0 and p_0, which are defined by the properties of the material of the active region. The difference between the threshold density and the transparency density depends on the total optical loss, as well as on the behavior of

$g(n_{QW}, p_{QW})$. The values of n_0 and p_0 for the QW used in the active region in this study were experimentally determined in [20]. The greatest fraction of the threshold density in the dependences we obtained (Fig. 3) is the transparency density. Therefore, the calculated minimum internal optical loss is, in fact, the lower fundamental limit for laser heterostructures with an active region consisting of InGaAs QWs with an emission wavelength of about 1 μm.

8. CHOICE OF PARAMETERS FOR THE OPTIMAL HETEROSTRUCTURE AND EXPERIMENTAL LASERS WITH A WIDE STRIPE CONTACT

Separate-confinement laser heterostructures with the design devised in the process of modeling were grown by MOCVD. As shown above, the shift of the active region in respect to the center of the waveguide opens the way for an efficient suppression of lasing at higher-order modes. However, the suppression efficiency decreases as the waveguide thickness increases. Therefore, we chose an asymmetric laser structure with a 1.7-μm-thick waveguide as the basic structure. The experimental heterostructure consisted of the following epitaxial layers: heavily doped n-$Al_{0.3}Ga_{0.7}As$ (n = 10^{18} cm^{-3}) and p-$Al_{0.3}Ga_{0.7}As$ (p = 3.5×10^{18} cm^{-3}) emitters (Si and Mg were used as donor and acceptor impurities, respectively), and a nominally undoped GaAs waveguide. The active region was a single strained InGaAs QW 90 Å thick. The composition of the solid solution of the QW corresponded to a electroluminescence wavelength of 1.05 μm.

Standard postgrowth treatment [28, 29] was used for the fabrication of mesa-stripe lasers with a stripe width of 100 μm and different lengths of the Fabry–Perot cavity, L = 1.5–4 mm.

Light–current characteristics in the CW mode were measured for all the fabricated devices, at a heat sink temperature of 20°C. Based on the data obtained, the dependence of the inverse external differential quantum efficiency on the cavity length was plotted (Fig. 13). The linear approximation to the dependence obtained allowed us to determine the internal quantum yield of the stimulated emission and the internal optical loss, which were η_i = 99% and α_i = 0.34 cm^{-1}, respectively. The ultralow internal optical loss achieved in this heterostructure design opens the way for the fabrication of laser diodes with ultralong cavities, without a noticeable decrease in the external differential quantum efficiency. The enlargement of the cavity length makes it possible to use higher driving currents and, respectively, to significantly increase the emission power, while retaining the high efficiency of the electric-to-optical energy conversion.

Figure 14 shows the typical dependence of the emission power and wallplug efficiency on the driving current

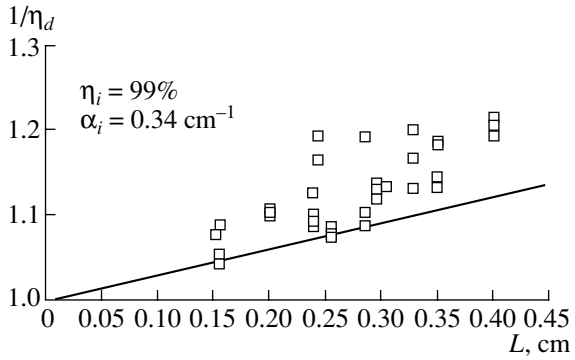

Fig. 13. Inverse external differential quantum efficiency $1/\eta_d$ as a function of the cavity length L in an asymmetric laser heterostructure with waveguide thickness D = 1.7 μm and $Al_{0.3}Ga_{0.7}As$ emitters. Solid line: approximation to the experimental data.

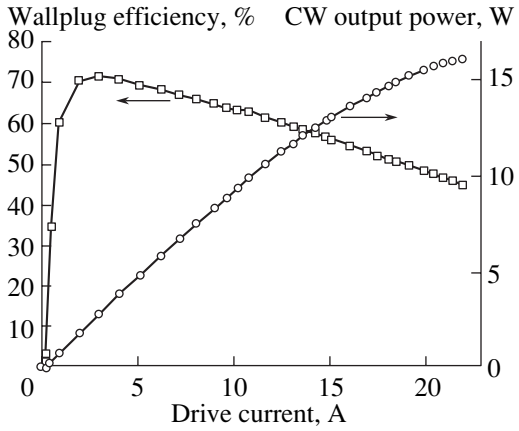

Fig. 14. Light–current characteristic and wallplug efficiency as functions of the driving current for a laser diode with cavity length L = 3040 μm, the stripe width 100 μm, and with high-reflection (95%) and antireflection (5%) coatings on the cavity faces. CW mode, temperature 20°C.

for a laser diode with the cavity length L = 3040 μm and antireflection and high-reflection insulator coatings deposited on the cavity faces, with power reflection coefficients of 5 and 95%. The output CW power was 16 W and the wallplug efficiency reached 72% at a stable heat sink temperature of 20°C. This value of the CW power is the highest obtained for semiconductor lasers [30].

Figure 15 shows typical far-field emission patterns in the plane normal to the p–n junction for different values of the driving current in laser diodes. It can be seen that the value of $\Theta_\perp$ and the shape of the line remain virtually unchanged when the driving current increases. Such a stable behavior of the far-field emission pattern indicates that the emission of the laser diode in the plane normal to the p–n junction is single-mode.

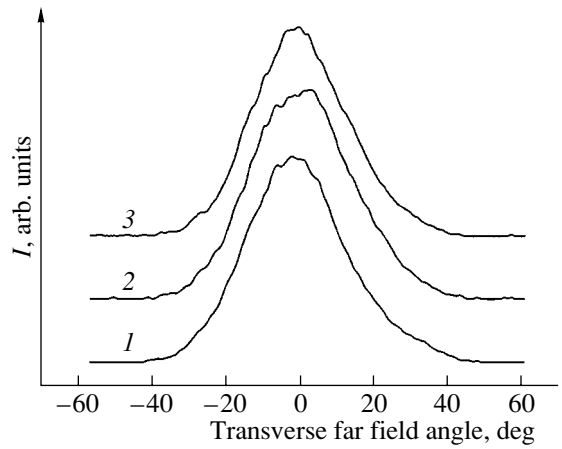

Fig. 15. Far-field emission pattern in the plane normal to the *p–n* junction, as a function of the angle Θ, for driving current (*1*) 0.4, (*2*) 5, and (*3*) 10 A. FWHM of the pattern, $\Theta_\perp$: (*1*) 30, (*2*) 33, and (*3*) 31 deg.

9. CONCLUSION

We conclude that progress in the design of high-power semiconductor lasers is possible with the use of asymmetric SC QW heterostructures. In symmetric separate-confinement heterostructures, the enlargement of the waveguide width above 1 μm gives rise to higher-order modes. This is related to the fact that, in multimode lasing, the difference between the threshold densities for the fundamental mode and higher-order modes does not exceed 5%. When higher-order modes arise, the internal optical loss strongly increases due to the strong penetration of these modes into the doped emitters. In asymmetric SC QW heterostructures with a waveguide width above 1 μm, higher-order modes can be suppressed, because the difference between the threshold densities for these modes and the fundamental mode is sufficiently large. It is shown that a difference of ~20% in the threshold densities for the fundamental and higher-order modes is sufficient for the suppression of higher-order modes. The internal optical loss in an asymmetric waveguide is defined by the loss by scattering on free carriers only for the fundamental mode. The lower fundamental limit to the internal optical loss is the internal optical loss by scattering on free carriers at the transparency density. The calculated internal optical loss in an ultrawide asymmetric waveguide for real structures approaches the fundamental limit. In MOCVD-fabricated laser heterostructures with a 1.7-μm-wide asymmetric waveguide, an internal optical loss of 0.34 cm^{-1} was obtained, which coincides with the calculated value. The fundamental limit to the internal optical loss for a similar structure with $D > 4$ μm is 0.2 cm^{-1}. As the waveguide thickness increases, the internal optical loss tends to its fundamental limit.

In lasers with a 100-μm aperture and a length of the Fabry–Perot cavity of ~3 mm, we obtained a record high CW emission power of 16 W in the fundamental transverse mode and a wallplug efficiency of 72%.

ACKNOWLEDGMENTS

The authors are grateful to A.A. Marmalyuk, I.D. Zalevskiĭ, and V.P. Evtikhiev for valuable discussions; to D.N. Nikolaev, V.V. Shamakhov, A.V. Murashova, S.A. Zorina, A.Yu. Leshko, and V.V. Vasilieva for assistance in the fabrication of heterostructures; to M.A. Khomylev, V.V. Kapitonov, A.V. Lyutetskiĭ, and N.V. Fetisova for the optical studies of the samples; and to T.A. Nalet, T.N. Drokina, and N.A. Rudova for preparing the laser diodes.

This study was supported in part by the Russian scientific and technical program "Physics of Solid-State Nanostructures."

REFERENCES

1. A. Yu. Leshko, A. V. Lyutetskiĭ, N. A. Pikhtin, and G. V. Skrynnikov, Fiz. Tekh. Poluprovodn. (St. Petersburg) **34**, 1457 (2000) [Semiconductors **34**, 1397 (2000)].
2. D. A. Vinokurov, V. A. Kapitonov, D. N. Nikolaev, *et al.*, Fiz. Tekh. Poluprovodn. (St. Petersburg) **35**, 1380 (2001) [Semiconductors **35**, 1324 (2001)].
3. E. G. Golikova, V. A. Kureshov, A. Yu. Leshko, *et al.*, Fiz. Tekh. Poluprovodn. (St. Petersburg) **34**, 886 (2000) [Semiconductors **34**, 853 (2000)].
4. D. A. Livshits, A. Yu. Egorov, I. V. Kochnev, *et al.*, Fiz. Tekh. Poluprovodn. (St. Petersburg) **35**, 380 (2001) [Semiconductors **35**, 365 (2001)].
5. P. V. Bulaev, V. A. Kapitonov, A. V. Lyutetskiĭ, *et al.*, Fiz. Tekh. Poluprovodn. (St. Petersburg) **36**, 1144 (2002) [Semiconductors **36**, 1065 (2002)].
6. D. A. Livshits, I. V. Kochnev, V. M. Lantratov, *et al.*, Electron. Lett. **36**, 1848 (2000).
7. A. V. Lyutetskiĭ, N. A. Pikhtin, S. O. Slipchenko, *et al.*, Fiz. Tekh. Poluprovodn. (St. Petersburg) **37**, 1394 (2003) [Semiconductors **37**, 1356 (2003)].
8. S. O. Slipchenko, N. A. Pikhtin, N. V. Fetisova, *et al.*, Pis'ma Zh. Tekh. Fiz. **29** (23), 26 (2003) [Tech. Phys. Lett. **29**, 980 (2003)].
9. N. A. Pikhtin, S. O. Slipchenko, Z. N. Sokolova, and I. S. Tarasov, Fiz. Tekh. Poluprovodn. (St. Petersburg) **38**, 374 (2004) [Semiconductors **38**, 360 (2004)].
10. B. Ryvkin, E. Avrutin, and M. Pessa, Electron. Lett. **38**, 991 (2002).
11. A. Al-Muhanna, L. J. Mawst, D. Botez, *et al.*, Appl. Phys. Lett. **73**, 1182 (1998).
12. J. Temmyo and M. Sugo, Electron. Lett. **31**, 642 (1995).
13. D. Vakhshoori, W. S. Hobson, H. Han, *et al.*, Electron. Lett. **32**, 1007 (1996).
14. J. M. Verdiell, M. Ziari, and D. F. Welch, Electron. Lett. **32**, 1817 (1996).
15. N. B. Zvonkov, S. A. Akhlestina, A. V. Ershov, *et al.*, Kvantovaya Élektron. (Moscow) **26**, 217 (1999) [Quantum Electron. **29**, 217 (1999)].

16. V. I. Shveĭkin and V. A. Gelovani, Kvantovaya Élektron. (Moscow) **32**, 683 (2002) [Quantum Electron. **32**, 683 (2002)].
17. J. P. Donnelly, R. K. Huang, J. N. Walpole, *et al.*, IEEE J. Quantum Electron. **39**, 289 (2003).
18. H. C. Casey, Jr. and M. B. Panish, *Heterostructure Lasers* (Academic, New York, 1978; Mir, Moscow, 1981).
19. I. A. Kostko, V. P. Evtikhiev, E. Yu. Kotel'nikov, and G. G. Zegrya, Fiz. Tekh. Poluprovodn. (St. Petersburg) **33**, 752 (1999) [Semiconductors **33**, 693 (1999)].
20. N. A. Pikhtin, S. O. Slipchenko, Z. N. Sokolova, and I. S. Tarasov, Fiz. Tekh. Poluprovodn. (St. Petersburg) **36**, 364 (2002) [Semiconductors **36**, 344 (2002)].
21. T. Ikegami, IEEE J. Quantum Electron. **8**, 470 (1972).
22. E. I. Gordon, IEEE J. Quantum Electron. **9**, 772 (1973).
23. D. C. Krupka, IEEE J. Quantum Electron. **11**, 390 (1975).
24. L. Levin, IEEE Trans. Microwave Theory Tech. **23**, 576 (1975).
25. C. M. Herzinger, C. C. Lu, T. A. DeTemple, and W. C. Chew, IEEE J. Quantum Electron. **29**, 2272 (1993).
26. E. Pinkas, B. I. Miller, I. Kayashi, and P. W. Foy, IEEE J. Quantum Electron. **9**, 281 (1973).
27. L. V. Asryan, N. A. Gunko, A. S. Polkovnikov, *et al.*, Semicond. Sci. Technol. **15**, 1131 (2000).
28. E. G. Golikova, V. A. Gorbylev, Yu. V. Il'in, *et al.*, Pis'ma Zh. Tekh. Fiz. **26** (7), 57 (2000) [Tech. Phys. Lett. **26**, 295 (2000)].
29. A. Yu. Leshko, A. V. Lyutetskiĭ, N. A. Pikhtin, *et al.*, Fiz. Tekh. Poluprovodn. (St. Petersburg) **36**, 1393 (2002) [Semiconductors **36**, 1308 (2002)].
30. F. Bugge, G. Erbert, J. Fricke, *et al.*, Appl. Phys. Lett. **79**, 1965 (2001).

Translated by D. Mashovets